ASSESSING GRAPEVINE CANOPY HEALTH IN THE TEXAS HILL COUNTRY WITH REMOTE SENSING AND GIS TECHNIQUES

by

Adam J. Mathews, B.S., M.A.

A dissertation submitted to the Graduate Council of
Texas State University in partial fulfillment
of the requirements for the degree of
Doctor of Philosophy
with a Major in Geography-GIScience
May 2014

Committee Members:

Jennifer L. R. Jensen, Chair

F. Benjamin Zhan

Richard W. Dixon

Andrew Hall

FAIR USE AND AUTHOR'S PERMISSION STATEMENT

Fair Use

Duplication Permission

DEDICATION

I dedicate this work to my Uncle Earnie who passed away a few months before the completion of this dissertation. I will never forget his love of my love of maps. It was always enjoyable to talk about GPS, GIS, and maps with him. I will also never forget the time spent with him on our family vacations. He always had a way of making everyone around him feel special and, of course, laugh. I will miss our time together with the family, GPS talks, and sharing links of the latest online maps. Rest in peace.

ACKNOWLEDGEMENTS

I would firstly like to thank and acknowledge the efforts of my advisor Jennifer Jensen. I am extremely grateful for the time and effort she put in to my work as a doctoral student. Jenn always had the time to discuss research methods, exchange teaching approaches, write letters of recommendation (and there were many!), and provide feedback on manuscripts. With Jenn's guidance, my writing improved tremendously during my time at Texas State. I really admire her high standard of research and work in general. Jenn sets the bar high and will accept nothing less. I have benefitted greatly from abiding by this credo. Thank you so much for everything!

Additionally, thanks are extended to my dissertation committee, Benjamin Zhan, Richard Dixon, and Andrew Hall, for support throughout my doctoral work that culminated in the production of this dissertation. Thank you all very much for your time, effort, advice, and continued encouragement. I would further like to thank Andrew Hall for serving as my supervisor while I spent time abroad. In regards to this dissertation and other research projects, Andrew kindly provided valuable advice throughout it all.

I am very grateful for access to the study vineyard that was granted by the property owners. I also greatly appreciate assistance provided by the vineyard manager, winemaker, and maintenance personnel throughout my study.

I thank the many people who helped collect the data used in this dissertation including John Klier (Chapters II and III) and Joel Scholz (Chapter IV) for piloting the UAV to collect aerial images. Thank you so much John! Jennifer Jensen helped collect

the LAI data used in Chapter IV. Kumudan Grubh, Matt Patton, and David Yelacic assisted in the capture of spectroradiometer measurements in San Marcos to calibrate the digital cameras in Chapter II. Ryan Schuermann helped collect the harvest data utilized in Chapter IV. Thank you all so much for your time.

I would like to thank the Graduate College at Texas State University for providing financial support (a doctoral research stipend award) for this dissertation. Additionally, I would like to thank the Department of Geography for supporting my efforts in my time at Texas State University. This includes help provided by faculty (Yongmei Lu, Sven Fuhrmann, and Nathan Currit), staff (Allison Glass-Smith, Pat Hell-Jones, and Angelika Wahl), and colleagues (Matt Patton, David Yelacic, Ryan Schuermann, David Parr, Elyse Zavar, and Nathaniel Dede-Bamfo). Thank you all for your friendship and support.

Lastly, I would like to acknowledge my immediate support network: my family. Most importantly, I thank my fiancé Carolyn for being by my side throughout the ups and downs of being a doctoral student. Your support has been vital to my success as a student and professional. I cannot wait until June 21st! I would also like to acknowledge my family members who have played a vital role in my development as a person as well as a student: Mom and Jeff, Dad and Amy, Brad and Kelly, Uncle Marty and Aunt Peggy, Ashley and Honorio, my grandparents, and the rest of my family.

TABLE OF CONTENTS

Page

ACKNOWLEDGEMENTS v

LIST OF TABLES x

LIST OF FIGURES xi

LIST OF ABBREVIATIONS xiii

ABSTRACT xiv

CHAPTER

I. INTRODUCTION 1

Background 1
Geography and Viticulture: Past and Present 1
Variability in the Vineyard 2
Current Research Areas 4
Land Use Delineation 4
Site Location and Suitability Modeling 5
Precision Viticulture 6
Remote Sensing of Vineyards 7
Research Objectives and Chapter Outline 8
Study Site 9

II. IMAGING SYSTEM SET-UP, CALIBRATION, AND APPLICATION IN THE VINEYARD 11

Introduction 11
Use of Compact Digital Cameras in Remote Sensing 11
Improving the Quality of Collected Images 13
Radiometric Corrections 14
Geometric Corrections 17
Objective 18
Materials and Methods 19
Digital Cameras 19
On-Ground Image Collection and Camera Calibration 20

Application of UAV-based Image System to the Study Vineyard and Generation of Analysis Ready Image Products 23
Study Site and Data Collection 23
Data Processing....27
Output Validation....30
Results....31
On-Ground Image Collection and Camera Calibration 31
Application of UAV-Based Image System to the Study Vineyard and Generation of Analysis-Ready Image Products 33
Orthophoto Generation and Per-Band Reflectance Conversion 33
Per-Band Validation....33
Discussion 34
Validation Results 34
Practicality of Provided Methodology and Future Work....36
Conclusion 38

III. AN ANALYSIS OF VINEYARD CANOPY HEALTH THROUGHOUT A GROWING SEASON....48

Introduction....48
Methods....53
Study Vineyard 53
Data Collection 54
UAV Image Collection 54
Other Field Measurements....56
Data Processing....59
Data Analysis 63
Results....65
Canopy Area 65
Canopy Density....67
Vine Performance Index and Management Zone Delineation....68
Discussion 69
Assessment of Methodology and Results 69
Future Work 71
Conclusion 72

IV. A NEW METHOD FOR VISUALIZING AND QUANTIFYING VINEYARD CANOPY DENSITY 78

Introduction....78
Materials and Methods....83
Study Site....83
Data Collection....83
Data Processing....87
Data Analysis....88
Results....90
SfM Results and Point Cloud Visualization....90
Relationship between SfM Output and LAI....93
Discussion....94
General Study Limitations....94
SfM as an Alternative Source of High-Density 3D Data....95
SfM LAI Estimates Compared to Lidar and Spectral-based Approaches....97
Potential of SfM as a Source of 3D Data for LAI Estimation....98
Conclusions....99

V. CONCLUSIONS....106

Chapter II Accomplishments....106
Chapter III Accomplishments....107
Chapter IV Accomplishments....108
Final Recommendations for Viticulturists....108

LITERATURE CITED....110

LIST OF TABLES

Table **Page**

2.1. Spectral calibration test results for UDC (visible bands).....39

2.2. Spectral calibration test results for ADC (NIR bands) 40

2.3. Derived reflectance conversion equations for each band 40

3.1. UAV-collected images, conversion results, and output orthophoto attributes 73

3.2. Canopy area correlations.....73

3.3. Canopy density correlations.....74

4.1. Inputs and outputs of PhotoScan and LP360 point cloud processing.....100

4.2. Results of stepwise multiple regression predicting LAI based on SfM derived metrics.....101

LIST OF FIGURES

Figure **Page**

2.1. Sample images of spectral targets captured with the UDC (a) and the ADC (b) with the regions of interest (ROIs) shown (a) in different colors 41

2.2. The study vineyard blocks with UAV flight path 41

2.3. The kitewing UAV (a) with mounted digital camera (b) and other hardware 42

2.4. Data workflow from UAV image capture to final orthophoto generation....42

2.5. Comparison of image mosaics (RGB: a, b; NIR: c, d) with (b, d) and without (a, c) image histogram equalization 43

2.6. High- vs. low-altitude aerial image capture of vineyard canopy 43

2.7. Relationships between spectroradiometer measured reflectance (Y-axis) and digital camera measured brightness (X-axis) of spectral targets within blue (a), green (b), red (c), and NIR (d) bands 44

2.8. Spectral signatures of selected targets from sample 1 with camera spectral ranges and optimal band wavelength intervals....45

2.9. Generated orthophoto bands of blue (a,e), green (b,f), red (c,g), and NIR (d,h) at the whole-vineyard (a-d) and partial-vineyard (e-h) scales 46

2.10. Validation results comparing measured (Y-axis) and estimated (X-axis) reflectance of vines and spectral targets within each band....47

3.1. The study vineyard in the Texas Hill Country AVA 74

3.2. Data workflow from collection through processing and final analysis 75

3.3. Image segmentation results and extraction zones for select vine canopies for the veraison RGB orthophoto 76

3.4. Observed canopy area (mean area of RGB and NIR segments) for the study vineyard at (a) post-flowering, (b) veraison, (c) harvest, as well as for (d) the entire growing season (season average)....76

3.5. Observed canopy density (NDVI-based) for the study vineyard at (a) post-flowering, (b) veraison, (c) harvest, as well as for (d) the entire growing season (season average) 77

3.6. Vine performance analyses including (a) the calculated vine performance index or VPI, (b) vine grouping results, and (c) proposed management zones numbered from 1 (high vigor) to 6 (low vigor) 77

4.1. Study area in the Texas Hill Country American Viticultural Area with winery locations 101

4.2. The study vineyard blocks 102

4.3. The filtered point cloud of ground (gray) and non-ground (orange) points 102

4.4. A comparison of an actual UAV captured image (a) and the filtered point cloud (b) for the same area 103

4.5. The density of points (local average number of points per square meter) for both the ground and non-ground point clouds 103

4.6. Three-dimensional visualization of the study vineyard (a, b, and c) including sample vines (red poles) with highlighted sample rows, non-ground point cloud (green spheres), projected trellis wiring (gray lines), and underlying DTM surface at (a) whole vineyard, (b) partial vineyard, and (c) per-vine scales. 104

4.7. Canopy density (measured LAI) across the study vineyard blocks 105

4.8. Scatterplot of LAI predicted with SfM height metrics (Y-axis) and field-measured LAI (X-axis) 105

LIST OF ABBREVIATIONS

Abbreviation **Description**

ADC – Altered Digital Camera

AVA – American Viticultural Area

CHDK – Canon Hackers Development Kit

DNs – Digital Numbers

DSM – Digital Surface Model

DTM – Digital Terrain Model

FOV – Field of View

GCP – Ground Control Point

GIS – Geographic Information System

GPS – Global Position System

LAI – Leaf Area Index

NDVI – Normalized Difference Vegetation Index

NIR – Near-infrared

RGB – Red, Green, and Blue

SfM – Structure from Motion

THCAVA – Texas Hill Country American Viticultural Area

UAV – Unmanned Aerial Vehicle

UAS – Unmanned Aerial System

UDC – Unaltered Digital Camera

ABSTRACT

Vineyards are typically managed uniformly over space, although known spatial variation exists in the performance of vines within and across vineyard blocks. Identifying spatial variability in crop performance at a large scale (one or a few vineyard blocks) is useful to vineyard managers wishing to address such variation by enacting separate management plans for differing areas of performance. Zonal management and the institution of precision viticultural practices (i.e. use of GIS and remote sensing techniques to study this spatial variation) has proven profitable for a number of reasons, namely zonal harvesting based on zone performance.

This dissertation implements cutting-edge, practical, and low-cost equipment and techniques, specifically an unmanned aerial vehicle (UAV), digital cameras, and Structure from Motion (SfM), to identify spatial variation in grapevine canopy vigor at a vineyard in the Texas Hill Country American Viticultural Area. Three research objectives were addressed in this dissertation including: (1) the setup and implementation of a practical imaging system and processing methodology (digital cameras and a UAV) to produce very high spatial resolution orthophotomosaics of vineyards with visible and near-infrared bands, (2) observation of spatial and temporal variation in grapevine canopy vigor that can aid in improving vineyard management practice, and (3) development of a three-dimensional method for visualizing and quantifying vineyard canopy density. Results concluded that the low-cost tools and techniques outlined in this study provided a practical means by which to identify spatial variation in canopy vigor at the study

vineyard. Of the three methods used to identify this variation, spectrally-based (NDVI), planimetrically-based (canopy extent), and three-dimensionally-derived (SfM point clouds), the latter two were most successful and would be recommended for future use. Most importantly, due to the low cost of the technology used to capture data for this study, the methodologies developed in this dissertation would be practical for implementation in other vineyards as well as in other areas of agriculture.

CHAPTER I

INTRODUCTION

Growing grapes, as with any crop, is by nature a geographically-dictated process. Worldwide, grapevines are grown in particular locations due to accommodating climate, slope, soil, and other physical site characteristics. Even at the most local of scales, within one vineyard or between a few vineyards in close proximity to each other, the physical characteristics that affect grapevines vary spatially (i.e. moisture, temperature, soil, etc.). As a result, the yield and quality of the harvest are also variable. In most cases, this variation remains unaddressed by viticulturists (vineyard managers) because of traditional homogenous crop management practices and an overall lack of awareness regarding this variation. To monitor and address spatial variation in vineyard performance, recent viticultural research integrates GIScience-based approaches and methodologies through the geospatial analyses and techniques provided by GIS and, more importantly, remote sensing. Remote sensing analyses have recently been shown to be an essential tool in monitoring and addressing vineyard crop variability by way of grapevine leaf canopy (Hall 2003). At the local scale, the variation in reflectance for the vine leaf canopy observed with remotely sensed images directly correlates with vine health and eventual vine performance through grape yield and quality (Hall 2003; Proffitt et al. 2006).

Background

Geography and Viticulture: Past and Present

As was previously mentioned, growing grapes is an inherently geographic process. Thus, geographers have studied viticulture, specifically its unique location-

determined characteristics otherwise known as terroir, for over a century (Morrison 1936; Weigend 1954; Peters 1984; Newman 1986). Such studies follow the regional tradition of geography, looking at the amalgamation of both human and physical or environmental factors that go into grape-growing and in some cases making wines (de Blij, 1983); for example, Newman (1986) summarized and reported the aspects that go into grape-growing and wine-making within the Finger Lakes American Viticultural Area (AVA) in central New York State as did Morrison (1936) in Ohio. In a much different light, recent geographically-based viticultural research trends have shifted from being descriptive and regional to being more technical, quantitative, and increasingly site-specific (Bramley et al. 2003; Hall 2003; Johnson et al. 2003b; Proffitt et al. 2006). Using geospatial tools and techniques, these new types of studies aim to address localized grapevine performance variability within a few or even a single vineyard block.

Variability in the Vineyard

All of the environmental factors that influence the grapevine like climate, slope, soil, drainage, etc. vary over space. As a result, grapevines produce fruit that varies spatially in regards to its quality and quantity (Hall et al. 2002; Proffitt et al. 2006). In essence, each vineyard and each vine within a vineyard faces a different set of circumstances (soil types, drainage, slopes, microclimate, etc.) that impacts the grapes produced there. Geographic tools and techniques have provided the ability to observe such differentials in grapevines. Site-specific remote sensing, for example, quantifies the spatial variability in the vine leaf canopy that is directly related to grape production quantity and quality (Hall et al. 2002, Bramley et al. 2003; Hall, 2003; Hall et al. 2003). Layer-based mapping systems like GIS visually enhance ground data for vineyard

managers, providing viticulturists snapshots of crop health across entire vineyard blocks. In most cases, ground data samples are interpolated to create a number of surfaces for proper and more thorough crop evaluation (Bramley et al. 2003; Proffitt et al. 2006). Grape yield, soil conductivity and salinity, juice pH, berry weight, and pruning weight have proven useful in vineyard spatial analyses (Bramley 2001; Dobrowski et al. 2003; Best et al. 2005; Proffitt et al. 2006). Grapevine variability is twofold however, not only does it vary over space; it varies over time due to its annual growth cycle.

Changes are also found in grapevines over time due to the natural perennial growth cycle that is observed throughout every season. Knowledge of phenology, or the growth stages, of the crop is essential to properly study temporal changes in grapevine health. (Coombe and Dry 1988; Mullins et al. 1992; Jackson 2008; Hall et al. 2011). Grapevine phenological cycles, dictate the periods within a growing season that the crop must be sampled and monitored (Mullins et al. 1992; Dry and Coombe 2004). For example, grapevines require a dormancy period wherein growth is not taking place. This is why grapes are typically only located at temperate latitudes of between 30 and 50 degrees north or south of the equator (de Blij 1983), consistent with the majority of deciduous plants. In succession, after a dormancy period of several months, budding occurs, buds break, leaves form, grapes grow, and sugar/acid levels increase within the grapes changing grape color soon before the harvest. Despite this change over time, the crop is still monitored, although this does provide challenges in sampling the crop. The timing of such grapevine phenology is dependent upon the particular season in which the crop is growing. In short, the amount of precipitation, sunlight, temperature, and many other factors dictate when the crop reaches each growth stage in a given season (Mullins

et al. 1992; Dry and Coombe 2004). Therefore, seasonal changes in the crop are rarely exactly the same as the previous year or years.

Current Research Areas

Three recent research areas have emerged that utilize geographic tools and techniques to address grapevine variability in structure, locational attributes, and health: (1) vineyard land use or vine row delineation, (2) vineyard site location and suitability modeling, and (3) precision viticulture. These three research avenues are distinct in purpose but are contextually and methodologically very similar. Therefore, it is important to be knowledgeable of methodologies from each research area, even if the research only falls into one of the three categories.

Land Use Delineation

Vineyard land uses are particularly unique due to the fact that in most cases they are made up of rows of vines (vine rows) and spaces between these rows of vines (inter-row spaces). This is due to the trellis training system onto which vines grow. This creates a discontinuous surface of vine leaf canopy and inter-row spaces of bare earth, grass, or a cover crop within the vineyard land areas. A number of studies have expressed the difficulties of locating such land uses via remotely sensed imagery of low, medium, and high-spatial resolutions (Trolier et al. 1989; Wassenaar et al. 2002; Delenne et al. 2010). The size of the pixels within the imagery is vital in this process (Hall et al., 2008). The pixels can be no bigger than the desired area of analysis (i.e. the size of the vine canopy, which is typically less than one meter in width). Smaller pixels translate to more easily identifiable features on the ground. Hall and Louis (2009) took this a step further by not only finding vineyard land areas, but also demarcating vine rows.

Excluding the inter-row spaces is desirable because these areas are not of interest, and by eliminating them, time spent processing and analyzing images is minimized. The most recent methodologies in this research area have bypassed image resolution issues by substituting imagery with airborne lidar (light detection and ranging) datasets (Mathews and Jensen 2012a). Use of similar point cloud based datasets for three-dimensional analyses of grapevine health has also been suggested (Mathews and Jensen 2012a).

Site Location and Suitability Modeling

Site location refers to what characteristics are found at actual vineyard sites. Site suitability uses known vineyard characteristics from literature or from studying site location in the same region to predict future vineyard areas in the same region. GIS provides an interface that allows the manipulation of multiple layers of information and the ability to create an optimal vineyard location index. Jones et al. (2004) and Kurtural et al. (2006) each presented such models in Oregon and Illinois respectively. Both used numerous layers of information such as slope, aspect, elevation, growing degree days, frost days, drainage, soil, and land use to create a suitability index specific to their area of interest. The index is created with the raster model by overlaying and performing map algebra (addition or multiplication) on all of the previously mentioned layers to create a master prediction layer (Kurtural et al. 2006). Some layers can be more heavily weighted so that the information in them is more influential than other layers as did Jones et al. (2004) with climate. The resultant master layer serves as the final index except in the case of excluding improper land uses and other improbable areas (Kurtural et al. 2006). To take this a step further, the final index can be ground-truthed using GPS to locate actual

vineyard sites (Jones et al. 2004). In general, GIS has proven to be a very useful tool in studying vineyard location attributes (Watkins 1997; Hellman et al. 2011).

Precision Viticulture

Precision viticulture is a relatively new subfield of precision agriculture that utilizes a number of geographic techniques and datasets to micro-manage spatial variation in grapevine performance (Lamb 2001; Bramley et al. 2003, Bramley et al. 2005; Proffitt et al. 2006; Hall and Hardie 2008). The recent boom in research and adoption of precision viticulture can be attributed to the advent of GPS technology as well as GIS software systems and the inherent spatial analysis capabilities that they provide. GIS surface or layer creation permits all types of spatial data to be viewed and analyzed (Proffitt et al. 2006). In addition, remote sensing analyses have been shown to add yet another useful tool to the precision viticulture management scheme (Lamb et al. 2001; Hall et al. 2002; Hall 2003; Proffitt et al. 2006), usually incorporating several spectral bands by way of calculating vegetation indices (Dobrowski et al. 2002; Zarco-Tejada et al. 2005) like the Normalized Difference Vegetation Index (NDVI; Rouse et al. 1973). Such indices are useful in estimating vegetation density (Hall et al. 2011) and subsequent photosynthetic capacity.

The precision viticulture design is based on four overlapping phases or steps: observation, interpretation, evaluation, and implementation (Bramley et al. 2003; Proffitt et al. 2006). The observation phase represents the data collection period where soil sampling, grape quantity and quality sampling, and image acquisition occurs. In the case of data captured at the individual grapevine scale, the interpretation step spatially interpolates information to output vine canopy vigor, soil, yield, and other maps for

evaluation. For imagery, interpretation is done by way of transformation with vegetation indices like NDVI to better gauge health differentials over the image. The evaluation phase assesses the spatial variability shown in all the created maps and constructs a plan to address it (i.e. through management zones or otherwise). Lastly, the implementation of the plan is carried out to improve the crop via more or less fertilizer, improved irrigation, zonal harvesting, etc. (Bramley et al. 2003; Proffitt et al. 2006). The implementation of the precision viticulture scheme has been shown to be profitable in a number of ways because it can decrease inputs (water, fertilizer, etc.) and increase or improve outputs like grape quantity and quality (Best et al. 2005); therefore, reducing costs and increasing profits (Bramley et al. 2003).

Remote Sensing of Vineyards

As discussed in the previous section, an abundance of research has focused on utilizing remote sensing techniques to better study vineyards; specifically in the context of land use (vineyard block) delineation and precision viticulture research. The types of studies that use remote sensing to look into grapevines include but are not limited to: land use and vine row delineation (Hall and Louis 2009; Delenne et al. 2010), disease detection (Zarco-Tejada et al. 2005), vine water status (Acevedo-Opazo et al. 2008), leaf canopy vigor assessment (Hall et al. 2002), and grape phenolics and yield prediction (Lamb et al. 2004; Cunha et al. 2010). Despite the many different uses of remote sensing techniques in vineyard studies, commonalities are present in regards to the researchers' choice of imagery utilized, how the imagery is processed and analyzed, and what outputs are generated. This is discussed in further detail in the chapters that follow.

Research Objectives and Chapter Outline

Following the most recent trend in viticultural research, precision viticulture, this study addresses the following three objectives at a study site in the Texas Hill Country American Viticultural Area (THCAVA) over the course of the 2012 growing season:

(1) craft a practical imaging system (digital cameras and unmanned aerial vehicle, UAV) and processing methodology to produce high quality multispectral (visible and near-infrared [NIR]) orthophotos of a study vineyard,

(2) use produced orthophotos, image segmentation, and NDVI to observe spatial and temporal variation in grapevine canopy health/vigor that can aid in improving vineyard management practice and eventual vine performance (i.e. yield), and

(3) develop a new, three-dimensional method for visualizing and quantifying vineyard canopy density.

Objective 1 addresses image acquisition in the field and the plethora of factors and considerations that impact accurately imaging and analyzing vineyard vegetation canopy. This includes use of lightweight digital camera sensors mounted on a UAV to collect aerial imagery in four spectral bands (blue, green, red, and NIR). This also includes processing the collected imagery to create spectrally standardized image mosaics of the study site from several sample periods during the 2012 growing season.

Objective 2 entails the analysis of the created imagery in the first objective to identify spatial variation in crop health/vigor throughout the study vineyard. This includes exploring correlations between orthophoto-based canopy metrics and on-ground measured harvest data. Maps will be produced to visualize the spatial variation in vine performance at the study site.

Objective 3 assesses the applicability and practicality of three-dimensional modeling (visualization and quantification) of grapevine canopy; in particular, exploring whether or not leaf area index (LAI) can be estimated with such 3D data. This objective utilizes the same aerial image data as collected in objective 1 to create lidar-like point cloud datasets using the relatively new Structure from Motion (SfM) technique to be discussed in-depth in the chapters that follow.

This dissertation is presented in chapter form in the following manner: the current chapter (Chapter I) presented general literature in the research area, current research trends, specific objectives of this research, and the study site, Chapter II addresses research objective 1 creating an UAV-based aerial image capturing system and data flow methodology to create useful aerial image products, Chapter III presents research objective 2 in analyzing the spatial data created in Chapter II to explore spatial variation in crop performance, and Chapter IV creates and utilizes a 3D-based vineyard dataset to predict per-vine canopy LAI and visualize vineyard canopy. More specific literature is presented within each of the body chapters (II, III, and IV) to better provide specific context pertaining to the different topical areas that aided in crafting the methodologies employed. Lastly, Chapter V provides the overarching conclusions of the entire dissertation as well as recommendations to viticulturists interested in using such methodologies.

Study Site

The THCAVA was recognized in 1991 and is located in south-central Texas west of Austin and north of San Antonio. This AVA contains 22 wineries, encompasses parts of 22 counties, and covers an area of over 36,000 square kilometers (14,000 square

miles). Two consecutive vineyard blocks managed by one winery are the focus of this dissertation. The specific location of the study vineyard is not disclosed as requested by the property owners. Anonymity was preferred in this case because of the competitive nature of the wine industry. Permission for vineyard access and research collaboration was granted during the fall of 2011. The vineyard manager and winemaker served as the main contacts and the on-site persons with which discussions were held throughout this research. This study focused on two blocks of trellis-trained Tempranillo (*Vitis vinifera*) vines totaling 1.9 hectares (4.8 acres). Hereafter, all data collection and analysis are contained within these two vineyard blocks. Study site maps and more detailed site descriptions are provided in Chapters II-IV.

CHAPTER II

IMAGING SYSTEM SET-UP, CALIBRATION, AND APPLICATION IN THE VINEYARD[1]

Introduction

Use of Compact Digital Cameras in Remote Sensing

The low cost and high availability of compact (point-and-shoot) digital cameras has led to usages beyond that of recreational or professional capture of natural color photography (Dean et al. 2000). Digital camera ease of operation, speed of image capture, efficient processing, and lightweight design lend utility to aerial image capture (King 1995). Coupled with an unmanned aerial vehicle (UAV) to create an unmanned aerial system (UAS), digital cameras can inexpensively provide very high spatial and temporal resolution data for research in soils (Levin et al. 2005), tree inventory and biomass (Dean et al. 2000), land management (Rango et al. 2009), and agriculture (Hunt et al. 2008; Lebourgeois et al. 2008; Lelong et al. 2008; Ritchie et al. 2008) including viticulture (Smit et al. 2010; Turner et al. 2011). See Everaerts (2008) and Watts et al. (2012) for informative reviews on UAV and UAS technology. Camera system design for UAV-based remote sensing varies by the nature of the images to be captured; as evidenced by studies that alter digital cameras for their specific needs, while others employ cameras with off-the-shelf configurations. With or without modification, digital cameras remotely record spectral information of a target of interest (Dean et al. 2000; Levin et al. 2005; Ritchie et al. 2008). Levin et al. (2005) utilized an unaltered digital camera (UDC) to record the spectral properties of soils with three spectral bands of blue,

[1] This chapter was accepted for publication with the title "A practical UAV remote sensing methodology to generate multispectral orthophotos for vineyards: Estimation of spectral reflectance using compact digital cameras" in the *International Journal of Applied Geospatial Research* (Feb. 1, 2014).

green, and red. Most digital cameras, however, have the ability to sense wavelengths beyond the visible spectrum with minor alteration (Cheng and Rahimzadeh 2005).

A typical digital camera has the following vital components: a sensor (either a charge-coupled device [CCD] or a complementary metal oxide semiconductor [CMOS]) made up of an array of sensor elements or sensels (each of which later become picture elements or pixels in the captured image), a Bayer filter (or other color filter), a lens, and a hot mirror. This study focuses on the CCD sensor, which senses light and converts this spectral information into digital numbers (DNs), typically with 8-bit radiometric resolution (0-255). The Bayer filter is responsible for splitting the incoming visible wavelengths into separate bands so brightness for each can be recorded (i.e., blue, green, and red; stored in reverse order and referred to as RGB). The lens de-magnifies the scene to properly represent physical objects and their geometric relationships within a captured image. The hot mirror is an internal spectral filter that limits detector sensitivity to visible wavelengths (i.e., the sensor will not record energy in the near-infrared [NIR] region). In most cases the hot mirror wavelength cut-off is somewhere around 670-690 nm (Dean et al. 2000; Ritchie et al. 2008), whereas most CCDs have a spectral range up to 900 nm (Dare 2008; Lelong et al. 2008). Therefore, the hot mirror forces the CCD to sense only the desired portions of the spectrum to more easily replicate the visible light range for natural color photography. For studies that require NIR sensitivity, the hot mirror can be removed and replaced with clear glass to allow the CCD to sense NIR wavelengths (Cheng and Rahimzadeh, 2005). In the case of vegetation studies for instance, NIR sensitivity is important to be able to monitor differentials in crop health, thus the hot mirror must be replaced (Dare 2008; Ritchie et al. 2008). System designs

must be creative to integrate the NIR band usually by use of two cameras. Ritchie et al. (2008), for example, employed an UDC combined with an altered digital camera (ADC) to gather four spectral bands for analysis (UDC—blue, green, red; ADC—NIR).

Image format is another important image acquisition consideration when using digital cameras as remote sensors. Image format is important because compression of images alters the way DNs are computed and stored (Dean et al. 2000). RAW and TIFF image formats are presumed to be better because they do not alter the image (Cheng and Rahimzadeh 2005; Lebourgeois et al. 2008). RAW and TIFF images are made up of unprocessed, uncompressed pixel data as captured by the CCD. The downsides to such measurements are increased file size and capture time (Lelong et al. 2008). An alternative to RAW and TIFF formats is JPEG, which has proven adequate for scientific analyses (Hunt et al. 2005; Lelong et al. 2008; Levin et al. 2005). Compared to other formats, JPEG offers the convenience of small file size, quick capture ability, and easier processing.

Improving the Quality of Collected Images

Regardless of the type of sensor employed, radiometric and geometric effects must be addressed in the processing of aerial imagery to properly create image products for future analysis. Radiometric corrections aim to remove inconsistencies produced by (1) atmospheric effects like scattering and/or absorption of incoming or reflected energy between the sensor and the surface, and (2) topographic effects that may create shadowing and other unequal reflectance over space within the collected images (Jensen 2005). Geometric corrections address internal and external errors caused by the sensor and aircraft (Jensen 2005). Internal errors are predictable and therefore easier to correct

like distortion created by the camera lens. External errors are flight-dependent and include altitude changes as well as sensor viewing geometries dictated by aircraft attitude. External errors are accentuated in UAV image capture due to low flying heights and reduced control of in-flight motion (Lelong et al. 2008). Low flying height also results in small image footprints, which requires mosaicking of images to create the desired ground coverage (Laliberte et al. 2011; Turner et al. 2012).

Radiometric Corrections

"Radiometric calibration of a sensor involves determining the relationship between image brightness as measured in digital image units [DNs] and actual radiance or reflectance of the target" (King 1995, p. 258). This is normally completed by capturing known spectral targets during flight and establishing a correlative relationship with in situ spectroradiometer measurements (King 1995; Smith and Milton 1999). Conversion to spectral reflectance allows for a standardized method by which quantitative comparisons can be made over time with accuracy and confidence (Smith and Milton 1999). One method of conversion is the empirical line method (Jensen 2005; Smith and Milton 1999). This method assumes that targets of differing reflectance are captured by the sensor that can be compared to actual target reflectance as measured by a spectroradiometer. At the very least one spectral target with very low reflectance (dark) and one with very high reflectance (light) should be included in the scene. Spectral targets with reflectances along the spectrum between the light and dark objects are encouraged to be included, not forgetting that similar variation must exist in NIR reflectance (if NIR calibration is necessary). The empirical line method essentially correlates brightness measured with the CCD to reflectance measured by a

spectroradiometer. Linear regression is then used to create a slope line equation to predict reflectance of non-target pixels (Karpouzli and Malthus 2003; Smith and Milton 1999). Each band of imagery requires a different prediction equation "which attempt to remove both illumination and atmospheric effects" that can then be "applied to the remotely sensed data to produce images in units of [relative] reflectance" (Smith and Milton 1999, p. 2654).

In the case of using digital cameras as remote sensors, the empirical line method has proven practical and successful in a number of instances (Levin et al. 2005; Ritchie et al. 2008). Levin et al. (2005) utilized repeating targets (plastic chips) of black, gray, white, blue, green, red, and also a known 100 percent reflectance target, whereas Ritchie et al. (2008) used a ColorChecker chart with 24 standardized colored squares as reflectance targets. These targets were designed for small-scale calibration of digital camera images taken on-the-ground. The difficulty with this method in the case of digital cameras for quantitative research relates to the properties of the digital camera sensor that are, for the most part, unknown and unpublished by the manufacturer, specifically the wavelength interval captured by each band. Lelong et al. (2008) were fortunate to know the properties of the sensor they employed: a Canon EOS-350D with blue (420-500 nm), green (490-580 nm), red (570-640 nm), and NIR (720-850 nm) bands. Levin et al. (2005), however, did not know this information and were therefore forced to select specific wavelengths that were assumed to best represent and correlate with DNs from each band collected by the CCD: Olympus Camedia C-920 with blue (460 nm), green (510 nm), and red (640 nm) bands. Jensen et al. (2007) provided an example of a typical

CCD sensitivity that showed blue centered on 450 nm, green on 550 nm, and red on 650 nm, with each band exhibiting a wavelength interval of around 80-120 nm.

After this calibration, large-scale targets can be captured within aerial imagery such as tarpaulins or other specially designed spectral targets to aid in conversion to reflectance of field captured imagery. These targets must cover substantial area on-the-ground depending on the spatial resolution of the imagery (Hunt et al. 2008). With small-footprint UAV imagery, Laliberte et al. (2011) noted difficulty capturing targets within all images. In converting UAV image DNs to reflectance using spectral targets, Laliberte et al. (2011) found estimates to be more accurate when the conversion was applied to the entire mosaic rather than to single images (prior to mosaicking).

Prior to conversion to reflectance, correction for vignetting within each image may be necessary. Aerial imagery collected by digital cameras often displays a radial pattern of brightness falloff near the image edges that can vary based on exposure (Kelcey and Lucieer 2012). Vignetting corrections range from producing and applying anti-vignetting filters (Lelong et al. 2008) to the complete removal (masking) of edge pixels (De Biasio et al. 2010), although leaving images unaltered and not correcting for vignetting is not uncommon (Turner et al. 2012). Other radiometric issues including general brightness differences between collected images can be addressed with color balancing and/or histogram equalization (Niethammer et al. 2011), although such brightness adjustment is not always a part of mosaicking methodologies (Rango et al. 2009; Turner et al. 2011; Turner et al. 2012).

Geometric Corrections

Internal geometric errors like radial and tangential distortions created by digital camera lenses are less predictable and stable than traditional aerial photograph sensors, but are still able to be estimated and corrected (Turner et al. 2012). Kelcey and Lucieer (2012) for instance used the free software Agisoft Lens (Agisoft LLC, St. Petersburg, Russia) to calculate lens distortion coefficients and apply a correction to their UAV images, although the literature indicates this correction is often ignored. Other sources of error such as external geometric errors are consistently present with UAV collected data because of the difficulty of maintaining consistent flying height, roll, pitch, and yaw (Lelong et al. 2008; Turner et al. 2012), which leads to image mosaics with differing spatial resolution and viewing angles. Selectivity in regard to which images to include in the mosaic becomes important (i.e., nadir-only at or near the same flying height; Turner et al. 2011; Turner et al. 2012).

Proper georectification of UAV collected images is traditionally based on a highly accurate digital terrain model (DTM) of the imaged area. UAV-based methodologies have benefitted from recent advances in Structure from Motion (SfM), which much like traditional photogrammetry utilizes image overlap from multiple perspectives of the collected images to identify keypoints (Snavely et al. 2008) and generate an accurate point cloud model of the surface (Kaminsky et al. 2009). Once georeferenced, SfM point clouds can be filtered and interpolated to create highly accurate, site-specific digital terrain models (DTMs; Mathews and Jensen 2013) and/or digital surface models (DSMs; Dandois and Ellis 2010) upon which image mosaics are georectified (Turner et al. 2012).

Adjustment of imagery to the DTM accounts for any topographic effects at the image site (Baboo and Devi 2011).

Objective

The objective of this paper was to design a practical and inexpensive data collection and processing methodology to generate orthophotomosiacs with multiple bands each with pixel values in units of reflectance. This was completed using only compact digital cameras and a small UAV, which is contrary to similar studies that utilize specialized, more expensive sensors and UAVs (Baluja et al. 2012; Bellvert et al. 2013; Primicerio et al. 2012; Turner et al. 2011). Ultimately, the system would have the ability to collect very high spatial resolution aerial imagery (less than 10 cm) in four spectral bands (blue, green, red, and NIR), each of which could be converted to estimates of reflectance using the empirical line method. To address the objective, this paper is presented in two parts: (1) on-ground camera testing to determine the sensitivity and capability of the digital camera sensors and (2) application of the camera system in the field to create spectrally-consistent orthophotos of a study vineyard site in the Texas Hill Country. A per-band validation was implemented to gauge the quality of each of the four collected bands for future analyses. A per-band validation is contrary to similar research that evaluates orthophoto quality using NDVI or other vegetation index values (Hunt et al. 2005; Primicerio et al. 2012). This UAV and digital camera system design was aimed at identifying spatial heterogeneity in grapevine canopy vigor across vineyards, however, it could be used for a number of applications that require very high spatial resolution imagery with visible and NIR bands (precision agriculture and crop management, small area land cover change, etc.).

Materials and Methods

Digital Cameras

This study utilized two Canon PowerShot A480 compact digital cameras (Canon U.S.A., Inc., Lake Success, NY, USA), one UDC and one ADC. The A480s have a resolution of 10 megapixels (3648 by 2736 pixels) with a 1/2.3-inch type CCD sensor and cost approximately $150 USD each. The ADC was purchased with the hot mirror removed and replaced with clear glass as described by Cheng and Rahimzadeh (2005). The same model camera (A480) was utilized for both the UDC and ADC to consistently replicate potential geometric (focal length, megapixels) and spectral (sensor, Bayer filter) distortions between cameras.

Following Levin et al. (2005) and Ritchie et al. (2008), all UDC and ADC images were captured on manual setting with sunlight white balance and no image adjustment. In addition, the UDC ISO level was fixed at 80. The ADC ISO level was fixed at 400 due to the speed of the UAV carrying the camera, increasing the cameras' ability to effectively capture the scene. All images were captured in JPEG format following Levin et al. (2005). Although JPEG format undergoes compression which may slightly alter the saved data, JPEGs provide the most practical means to capture hundreds of aerial images while in-the-field due to its quick recording ability and smaller file size. This is contrary to RAW files, which in testing needed several more seconds per image to save and were around three times larger in file size (JPEG: 2-5 MB, RAW: 15 MB). The high speed capturing ability is necessary when using faster moving aircraft like planes to ensure proper image overlap.

Four spectral bands were captured: blue, green, red, and NIR. Like Ritchie et al. (2008), both cameras were utilized to obtain these bands with the UDC capturing the three visible bands and the ADC capturing three NIR bands. To block visible wavelengths from being sensed by the ADC, a NIR-transmitting filter was placed in front of the ADC lens similar to Dean et al. (2000). This filter permitted the ADC CCD to only sense wavelengths 750 nm and longer. As was discussed previously, presumably most digital camera sensors (CCDs) cannot sense wavelengths greater than 900 nm, which forced the ADC to collect three bands (still assigned as RGB) within this 750-900 nm range. Placing the NIR filter on the outside of the camera, instead of replacing the hot mirror with a NIR filter, was preferred so other spectral filters (i.e., red) could be implemented during future acquisitions.

On-Ground Image Collection and Camera Calibration

Ground-based calibration data were collected on two cloud-free days near noon: 23-November-2011 at 11:30 AM and 27-November-2011 at 12:45 PM. Data were captured at the Texas State University campus in San Marcos, Texas, USA (29°53′18″N, 97°56′32″W). On both occasions, the following datasets were collected: (1) 2-3 images from both cameras capturing within the field of view (FOV) a calibration panel of color targets, a known 100 percent Spectralon reflectance target, and two leaves for distinct NIR response, and (2) spectroradiometer readings of each of these objects. The calibration panel of spectral targets was crafted out of black, gray, white, purple, yellow, blue, green, and red paint swatches affixed to foamboard (near-Lambertian surfaces as suggested by Smith and Milton 1999). The swatches were collected from a local hardware store and exhibited a flat color finish. Each color square was 5 cm by 5 cm.

Two of each color swatch were included to account for variability in spectral response. Calibration panel design was similar to the set-up produced by Levin et al. (2005).

Images were taken perpendicular to the targets (nadir) at a distance of approximately one meter (see Figure 2.1a-b for sample images). An ASD FieldSpec Pro spectroradiometer (Analytical Spectral Devices, Inc., Boulder, CO, USA) collecting a value for every nanometer within a spectral range of 350-1050 nm was utilized to collect spectral signatures of the objects immediately following image capture. The ASD device consisted of a backpack unit and a fiber optic cable connected to a 25° field of view handheld optic (pistol-grip with integrated leveler for nadir positioning). Measurements were logged with a connected laptop computer. Throughout spectroradiometer data collection for on-ground and aerial-based calibration and validation, measurements were taken by a single operator standing on the far side of the sun to avoid casting shadows into the measurement area (McCoy 2005). Data were collected as values of reflectance by regularly calibrating the ASD with the Spectralon reference panel. Measurements of spectral targets were taken at nadir approximately 10 cm above each target aimed at the center of each target. A minimum of two measurements were taken of each target and later averaged. DNs were obtained for each target using ENVI 4.8 (Exelis, Inc., Boulder, CO, USA) to define 19 regions of interest (ROI) as shown in Figure 2.1a. ROIs were drawn central to each target area to avoid adjacency effects (Dean et al. 2000; Levin et al. 2007). The mean DN value was taken from each ROI to represent each target. Single images from each sample were used to calculate mean DN after observing minimal variation in DNs across images within each sample.

Mean DNs were then compared to spectroradiometer-measured reflectance for each band. Both cameras used a Bayer filter to capture three bands of data (UDC—blue, green, red and ADC—NIR [called ADC-Blue], NIR [ADC-Green], NIR [ADC-Red]). The three NIR bands recorded DNs for energy reflected within a 750-900 nm interval. The optimal NIR band, to be used in future analysis, was chosen based on the linear relationship between DNs and spectroradiometer measurements. The band with the highest R^2 value was chosen as the best representation of the NIR wavelengths. The optimal wavelength interval for each band was determined by testing a series of wavelength intervals. Tested intervals for each band were centered on 450 nm (blue), 550 nm (green), 650 nm (red), and 850 nm (NIR) following the typical CCD sensitivity illustrated by Jensen et al. (2007). The following wavelength intervals were tested for the blue band from narrow to wide: 450 nm, 445-455 nm, 440-460 nm, 420-480 nm, and 400-500 nm. Similarly, the same intervals were used for the other bands (i.e. green: 550 nm, 545-555 nm, 540-560 nm, etc.; red: 650 nm, 645-655 nm, etc.), except for narrow intervals in the NIR band (850 nm, 845-455 nm, and 840-860 nm) because the wavelength interval range was more confidently known. These intervals determined the range at which spectral signatures captured by the spectroradiometer would be averaged and compared to mean ROI-specific DNs for each target.

The relationship between spectroradiometer-measured reflectance and camera recorded DNs was modeled using linear regression (R^2) and root mean square error (RMSE). This was completed for both samples to account for any variability that may exist with the digital camera and spectroradiometer measurements over time. For each band, the wavelength interval with the best combination of R^2 (high) and RMSE (low) for

both samples was selected as the most representative wavelength interval. These wavelength intervals were then used with in situ spectroradiometer measurements to convert aerial image DNs to reflectance using the empirical line method.

Application of UAV-Based Image System to the Study Vineyard and Generation of Analysis-Ready Image Products

Study Site and Data Collection

The vineyard study site is located in the Texas Hill Country American Viticultural Area near Fredericksburg, Texas, USA (120 km west of Austin). This study focused image collection on two contiguous vineyard blocks consisting of 38 vine rows each with up to 95 vertical trellis-trained 4-6 year-old Tempranillo (Vitis vinifera) vines covering approximately 1.9 ha (4.8 acres). Figure 2.2 shows the vineyard layout with the study vines outlined in red. The study blocks are separated with a dotted red line. The eastern block is older than the western block and provides desirable variation in canopy size and reflectance characteristics. At the time of data collection, the area beneath the vine canopies consisted of bare soil, while the inter-row space was covered in grass. The vineyard has a gentle slope from its highest point in the northwest corner to the lowest point in the southeast corner.

Aerial images of the study vineyard were captured using the previously discussed digital cameras mounted (at separate times) on a Hawkeye UAV (www.ElectricFlights.com, Kingsland, TX, USA; see Figure 2.3a-b). The Hawkeye is a lithium battery-powered kitewing plane with a 1.5 m wingspan, single rear-facing propeller, and single nadir-facing camera mount. The Hawkeye was flown both autonomously with pre-programmed autopilot and manually. Ardupilot (code.google.com/p/ardupilot/) was used to allow for autopilot capability. This Arduino-

based, open-source hardware and software combination based its flight path on pre-programmed, ordered waypoints (X, Y, and Z coordinates). When autopilot was switched on, Ardupilot controlled the UAV autonomously using the on-board GPS and the waypoint locations. When flown on autopilot, the Hawkeye is prone to becoming stagnant in gusty winds, particularly when flying into the wind. Manual flight control, therefore, was initiated during wind gusts to avoid unnecessary reduction in ground covered and battery power loss. Takeoff and landing were also manually controlled. To launch the UAV, the Hawkeye was thrown forward at shoulder height with the propeller running and manual control initiated. After gaining altitude under manual control, autopilot was enabled with a switch on the remote control. The autopilot was pre-programmed to follow the flight path provided in Figure 2.2. Flight paths were orientated north-to-south to keep the UAV flying directly into or with the winds, serving to steady the aircraft and capture higher quality images. Otherwise, the UAV was likely to sway and decrease the cameras ability to capture nadir images. Upon completion of aerial data collection manual flight control was reinitiated, the altitude of the UAV was gradually decreased, the UAV was guided to touchdown in the landing area and retrieved.

Prior to image capture, several spectral targets were placed along the northeastern edge of the vineyard to aid the empirical line method transformation. Six flat, colored foamboard spectral targets sized 0.75 m by 0.5 m (black, white, grey, blue, green, red) were placed on flat ground spaced about 2 m apart near the takeoff/landing area (see Figure 2.2). The targets were large enough to ensure that many pure pixels would represent each target within the captured images that could then be averaged and compared to measured reflectance. Other targets were placed in the field to help

georeference the collected imagery. Five total ground control points (GCPs) were positioned following Mathews and Jensen (2013). Locations of the GCPs are shown with X's in Figure 2.2 at the corners and eastern edge of the study vineyard. The 0.6 m by 0.6 m GCP targets were crafted out of durable foamboard and painted with flat hues of red, and small concentric black and white circles at the center, similar to Aber et al. (2010). These highly visible targets were easy to find in aerial images and served to provide additional spectral targets to aid in SfM keypoint matching as well as conversion of DNs to reflectance. GCPs were located using a Trimble GeoXH GPS with an external Zephyr antenna that averaged 200 separate positions for each location (X,Y: NAD83 UTM Zone 14N; and Z: NADV88). Acquisition of GPS positions was limited to a maximum position dilution of precision (PDOP) of three. Following GPS data collection, differential correction was completed using the Trimble GPS Analyst Extension in ArcGIS (ESRI, Redlands, CA, USA).

UAV-based aerial images were captured under clear skies on 16-May-2012 at approximately 11:00 AM to minimize shadowing between the vine rows. At this time of the growing season the vines were flowering, which has served as a useful time to gauge relative vine health and eventual production (Hall et al. 2011). Images were captured at a flying height of approximately 125 m and before noon due to lower wind speeds at that time (around 15 kph). Images were captured within two 15 minute time periods coinciding with the life of each lithium battery. Upon landing, the UAV battery and cameras were switched to continue capturing data. Images were automatically captured every second throughout flight using the Canon Hackers Development Kit (CHDK;

chdk.wikia.com) intervalometer script preinstalled on the camera SD cards. During aerial image collection, camera settings remained the same as were used for on-ground testing.

Immediately following image capture, spectroradiometer data were collected at the vineyard site with the ASD FieldSpec Pro. A minimum of two measurements of each of the spectral targets, including the red portion of each GCP, were collected and averaged. A stratified sample of vine measurements was implemented for every fifth row starting with the first row (easternmost) and ending at row 30. Within rows, every tenth vine was sampled starting from the northern end of the vine rows (alternating starting vines from first to fifth vine; i.e. row 1-vine 1; row 1-vine 10; row 5-vine 5; row 5-vine 15; etc.). Vine canopy reflectance was sampled by aiming the spectroradiometer pistol-grip fiber optic sensor at a level nadir direction approximately 0.5 m above the vine canopy directly above the vine trunk. At this height above the canopy, the spot or target size of the ASD optic was around 0.23 m in diameter similar to vine canopy measurements taken by Rodríguez-Pérez et al. (2007). The sensor was then moved slightly to cover more vine canopy area and account for variation in spectral response. Multiple measurements were also captured to account for variation due to wind and potential canopy movement (McCoy 2005). Two to four observations of each vine canopy were taken and averaged. The same procedure was used to sample each vine. All samples were taken with the ASD spectroradiometer by the same operator standing on the far side of the canopy (in relation to the sun) to not cast shadows into the vine canopy being sampled. In total, the spectral signatures of 61 vine canopies were collected. The sampled vine locations (vine trunks) were located using the previously discussed GPS

unit and processing method with the number of averaged positions reduced from 200 to 30.

Data Processing

The data processing workflow from UAV image capture to export of the final orthophotos is provided with Figure 2.4. The same processing chain was completed separately for both the RGB and NIR images. After capturing aerial images of the vineyard site, a cursory manual image filtering was employed to remove any non-nadir images and other poor quality (blurry) images caused by aircraft motion. This image subset was used throughout the rest of the processing. Image histogram equalization was applied to the image subset to account for any brightness differences between individual images using ERDAS ImageEqualizer (Intergraph Corp., Madison, AL, USA). ImageEqualizer collects image statistics for all of the images and applies a normalization procedure prior to exporting new, radiometrically-adjusted images. Without such spectral adjustment, spatial heterogeneity in surface reflectance was visually apparent in the output mosaics (see Figure 2.5). Figure 2.5a displays increased brightness in the central-western portions of the study vineyard. Brightness variation is also apparent in the NIR imagery (Figure 2.5c) in the southernmost parts of the study vineyard. Histogram equalization served to correct such image-to-image brightness variation (Figure 2.5b,d). This normalization also served to minimize the effect of vignetting by brightening pixels near image edges.

Following image normalization, images were aligned using Agisoft PhotoScan (Agisoft LLC, St. Petersburg, Russia). PhotoScan provides a SfM-based automatic image alignment procedure that creates point clouds with arbitrary coordinates. Input

images are corrected for internal geometric distortions in PhotoScan by automatic import of digital camera EXIF data on lens and focal characteristics (applies lens distortion coefficients). Across the input images, point clouds for RGB and NIR images were created. Following point cloud creation, manual editing was necessary to remove obvious outlier points or noise (usually well above or below the ground surface). SfM point clouds typically include noise that necessitates removal (Dandois and Ellis 2013; Mathews and Jensen 2013).

Following noise removal, the point clouds were georeferenced within PhotoScan by manual identification of the GCP targets within images and by inputting their respective UTM coordinates. PhotoScan then transformed and optimized the point cloud with arbitrary coordinates to real-world UTM coordinates (X,Y,Z). Within PhotoScan, geometry was then built to both (1) create the underlying DTM surface onto which orthophotos were rectified/generated, and (2) determine the spatial resolution (pixel size as well as pixel array layout and image coverage) of the output orthophoto by analyzing the input images. In PhotoScan, the DTM surface was derived by creating a mesh from a simplified/filtered version of the point cloud (like a TIN). The spatial resolution of the orthophotos was determined by the lowest altitude image within the image set. This image exhibited the highest spatial resolution that all of the other images were upsampled to.

At this stage, preliminary RGB and NIR orthophotos were exported from PhotoScan, which include all input images blended (mean DNs at edge overlap). Figure 2.4 specifies further manual editing at this point, specifically trial and error image masking or removal of undesirable areas within images (i.e., vignetting corners if still

present, areas of distortion). This was necessary because the geometry of vineyards and similar row crops provide a difficult surface to automatically create orthophoto mosaics from due to the canopy being elevated above the ground surface on a trellis system. This elevated canopy combined with the wide FOV of the digital cameras created areas of high distortion within images. In images captured with an area array like a CCD, distortion naturally occurs in the pixels away from the principal point. This is further accentuated in UAV imagery due to low flying height and variability in aircraft attitude. Figure 2.6 shows a more traditional example of aerial image capture of vineyards where in this case one image captured the entire vineyard within its FOV (black camera at or above 250 m flying height). In this case, all of the vine rows would look to be near-planimetrically correct because they fall with a "usable" field of view (UFOV) showed with dark lines extending from the FOV to the ground surface (Figure 2.6), without the appearance of "leaning" vine rows away from the principal point. In the case of UAV-captured images at an altitude of 125 m (ideal locations shown with black cameras in Figure 2.6), these areas of distortion within images are increased due to the UFOV shrinking with reduction in altitude. In this example, instead of the whole vineyard being successfully imaged, only five rows of vines are accurately represented (multiple images needed with mosaic). This is further complicated by the more realistic picture of UAV camera geometry (gray cameras in Figure 2.6) where flying height is inconsistent and not every image is perfectly nadir-facing. A significant amount of manual masking (within PhotoScan) of unusable areas of images (outside the UFOV) within both the RGB and NIR image sets was necessary. In some extreme cases, entire images were completely excluded from production of the final orthophoto.

The final orthophotos (two mosaics) were exported from PhotoScan following the trial/error masking process: a RGB mosaic from the UDC images and a NIR mosaic from the ADC images. The ADC-Blue and ADC-Red bands were dropped from the NIR orthophoto since ADC-Green was determined to best gauge NIR. All three NIR bands were kept in the earlier stages of processing to aid SfM image alignment, which was more successful with the additional pixel information provided by multiple bands. Average DNs of spectral targets were collected from all four bands avoiding target edge pixels. Mean DNs were compared to measured reflectance to create linear regression models to transform each band's pixels from DNs (0-255) to percent reflectance (0-100). All six spectral targets were intended to be included in creation of all slope line equations as suggested by Smith and Milton (1999), but this was only completed for the NIR band. For the visible bands, two dark objects (black target; GCP red target for the blue and green bands, blue target for red band) and one light object (white target) were used due an observed tendency of the visible bands to over- and underestimate brightness of color targets. The non-black dark targets were chosen based on having at or near the same recorded brightness as the black target. Regression equations were created for each band and applied to every pixel in that band using the raster calculator in ArcGIS.

Output Validation

Using the output mosaics and spectroradiometer measurements, each output band was validated to compare measured reflectance to estimated reflectance. Validation ROIs were obtained for each vine location using 0.48 m diameter buffers of the GPS-located vine trunks. More narrow and broad buffers were tested (no buffer, 0.12 m, 0.24 m, and 1 m), but were considered less representative of the canopy size and spectroradiometer

FOV (multiple measurements over the canopy). This 0.48 m buffer size was near the extent of the canopy width for most vines, although smaller canopies and canopies with sizable gaps bring in the possibility of spectral contamination from underlying soil. All pixels with centroids within the 0.48 m buffers were averaged and compared to spectroradiometer-measured reflectance. In addition to vine samples, reflectance values from on-ground spectral targets not included in the DN to reflectance conversion were also compared (including GCP targets and other color targets like blue, green, and red). Linear regression was used to compare each band's estimated and measured reflectances and determine the suitable bands for future analyses.

Results

On-Ground Image Collection and Camera Calibration

Results from the wavelength interval analysis for the visible bands are provided in Table 2.1. The wavelength intervals determined to best represent the sensor for each band are displayed in bold. The blue band accounted for a significant amount of variation, especially within narrow wavelength intervals. The 440-460 nm interval was selected as the best fit between samples with R^2 and RMSE values of 0.937 and 8.250 for sample 1 and 0.923 and 9.628 for sample 2. Although, the interval of 445-455 nm and single wavelength of 450 nm had slightly higher R^2 values, these were considered to be less robust due to greater variation between samples 1 and 2. The green band DNs exhibited a strong relationship with spectroradiometer measurements contained with a relatively wide interval of 500-600 nm, yielding R^2 and RMSE values of 0.973 and 6.057 for sample 1 and 0.965 and 7.242 for sample 2. The red band R^2 values were the most consistent among the different wavelength intervals, with R^2 of 0.974 and 0.960. The

620-680 nm range was chosen based on the combination of high R^2 and low RMSE. Overall, the blue band was slightly less successful in correlating DNs with measured reflectance (R^2 less than 0.94) when compared to the green and red bands (both with R^2 greater than 0.96).

The ADC provided three NIR bands, of which the green band (regardless of wavelength interval) consistently provided DNs that highly correlate with measured reflectance (Table 2.2). The ADC-Green band was therefore used as the NIR band throughout this paper (hereafter referred to as just 'NIR'). Within this band, the widest wavelength interval had the highest R^2 values accounting for greater than 98% of the variation in measured reflectance of both samples. RMSE values for this wavelength interval also were desirably low (3.587 and 4.220).

Using the selected wavelength intervals, the per-band relationships between DNs and reflectance are provided in Figure 2.7(a-d). In each case, all of the 19 ROIs are plotted twice (once for each sample). For each band there was a noticeable offset between the origin and where the fit lines intersect the X-axes. This was present with all bands. For each band the dark object (black spectral target) registered mean DNs greater than zero, meaning that the digital cameras measured the dark objects as being more reflective than expected when compared to the spectroradiometer measured reflectance. The low RMSE and high correlation for the NIR band are graphically demonstrated with observations falling close to, or on the fit line. However, this is not the case with the visible bands, where less variability in spectroradiometer values was accounted for by the regression models. Additionally, the spectral signatures of several of the calibration panel targets are shown in Figure 2.8 (the first blue, green, red, leaf, white, and black

targets). The spectral sensitivities of the UDC and ADC are provided, within which the selected wavelength intervals for each band are displayed.

Application of UAV-Based Image System to the Study Vineyard and Generation of Analysis-Ready Image Products

Orthophoto Generation and Per-Band Reflectance Conversion

Of the 150 total RGB images collected, 59 were selected as high-quality and nadir or near-nadir facing, which were used in model creation. In total, 25 of these images were used to export the final orthophoto mosaic. As for NIR, 45 of the 191 images captured were used to create the NIR model. Of this subset, only 13 images were needed to create the NIR orthophoto. Fewer images were needed for NIR because the NIR flight yielded higher quality images overall, mostly attributed to more consistent, slightly higher flying height (due to reduced winds during the NIR flight). This resulted in the NIR orthophoto having a lower spatial resolution. Both orthophoto mosaics yielded spatial resolutions of less than 4 cm. The RGB images had a resolution of 2.59 cm, and the NIR image had a resolution of 3.45 cm. Orthophotos were converted from DNs to reflectance using the equations for each band provided in Table 2.3. The light and dark targets used for the empirical line conversion yielded R^2 of 0.98 or greater for all bands (all models $p <= 0.085$). Each band of the converted, final orthophotos of the study vineyard is shown in Figure 2.9(a-h).

Per-Band Validation

The validation results including R^2, RMSE, scatterplots with trend lines and 1:1 lines are provided in Figure 2.10(a-d). For each band, the vine values are clustered, whereas the spectral target points are scattered due to their distinctness. Overall, the red (Figure 2.10c) and NIR (Figure 2.10d) bands exhibited the highest validation R^2 values of

0.78 and 0.57 respectively. Viewing the distribution of all points around the 1:1 line is representative of the relationship between measured and estimated. The NIR band in particular appears more robust than the other bands due to the tight clustering around the provided 1:1 relationship line. The vine values for the red (Figure 2.10c) band however are variable, shown along the bottom of the graph increasing the RMSE value for this band. This over- and sometimes underestimation of reflectance was also observed in the other visible bands of blue (Figure 2.10a) and green (Figure 2.10b). The blue and green bands yielded R^2 values of 0.35 and 0.02 respectively. More importantly though, the green vine samples are clustered similarly to the red and are even more variable. Vine reflectance was overestimated by the green band more so than the red. Vine values for the blue band were often underestimated with values at, near, or less zero. Some values ended up slightly negative following conversion, leaving the remaining samples off the graph. The over- and underestimation of reflectance in the visible bands, particularly the blue and green bands, also occurred with the spectral targets (outliers shown in the upper-left and lower-right portions of Figures 2.10a and 2.10b).

Discussion

Validation Results

The estimated reflectance results were weaker than desired for the visible bands, particularly with blue and green, where blue resulted in extremely low values and green resulted in extremely high, variable values. Shorter wavelengths are typically more difficult to measure due to atmospheric scattering, which may have played a slight role. At such a low flying height though, these effects should have been minimal. Similar to the other visible bands, the modeled red band did not account for much of the variability

in the validation data. The red band, however, exhibited the best fit of the visible bands due to its accurate estimations of spectral target reflectance unlike the blue and green bands (see Figure 2.10a-d; spectral target reflectance values are found on or very near the fit line). The tendency of the visible band models to over- and underestimate brightness (DNs and subsequent reflectance) might be attributed to the CCD and Bayer filter's susceptibility to accentuate color as it is measured. Hunt et al. (2005) discussed similar findings where, in the majority of images captured, mean DNs of non-light (object) spectral targets were greater than values of 250. The sensors used in this study were designed for and marketed to a recreational audience that limits the amount of customization possible. Even using the custom settings outlined in the Materials and Methods section, digital cameras still automate much of the data collection process. The JPEG file format may have also contributed to this error even though similar studies insist otherwise (Lebourgeois et al. 2008).

In terms of future qualitative analyses, the produced orthophotos are highly accurate representations of the study vineyard that are very useful for surveillance mapping. As for quantitative analyses, the weak validation R^2 values for all bands does not support future work without a substantial amount of error. In cases where such error can be tolerated (which is very likely due to the vastly reduced cost of UAV-based image collection), the red and NIR bands could be employed due to their higher R^2 values. Of all bands, NIR appeared graphically (Figure 2.10d) to best estimate vine reflectance (clustered around the fit line) without the high variability that the visible bands exhibited (low RMSE). Similarly, Jensen et al. (2007) noted that digital camera-collected NIR information played the most significant role in predicting grain yields. Statistically

though, validation results for the red band accounted for the most variation in measured reflectance. Overall, poor results may relate to the general difficulty of establishing a statistical relationship between ground-measured spectra and aerial imagery due to spatial and spectral resolution differences between the spectroradiometer and the digital cameras. This difficulty was discussed by Lelong et al. (2008) and led to relative analyses (within each image set and not image set to image set) with DNs instead of conversion to reflectance. In addition, due to its very heterogeneous nature with leaves of varying angles and sizes, canopy gaps, trellis hardware (wire and posts), and other background noise/spectral contamination (bare soil and grass), vine canopy is a very difficult surface to model in terms of reflectance. Due to this, using vine canopy as a validation is an especially challenging endeavor. Additionally, unknown sensor capabilities, which were estimated in this study (wavelength intervals), might have contributed error.

Practicality of Provided Methodology and Future Work

The proposed data workflow provides a practical and very inexpensive means by which to collect very high spatial resolution orthophotos. Processing time and effort, though, remains lengthy, specifically the effort needed to mask the input images to generate high quality image products. Future research would benefit from increased automation within the proposed data workflow in an effort to reduce overall time needed to produce image products (spectrally-consistent or not). Also, in creating orthophotomosaics with and without image histogram equalization, it was found that image alignment was less successful with images that were adjusted, necessitating more manual effort to remove noise within the point clouds. This is due to the slightly adjusted

DNs that, when changed within all images, can reduce image-to-image matching. It would therefore be useful to create a methodology that could improve SfM results of spectrally-adjusted images. UAV image processing software is rapidly becoming more sophisticated though, which may soon provide the ability to match images and then adjust spectral properties within a single application.

Of the more successful bands of red and NIR, the NIR band was less likely to over- or underestimate spectral reflectance. This might be due to the ADC only being able to sense a narrow portion of the spectrum, which minimizes the degree to which the Bayer filter and CCD affect the DNs of the captured scene. In this way, future work may wish to use a spectral filter with the UDC (or ADC) to collect single bands within the visible range. For example, a green filter (blocking blue and red light) would force the sensor to collect less spectral information overall, which may increase accuracy of green information collected within three (RGB) bands. How the Bayer filter and CCD might record this spectral data is unknown. Future work may wish to create a time series of orthophotos to gain a fuller sense of the usefulness of digital camera-based spectral reflectance estimations.

In keeping with the practical nature of this research, band-to-band registration between cameras was not performed. Band-to-band registration between two cameras is impractical in many UAV applications because UAV (planes, quadcopters, blimps) payloads are extremely low (less than 400 g in many cases where one digital camera weighs around 150-200 g with batteries), therefore necessitating separate flights with each camera. Even if the UAV has the payload capacity to carry two cameras, further problems can arise: mounting the cameras very near each other proves difficult with

many do-it-yourself UAVs and capturing images simultaneously without a servo and the additional weight of the servo (with motor) further complicates system creation. If desired at a later time, bands can always be co-registered by way of resampling the rasters to a lower spatial resolution.

As for vineyard-specific future work, analysis of the generated image products is needed to further assess the usefulness of the data to viticulturists. Due to band-to-band registration being disregarded, future analysis with the red and NIR bands would likely need to take an object-oriented approach or resample the imagery to a coarser spatial resolution to properly register the bands to one another.

Conclusion

This study used two Canon PowerShot A480 digital cameras (UDC and ADC) to collect UAV aerial imagery within four spectral bands of blue, green, red, and NIR at a vineyard site in central Texas. A data workflow methodology was proposed to address radiometric and geometric corrections within the collected images, which using SfM image processing exports very high spatial resolution orthophotomosaics. The empirical line method was employed to transform DNs collected by the camera system to values of reflectance. Through a validation procedure it was found that the red and NIR bands were the most accurate at estimating reflectance (although with a significant amount of error), and therefore are better suited for future analyses. The blue and green bands were less accurate and were highly prone to over- and underestimate reflectance.

Table 2.1. Spectral calibration test results for UDC (visible bands).

UDC-Blue		
Interval (nm)	***Sample 1 (R^2; RMSE)***	***Sample 2 (R^2; RMSE)***
450	0.941; 8.028	0.925; 9.52
445-455	0.940; 8.083	0.927; 9.386
440-460	**0.937; 8.250**	**0.923; 9.628**
420-480	0.923; 9.111	0.906; 10.514
400-500	0.909; 9.436	0.894; 10.710
UDC-Green		
Interval (nm)	***Sample 1 (R^2; RMSE)***	***Sample 2 (R^2; RMSE)***
550	0.940; 9.730	0.958; 8.383
545-555	0.940; 9.691	0.958; 8.367
540-560	0.943; 9.482	0.959; 8.307
520-580	0.958; 7.986	0.963; 7.735
500-600	**0.973; 6.057**	**0.965; 7.242**
UDC-Red		
Interval (nm)	***Sample 1 (R^2; RMSE)***	***Sample 2 (R^2; RMSE)***
650	0.973; 6.683	0.963; 7.998
645-655	0.973; 6.681	0.963; 8.029
640-660	0.973; 6.710	0.961; 8.126
620-680	**0.974; 6.547**	**0.960; 8.189**
600-700	0.973; 6.478	0.958; 8.331

Table 2.2. Spectral calibration test results for ADC (NIR bands).

ADC-Blue		
Interval (nm)	***Sample 1 (R^2; RMSE)***	***Sample 2 (R^2; RMSE)***
840-860	0.939; 8.853	0.923; 10.010
820-880	0.937; 8.991	0.921; 10.125
800-900	0.933; 9.250	0.917; 10.344
ADC-Green		
Interval (nm)	***Sample 1 (R^2; RMSE)***	***Sample 2 (R^2; RMSE)***
840-860	0.988; 3.903	0.984; 4.526
820-880	0.988; 3.903	0.984; 4.526
800-900	**0.990; 3.587**	**0.986; 4.220**
ADC-Red		
Interval (nm)	***Sample 1 (R^2; RMSE)***	***Sample 2 (R^2; RMSE)***
840-860	0.946; 8.352	0.929; 9.600
820-880	0.946; 8.361	0.929; 9.600
800-900	0.945; 8.406	0.929; 9.625

Table 2.3. Derived reflectance conversion equations for each band.

Band	**Conversion Equation**	**R^2**	**RMSE**	**Spectral Targets Used**
Blue	Reflectance = (0.7076 * DN) - 71.149	0.999	2.753	White, Black, Red GCP
Green	Reflectance = (0.6016 * DN) - 48.385	0.982	10.158	White, Black, Red GCP
Red	Reflectance = (0.6162 * DN) - 55.824	0.991	6.631	White, Black, Blue
NIR	Reflectance = (0.5124 * DN) - 11.675	0.992	3.420	All

Figure 2.1. Sample images of spectral targets captured with the UDC (a) and the ADC (b) with the regions of interest (ROIs) shown (a) in different colors.

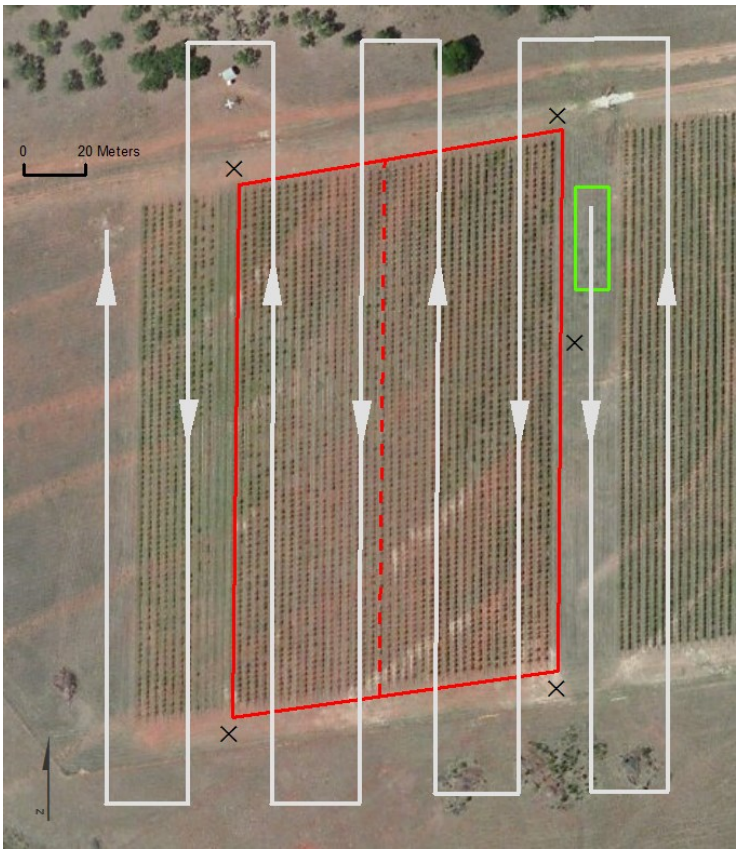

Figure 2.2. The study vineyard blocks with UAV flight path.

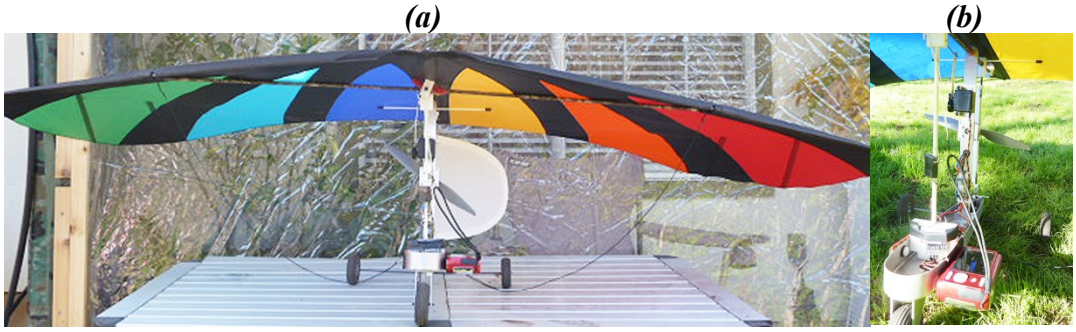

Figure 2.3. The kitewing UAV (a) with mounted digital camera (b) and other hardware.

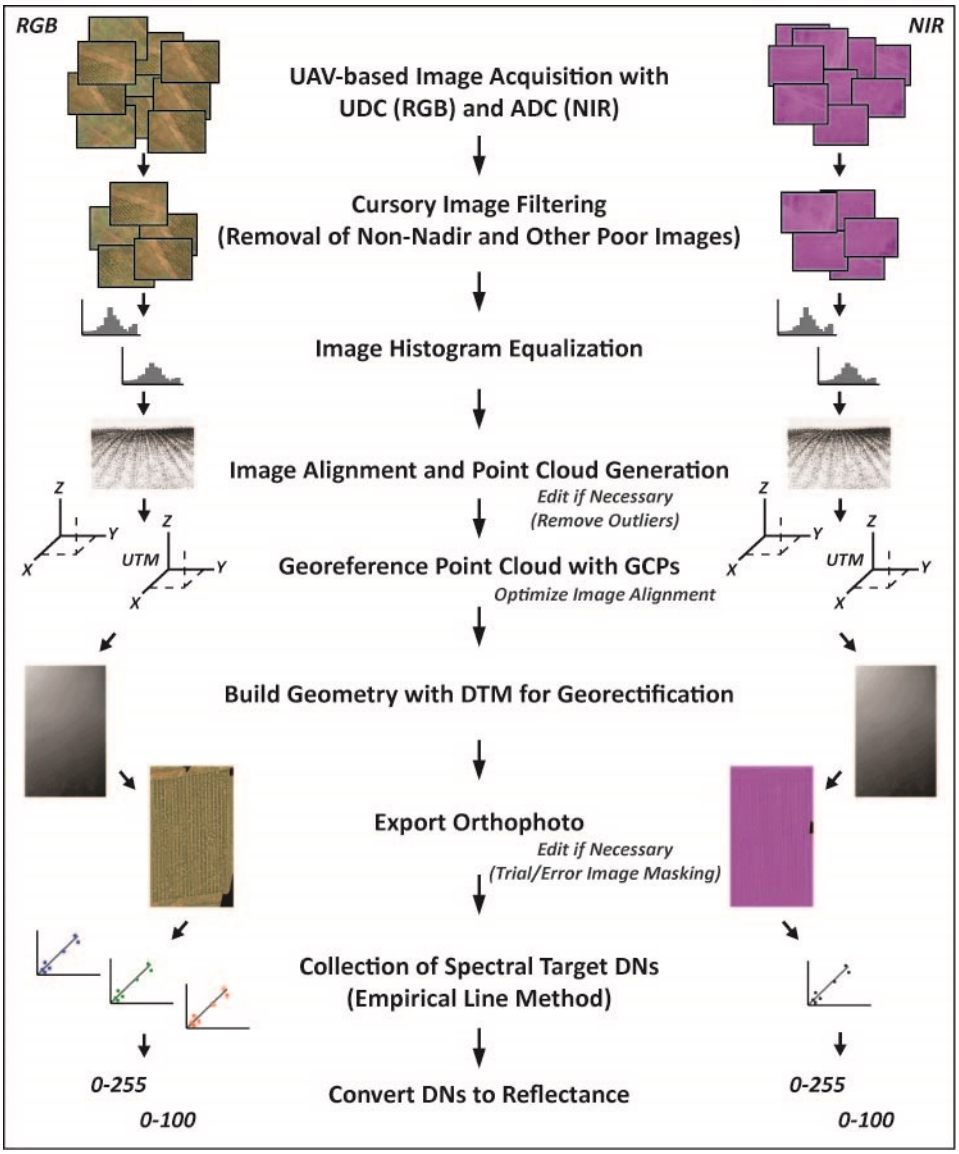

Figure 2.4. Data workflow from UAV image capture to final orthophoto generation.

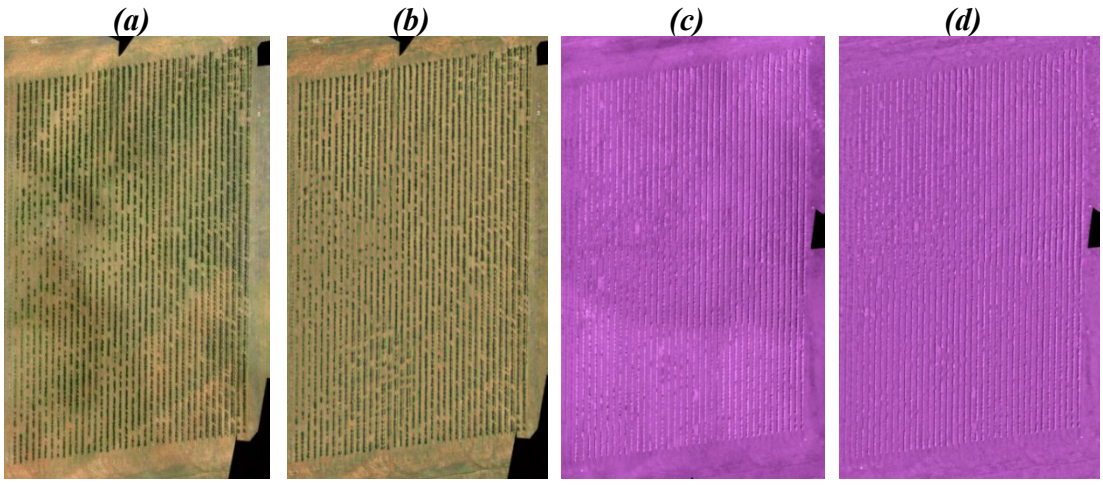

Figure 2.5. Comparison of image mosaics (RGB: a, b; NIR: c, d) with (b, d) and without (a, c) image histogram equalization.

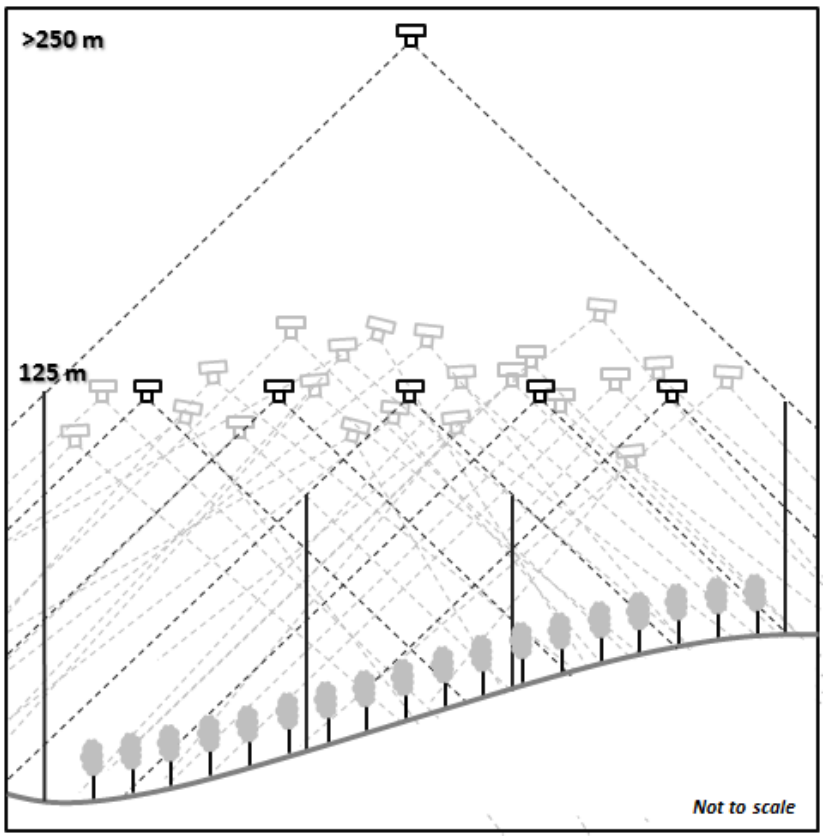

Figure 2.6. High- vs. low-altitude aerial image capture of vineyard canopy (ideal in black and realistic in gray).

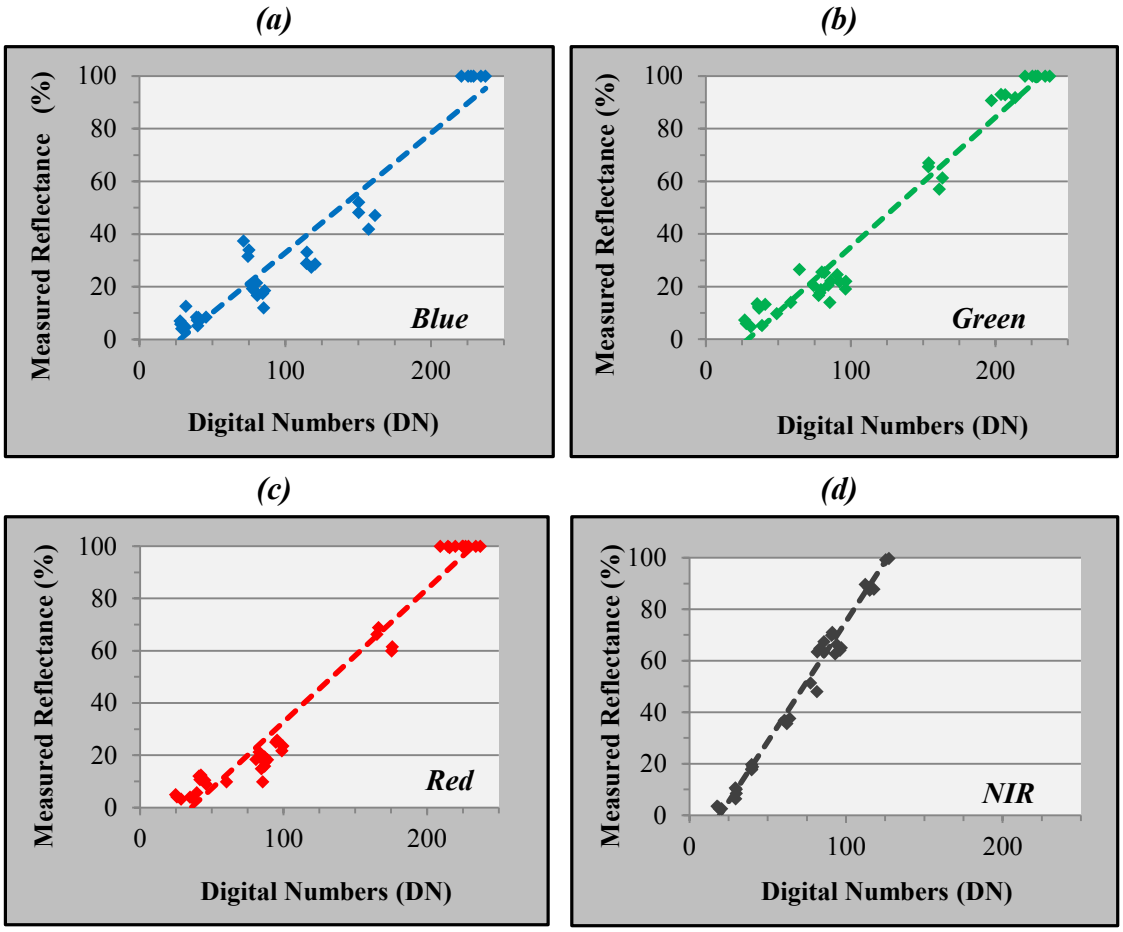

Figure 2.7. Relationships between spectroradiometer measured reflectance (Y-axis) and digital camera measured brightness (X-axis) of spectral targets within blue (a), green (b), red (c), and NIR (d) bands.

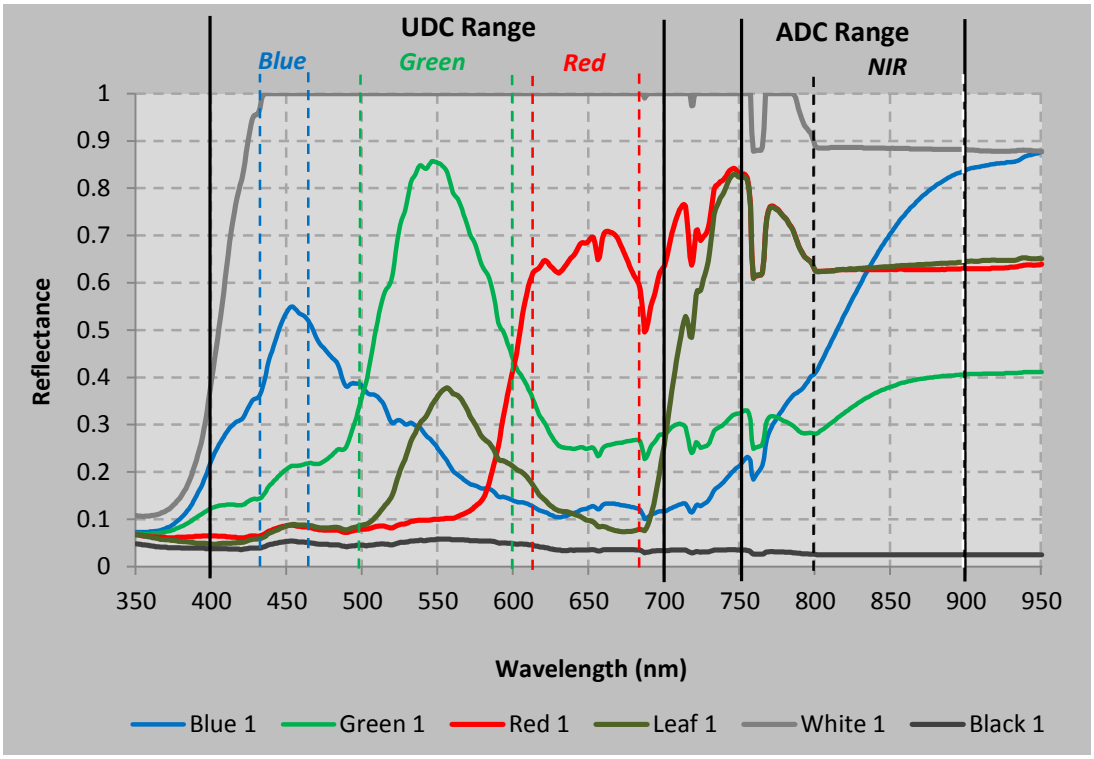

Figure 2.8. Spectral signatures of selected targets from sample 1 with camera spectral ranges and optimal band wavelength intervals.

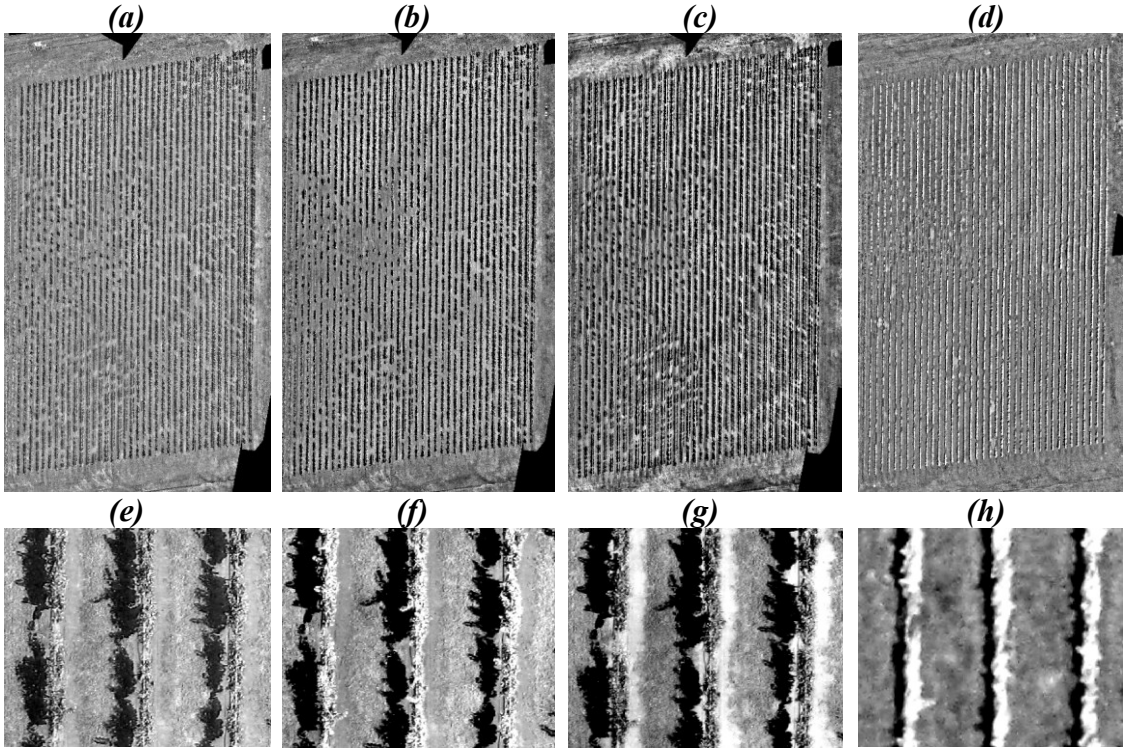

Figure 2.9. Generated orthophoto bands of blue (a,e), green (b,f), red (c,g), and NIR (d,h) at the whole-vineyard (a-d) and partial-vineyard (e-h) scales.

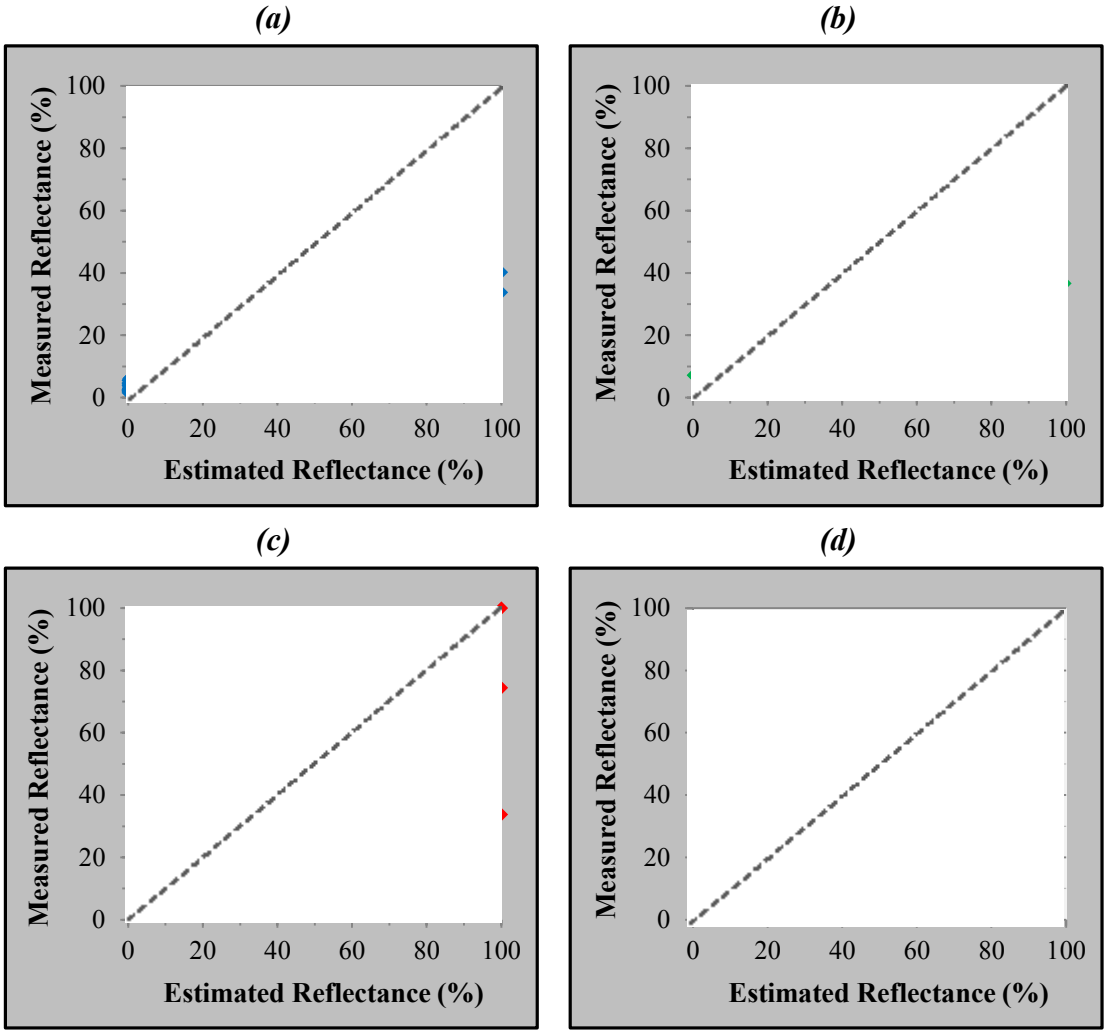

Figure 2.10. Validation results comparing measured (Y-axis) and estimated (X-axis) reflectance of vines and spectral targets within each band.

CHAPTER III

AN ANALYSIS OF VINEYARD CANOPY HEALTH THROUGHOUT A GROWING SEASON[2]

Introduction

Until recently, vineyard managers have had a limited ability to quickly and inexpensively map and monitor leaf area within their vineyards (Johnson et al. 2003b). Remotely sensed imagery and image processing techniques now provide such capabilities (Hall et al. 2002; Dobrowski et al. 2003). Aerial and/or satellite-based vineyard imaging and mapping, oftentimes using red and near-infrared (NIR) spectral bands to calculate the Normalized Difference Vegetation Index (NDVI; Rouse et al. 1973), has proven invaluable to viticulturists interested in evaluating spatial variation in canopy vigor and subsequent crop performance (Bramley et al. 2003; Hall et al. 2003). Identifying spatial variability of canopy vigor is particularly useful to vineyard managers who want to apply site-specific treatments to problem areas instead of implementing a uniform management practice throughout a vineyard. Equipped with the knowledge of differing areas of performance within the vineyard, viticulturists can implement separate management schemes (Proffitt et al. 2006), which can lead to the mitigation of the deleterious effect of within vineyard spatial variability of vineyard performance and/or selective or staged harvesting (Johnson et al. 2001; Bramley et al. 2003). Such adoption of precision viticulture, which is the optimization of vineyard performance by way of spatial data collection, analysis, and informed decision-making (Bramley and Proffitt 1999), has proven lucrative because it can help to reduce inputs (water usage, fertilizer, etc.) and

[2] Upon completion of this dissertation, this chapter was under peer review with *GIScience & Remote Sensing* with the title "Object-based spatiotemporal analysis of vine canopy vigor using an inexpensive UAV remote sensing system" (Submitted: Feb. 6, 2014).

increase crop value through better yield/quality attributes (Bramley et al. 2003; Proffitt et al. 2006).

Hall et al. (2011) described grapevine canopy vigor as being comprised of two main elements: (1) canopy area or size, and (2) canopy density. Canopy area is the extent of the canopy, which in remote sensing usually translates to planimetric area when vine and non-vine pixels are separated by way of NDVI thresholding (Hall and Louis, 2001) or object-based image segmentation (Smit et al. 2010; Hall and Wilson 2013). Canopy density relates to the thickness of the canopy, its structure, and overall photosynthetic capacity. NDVI has been used in several studies to provide quick and accurate estimates of vine canopy density (Hall et al. 2002; Johnson et al. 2003b; Hall et al. 2011). Other methods of gauging canopy density include destructive (plucking and measuring area of leaves) or non-destructive (using an electronic ceptometer, hemispherical photographs, or otherwise) estimation of leaf area index (LAI; proportion of one-sided leaf surface area to ground surface area). Ground-based LAI data collection though is time-consuming when compared to NDVI image analysis (Johnson 2003). The usefulness of assessing canopy vigor (area and density) relates to its relationship with eventual grapevine performance. Highly vigorous vines are likely to be higher yielding vines (Petrie et al. 2000; Hall et al. 2002; Proffitt et al. 2006), which has been confirmed with NDVI-based analyses (Hall 2003; Johnson et al. 2003b). Spatial variability in fruit quality attributes, such as color and phenolic content, which can influence final price paid for a crop, can be estimated similarly (Lamb et al. 2004).

Acquiring images for vineyard analysis requires spectral, radiometric, spatial, and temporal considerations (for a full review of these considerations see Hall et al. 2002). In

regards to timing of image acquisition, vineyard images are, at minimum, acquired during the veraison phenological phase of the crop cycle in which leaf surface area is at its maximum (Hall 2003; Proffitt et al. 2006). In addition, leaf area observed at veraison is most predictive of the eventual harvest that follows (Hall et al. 2011; Hall and Wilson 2013). This timing also provides vineyard managers enough time to make beneficial adjustments to the crop leading up to the harvest (Proffitt et al. 2006). For comparative studies within a single growing season or over a number of seasons, the post-budburst, post-flowering, harvest, and other inter-phases can also be imaged (Acevedo-Opazo et al. 2008; Hall et al. 2011). Imaging prior to flowering though (i.e. at budburst or post-budburst), can result in minimal spectral difference between grapevine canopy and inter-row space when a between row cover crop, which senesces later in the season, has similar spectral qualities (Hall et al. 2008). The timing of phenological phases and therefore the timing of image acquisition varies by the conditions of the particular growing season, the geographic location of the grapevines, and the specific cultivar being grown (Mullins et al. 1992; Creasy and Creasy 2009). Image acquisition at more than one stage of the growing season provides a comprehensive view of the spatial variation of vine canopy vigor over time (Hall et al. 2011).

In addition to temporal resolution of collected imagery, spatial considerations are also very important when studying vineyards because accurate assessment of vine canopy vigor can only be certain when whole pixels fit within the canopy (0.10-0.25 m; Hall et al. 2002). Very high spatial resolution imagery (0.25 m or less) provides the ability to explore canopy vigor at a per-vine scale (Hall and Louis 2008; Johnson et al. 2003a). This translates to every single vine within a vineyard being assessed and assigned a vigor

value. Based on these values, management zones can be created by grouping vines that are spatially clustered and have similar vigor values (Bramley et al. 2003). Zonal management can be implemented by treating these zones differently based on their specific vigor status (Johnson et al. 2001; Proffitt et al. 2006).

Recent advances in low-altitude, very high spatial resolution remote sensing can be attributed to increasing use of unmanned aerial vehicle (UAV) technology (Everaerts 2008), which has been adopted in viticultural research (Johnson et al. 2003a; Baluja et al. 2012; Primicerio et al. 2012; Bellvert et al. 2013; Mathews and Jensen 2013). UAVs, also referred to as unmanned aerial systems (UASs), equipped with a single (or multiple) sensor(s) serve as low-cost platforms for aerial image capture. UAVs provide additional flexibility due to greater ease in making repeat image acquisitions. Processing of UAV aerial imagery has benefitted from advances in computer vision, namely Structure from Motion (SfM; Snavely 2008; Snavely et al. 2008). Similar to traditional photogrammetric method, SfM inputs multiple overlapping UAV-captured images to recreate environments with three-dimensional point clouds similar to lidar datasets (Kaminsky et al. 2009; Fonstad et al. 2013; Mathews and Jensen 2013). Following conversion from arbitrary XYZ coordinates to projected geographic coordinates, SfM datasets have been employed in digital terrain modeling (Fonstad et al. 2013) and in turn used to generate high-quality orthophotomosiacs (Turner et al. 2012; Mathews 2014).

As for spectral resolution, most vineyard studies use NDVI to assess canopy vigor; requiring remote sensors to collect at least red and NIR bands (although blue and green are also usually collected). With UAV image collection where aircraft payloads are very low, sensors must remain lightweight. Digital cameras have been used

extensively for UAV image capture due to their durability, compactness, low-cost and lightweight nature (Lebourgeois et al. 2008; Ritchie et al. 2008). Other, more expensive sensors are prevalent in UAV image capture like the multispectral Tetracam (Turner et al. 2011; Kelcey and Lucieer 2012; Primicerio et al. 2012). Surprisingly though, NIR image capture is possible with a digital camera, although it must be altered to do so. The digital camera sensor, normally a charge-coupled device (CCD) or complementary metal oxide semiconductor (CMOS), typically has a spectral range of up to 900 nm (Cheng and Rahimzadeh 2005; Lelong et al. 2008; Ritchie et al. 2008). Ability to sense wavelengths to this extent, however, is limited by an internal hot mirror (spectral filter) that allows the CCD or CMOS to only sense wavelengths in the visible range (400-700 nm) for natural color photography. Following hot mirror removal, NIR band imagery can be collected from a UAV platform (Ritchie et al. 2008; Mathews 2014), adding significant value to images acquired for vegetation analysis.

The objective of this study was to observe spatial variability in vine canopy vigor (area and density) within a single growing season both practically and inexpensively using a UAV. Use of such low-cost equipment for image collection is contrary to many studies that employ specialized sensors and/or hire aircraft to capture aerial imagery. The intention with this approach was to make such an analysis easily replicable for researchers and practitioners alike. This paper sought to determine, with this UAV-collected imagery, optimal methods of data processing (incorporating object-based image segmentation) and analysis to identify differentials in canopy vigor. This includes exploring correlations between eventual vine performance (harvest variables including

number of clusters, cluster size, and yield) and estimated canopy vigor (area and density) as well as delineation of practical management zones for the vineyard manager.

Methods

Study Vineyard

This study focused on two contiguous vineyard blocks (see Figure 3.1) uniformly managed by a single winery located near Fredericksburg, Texas, USA. The study vineyard is located in the Texas Hill Country American Viticultural Area (AVA), one of the largest AVAs in the USA, covering an area of approximately 36,000 square kilometers in central Texas (west of Austin and north of San Antonio). The study vineyard blocks, separated with a dashed line in Figure 3.1, include a total of 38 rows of north-to-south oriented, drip-irrigated, vertical trellis-trained Tempranillo (Vitis vinifera) vines containing 65 to 95 vines per-row. The vineyard is situated on a slight incline with its highest point in the northwest corner and its lowest point in the southeast corner. The vineyard geometry is consistent with 2.75 m of spacing between vine rows (inter-row space) and 1.8 m between vines within rows. Vine canopy throughout the vineyard was minimally pruned, a pruning technique that enables a relatively large canopy area, appropriate to this particular cultivar and climate. In total, both study blocks cover an area of approximately 1.9 ha. These two contiguous blocks were chosen because they were the same varietal and managed together with the same uniform scheme. For this study, the two blocks were not delineated throughout because of this high degree of similarity and uniform management. Inclusion of both blocks and a larger vineyard area overall was preferred to include more variability to give more confidence in planned statistical analyses.

Data Collection

UAV Image Collection

All collected datasets were captured at the study vineyard during the 2012 growing season. Similar to Hall et al. (2008; 2011), vineyard images were acquired on three different dates during the grapevine phenological cycle: post-flowering (16-May), veraison (6-July), and harvest (1-August). For each acquisition date, images were captured under clear skies near solar noon to minimize the effect of shadowing between the vine rows (Johnson and Scholasch 2005; Zarco-Tejada et al. 2005). Images were captured using a Hawkeye UAV platform (www.ElectricFlights.com, Kingsland, TX, USA) and two digital cameras. The Hawkeye is a battery-powered (electric) kitewing plane with a single propeller and a payload of around 400 grams. The Hawkeye used in this study had autopilot functionality (Ardupilot; code.google.com/p/ardupilot/) that, when enabled automatically, navigated to pre-programmed waypoints (X,Y,Z) using an on-board GPS. The UAV was flown both manually and autonomously depending on wind conditions on the day of flight. In low winds (<20 kph), the autopilot was used exclusively (not including takeoff and landing). In high winds (>20 kph), the Hawkeye was susceptible to becoming stagnant when flying into the wind, which unnecessarily depleted battery power. In these cases, manual control was initiated to keep the UAV moving on its flight path. Flight paths were oriented north-to-south to fly into (south) and with (north) the wind for added stability. UAV takeoff and landing was always completed under manual remote control and occurred in the staging area near the northeast corner of the study vineyard (see the rectangular area highlighted in Figure 3.1).

During flight, the UAV was flown at a height of approximately 125 m above the ground surface.

Two Canon PowerShot A480 digital cameras (Canon U.S.A. Inc., Lake Success, NY, USA) with 10-megapixel resolution were used to capture blue, green, red, and NIR image bands. One camera was left unaltered (unaltered digital camera—UDC) and captured the three visible bands of blue, green and red (stored as RGB). Wavelength intervals of visible bands were not published by Canon and therefore were estimated by Mathews (2014) using spectroradiometer measurements and linear regression: 440-460 nm for blue, 500-600 nm for green, and 620-680 nm for red. The other camera was altered (altered digital camera—ADC) to capture NIR image data. NIR capability was enabled by removing the internal hot mirror and replacing it with clear glass (Cheng and Rahimzadeh 2005). An external NIR-only filter was placed over the ADC lens to restrict the ADC CCD to only sense NIR wavelengths from 750 nm to the extent of CCD spectral sensitivity at around 900 nm (Lelong et al. 2008). In the case of the ADC, three NIR bands were collected within this range. Both cameras, regardless of spectral range, stored images in JPEG format in three bands (RGB). JPEG format was preferred due its quick capturing nature and smaller file size (Levin et al. 2005). All images were captured with both digital cameras set to manual setting with sunlight white balance and no image adjustment (Levin et al. 2005; Ritchie et al. 2008). ISO levels were manually set to 80 for the UDC and increased to 400 for the ADC due to relatively lower radiance in NIR. ISO settings for both cameras were determined appropriate based on the speed of the UAV and ability of the digital cameras to capture sufficient light without image blur.

Cameras were mounted near the front of the UAV in a nadir-facing direction. Images were captured in-flight using the Canon Hackers Development Kit (CHDK; wikia.chdk.com) intervalometer script preinstalled on the SD cards of both cameras. The script automatically captured images every second during flight. Image capture was initiated manually just prior to UAV launch and continued until manual deactivation immediately following landing. Only one camera was mounted on the UAV at a time due to payload restrictions. Due to this, two flights were flown on each image acquisition date. For the first flight the UAV was launched, captured RGB images with the UDC for the entire 15 minute flight, and landed. Upon landing, the UDC was replaced with the ADC and the UAV lithium battery was also replaced. The UAV was then re-launched and began another 15 minute flight to capture NIR images. For more details on the methodology used to capture vineyard images, including more detailed UAV and digital camera specifications, see Mathews (2014).

Other Field Measurements

Other datasets collected on-site besides UAV images included GPS data, spectroradiometer measurements, and harvest variables of number of clusters, cluster size, and yield. Figure 3.2 shows the data collection effort in its entirety with the accompanying collection date. For each image date, both GPS and spectroradiometer data were collected. Spectroradiometer data were captured immediately following UAV-based image collection. Prior to image collection, several spectral targets were placed near the northeastern edge of the vineyard (within the UAV staging area—see Figure 3.1) to aid in transforming image digital numbers (DNs) to units of reflectance using the empirical line method. In total, six flat, colored (black, white, grey, blue, green, and red)

foamboard spectral targets sized 0.75 m by 0.5 m (placed in line, each about 2 m apart) were captured within UAV imagery. Spectroradiometer measurements of each of these targets were taken using a backpack-mounted ASD FieldSpec Pro (Analytical Spectral Devices, Inc., Boulder, CO, USA) with fiber optic cable and pistol-grip sensor. Measurements were captured by holding the sensor out away from the body and pointing it at the center of each target in a level, nadir direction about 0.7 m above the target. Measurements were taken standing on the far side of the target in relation to the sun to avoid casting a shadow onto the target (McCoy 2005). A minimum of two spectral readings were captured and averaged for each target to account for any variability in spectral response.

Ground control point (GCP) targets were placed in the field prior to capturing each image set. The GCP targets were made of sturdy foamboard, painted flat red with concentric white and black circles at the center, and sized 0.6 m by 0.6 m (similar to Aber et al. 2010). Five GCPs were placed around the vineyard to aid in georeferencing the captured images. Figure 3.1 denotes the locations of the GCP targets as X's. Each GCP location was logged using a Trimble GeoXH GPS with an external Zephyr antenna. For each location, 200 separate positions were averaged (X,Y: NAD83 UTM Zone 14N; and Z: NADV88). In all cases, GPS data collection was limited to a maximum position dilution of precision (PDOP) of three. Following the collection of GPS data, differential correction was performed using the Trimble GPS Analyst Extension in ArcGIS (ESRI, Redlands, CA, USA).

The remaining data were collected around the time of the harvest. These per-vine performance variables include the number of clusters, cluster size, and yield (kg). All

three of these variables were collected using the same stratified sampling procedure resulting in the same vines being sampled. The sample consisted of every fifth vine row, alternating the starting vine within each sampled row and sampling every tenth vine within rows (i.e. row 1-vine 1, row 1-vine 10, etc.; row 5-vine 5; row 5-vine 15; etc.). Additional samples were taken for rows 1, 10, 20, and 30 for vines 11, 21, 31, etc. to add more samples to the dataset and to include several adjacent sample vines. This adjacency was considered important due to the use of very high spatial resolution imagery where vines were easily recognizable from one another. Row numbering began from the easternmost row, while vine numbering began with the northernmost vine in each row. Sampling ended with vine row 35. The vine trunks of the sampled vines were GPS-located using the previously discussed GPS unit and processing with the exception that the number of averaged positions was reduced to 30 from 200. The sampled vines are shown in Figure 3.1 as black dots. All of these locations represent vines sampled for number of clusters and cluster size; whereas those with a white outline are those that were also sampled for yield (fewer total vines were available to be sampled at harvest).

The number of clusters and cluster size for each sampled vine was logged on the harvest image date (1 August) following spectroradiometer and GPS data collection. In total, 97 vines were sampled for these two variables. For each vine, the number of clusters was counted by hand and recorded. Following cluster count, an ordinal assessment of cluster size was recorded for each vine. A single value (small, medium, or large) denoting cluster size was recorded for each vine based on a broad assessment of the size of all the clusters produced by a particular vine. Consistency was maintained by repeatedly using an object for size comparison (a digital camera). On-ground

photographs of sampled vines were also collected to confirm recorded cluster sizes upon returning from the field. Yield per vine (in kilograms) was measured on location the morning of harvest (6 August). Harvest occurred five days after the harvest image acquisition date. For each sample vine, clusters were removed, placed in a container, and weighed (subtracting the known container weight). In total, yield data for 42 vines were recorded.

Data Processing

Following data collection at post-flowering, veraison, and harvest, data were processed following the workflow provided in Figure 3.2. For each image acquisition (post-flowering, veraison, and harvest), vineyard orthophotos were produced using the methodology outlined in Mathews (2014). This procedure accounted for radiometric and geometric errors within the collected UAV images and output single, corrected orthophotomosaics covering the entire study site (six in total). A cursory manual filtering of each set of images (RGB and NIR sets for each date) was necessary to remove non-nadir viewing images and any blurry images based on UAV movement (see Table 3.1 for image counts). Treating each narrowed set of images separately, image histogram equalization was applied to account for any brightness discrepancies from image-to-image using the ERDAS ImageEqualizer (Intergraph Corp., Madison, AL, USA). Each image set was then processed and aligned with SfM algorithms provided by Agisoft PhotoScan (Agisoft LLC, St. Petersburg, Russia). With each image set, PhotoScan automatically overlapped images and built three-dimensional point cloud models. GCPs were manually identified within images in PhotoScan and given their GPS measured coordinates. PhotoScan then automatically transformed the point cloud model from

arbitrary three-dimensional space to known geographic coordinates. The georeferenced point clouds provided a site-specific digital terrain model (DTM) for each image set for proper geometric correction. Orthophotos were then created by mosaicking images following a manual masking process to ensure full vineyard coverage, confirm planimetric accuracy by excluding areas of distortion within images, and remove any remaining vignetting around image corners (Mathews 2014).

Due to separate flights being undertaken for the UDC and ADC, simple band-to-band registration of visible and NIR imagery, where the spectral integrity of the originally obtained individual pixels is preserved, was not possible. This was avoided to keep intact the very high spatial resolution desired with the UAV-based methodology. Therefore, UDC (RGB) and ADC (NIR) images throughout this study were treated and processed separately. Simple NDVI images (overlapped pixels) could not be calculated. NDVI values were calculated based on extracting median red and NIR values from whole vine objects (discussed further in paragraphs that follow).

Spatial resolution was known following export of each orthophoto. On average, the spatial resolution of all orthophotos was 25 mm. Specific orthophotos yielded differing spatial resolutions as provided in Table 3.1 based on variation in flying height. The number of images collected per-flight (all images) is shown in Table 3.1 as well as the number of high quality nadir images, and number of images used to export the orthophoto (images used). High variability in the amount of images collected and used relates to flying conditions on the acquisition date where high winds resulted in less flying time and less images overall as well as less high quality nadir images due to UAV instability.

Pixel values for each orthophoto were transformed from DNs (0-255) to units of reflectance (0-100) using the empirical line method (Smith and Milton 1999). DNs of spectral target pixels (mean values of central pixels to avoid adjacency effects after Levin et al. 2005) were collected and compared to field measured reflectance. For each band of all orthophotos, linear regression was used to create predictive equations (see Table 3.1) to change DNs to reflectance values. Orthophotos in units of reflectance (0-100) were created using the raster calculator in ArcGIS. In assessing the radiometric quality of the produced blue and green bands for post-flowering, Mathews (2014) determined these bands were unfit for further quantitative analysis due to excessive over- and under-estimation of brightness. This was due to a poor relationship between field measured reflectance and estimated (empirical line method) orthophoto reflectance. This is evident in Table 3.1 where conversion R^2 values for these bands are lower than the red and NIR bands, and RMSE values are higher. Mathews (2014) also reported that of the three collected NIR bands, the ADC-Green band (NIR) best correlated with spectroradiometer measurements. Due to this, the ADC-Blue and ADC-Red bands were dropped from further analysis (not shown in Table 3.1). The UDC-Red (red) and ADC-Green (NIR) bands were utilized to calculate NDVI.

After production of orthophotos (following Figure 3.2), image segmentation was performed using the open source software Monteverdi 2 (Orfeo Toolbox—OTB, French Centre National d'Études Spatiales, Paris, France). The mean-shift image segmentation algorithm was used for each orthophoto using the same parameters: a spatial radius of 5 (pixels) and a range radius of 10 (pixel values). Three-band RGB and single-band NIR orthophotos were input for post-flowering, veraison, and harvest. Three-bands (RGB)

were included in segmentation to provide additional spectral information to aid the algorithm in identifying and separating segments. Segmentation results were exported to vector format. As Figure 3.2 shows, vine-only segments were then selected to create vine canopy-only polygons. This was completed by spatially selecting vine canopy segments using known vineyard geometry, specifically vine rows that intersect canopy segments. Vine locations and vineyard geometry were estimated based on the GPS-collected sample vine locations and using the known ground distance between vines and vine rows. In this way, all vine locations throughout the vineyard were established in ArcGIS. Vine row vector files were created from vine locations. Following selection of vine-only segments, further manual touch-ups were performed to remove obvious non-vine segments. The vine-only segments were dissolved to create single polygons representing vine canopy. An image segmentation example for a portion of the vineyard is shown with Figure 3.3.

The output image segments (grey, solid lines in Figure 3.3) contain vine canopy as well as other features, including shadows and bare soil along the vine row. The vine canopy-only segments are outlined with a thick solid black line. These were split for each vine using extraction zones similar to Hall et al. (2011). Vine trunk locations are shown as well as extraction zones (1.8 m by 1.8 m dashed squares around the vine trunks). Extraction zones were used to cut the vine canopy polygons into per-vine pieces or objects. These per-vine objects were then used to calculate area and extract spectral data for each vine. Extraction zone sizes were based on the known vine-to-vine distance and field observation (no vine canopy came close to exceeding the extent of the 1.8 m allotted extraction width).

Per-vine objects (polygons) were attributed to every vine within the vineyard. Canopy area in square meters was calculated for all vines six times total (twice, RGB and NIR, for each phenological phase). Mean canopy areas were also calculated for each phenological phase (mean of RGB and NIR canopy area) and for the entire season (mean of all canopy areas). GRASS GIS 6.4.3 (grass.osgeo.org) was used, specifically the v.rast.stats function, to collect spectral statistics and attach spectral values to each vine (see Figure 3.2). This tool examined all pixels within each per-vine object and calculated mean and median values of red and NIR reflectance. After examination of extracted spectral values, median values were deemed more representative of per-vine objects than mean values due to some per-vine objects including outlier values (extremely high or low reflectances due to inclusion of soil or shadow within canopy segments). Due to this, median spectral values were used throughout the study. NDVI was calculated for all vines using median reflectance values as shown in Equation 3.1.

$$NDVI_{median} = (NIR_{median} - Red_{median}) / (NIR_{median} + Red_{median}) \quad (3.1)$$

Data Analysis

Two end products were created to explore spatial variation in canopy vigor (both for planimetrically-based canopy area and spectrally-based canopy density): maps and correlation coefficients between canopy vigor and harvest variables. Using every vine location with planimetric area and NDVI values (3436 total vines), ordinary kriging was implemented to create surface maps of canopy vigor—area and density respectively (Proffitt et al. 2006). These were created for each of the phenological stages as well as for the entire season based on a mean value of all three stages.

Correlation analysis was performed to compare canopy area and canopy density values to field-measured harvest variables. Correlations were calculated for each of the phenological stages as well as for the season average. Further, for each phenological stage, separate values were explored (i.e. post-flowering RGB canopy area, NIR-canopy area, and average canopy area; harvest red reflectance, harvest NIR reflectance, harvest NDVI; etc.) to identify the variables that most highly correlate with harvest variables. Pearson's correlation coefficients were calculated for all variables except for cluster size, which was at the ordinal scale. In these instances, the Spearman's rank correlation coefficient was reported.

A vine performance index (VPI) was calculated based on the canopy vigor variables that exhibited the highest correlation coefficients when compared to number of clusters, cluster size, and yield. Since average canopy area and average NIR_{median} were most correlated with these harvest variables, the VPI was calculated as a product of the two (Equation 3.2). A VPI value was calculated for all vine locations within the study vineyard except for those known to not have vines (dead/missing plants) based on not having per-vine object polygons. The VPI results were presented with a per-vine map to explore spatial variation in vine performance for the entire 2012 growing season.

$$VPI = \text{Season Average Canopy Area (sq m)} * \text{Season Average } NIR_{median} \quad (3.2)$$

Using VPI values, similar vines were grouped to create management zones for future growing seasons since the underlying physical/environmental properties that cause patterns of spatial variation in performance remain consistent from season-to-season (Bramley and Hamilton 2004). The grouping analysis function was used in ArcGIS to cluster all vines into 25 groups, which was then manually collapsed into 11 zones. The

grouping analysis spatial statistic utilized each vine's VPI value and spatial location (k nearest neighbors where k is a specified number of neighbors to be evaluated; k = 5) to analyze spatial patterns and output groups of similar performance. The exported groups were visually assessed and used to manually digitize management zone polygons. The grouping results were not used directly because the grouping analysis did not account for practicality of adoption of the groups or management zones. Following this logic, vines were grouped to take advantage of existing vineyard geometry where substantial portions of rows were assigned the same zones rather than having one or two vines within a row grouped with different zones.

Results

Canopy Area

Canopy area maps as estimated from planimetric extent are provided in Figure 3.4. These maps represent the average canopy area (RGB and NIR) for each of the phenological periods (Figure 3.4a-c) as well as the season average (Figured 3.4d). The spatial pattern of canopy area remains consistent over the growing season with smaller extent canopies located in the central-west portion of the vineyard. Vine canopies of greater extents are consistently located in the northern and eastern areas of the vineyard. In general, the post-flowering phenological phase exhibited the greatest overall canopy density, especially in the dense areas already mentioned. As the season progressed following post-flowering, canopy extent for the most part either remained the same size or shrank.

Correlation results for canopy area and harvest variables are provided in Table 3.2. Correlations are provided for each phenological phase within which RGB-based,

NIR-based, and average canopy areas are shown. The highest correlation coefficients within each part of the table are highlighted with bold type, the highest correlation coefficient of the three phenological phases is underlined, and the highest correlation coefficient overall is highlighted in gray. All correlation coefficients for canopy area and harvest variables were statistically significant ($p <= 0.01$). For the relationships between number of clusters per vine and canopy area, mean canopy area demonstrated the strongest correlations for all phenological periods. Within the growing season, mean canopy area for post-flowering most strongly correlated with number of clusters (0.492), although harvest canopy area was very similar (0.488). In this case, veraison canopy area was the least correlated with number of clusters produced per-vine. The season average yielded the highest correlation coefficient at 0.560.

The Spearman's rank results for cluster size yielded similar findings where mean planimetric area was most highly correlated with cluster size for two out of the three periods (post-flowering: 0.432 and harvest: 0.497). For this variable though, harvest yielded the highest correlation coefficient instead of post-flowering. The season average correlation coefficient remained the highest overall at 0.516.

As for yield, yet again mean planimetric area was consistently highly correlated with yield when compared to the RGB- and NIR-based canopy areas. For yield though, unlike number of clusters and cluster size, planimetric area from the veraison phenological phase of the growing season resulted in the highest correlation coefficient (0.577). The season average resulted in the highest correlation coefficient overall at 0.654.

Canopy Density

Unlike the canopy area maps provided in Figure 3.4(a-c), the canopy density (NDVI-based) maps provided in Figure 3.5(a-c) were not spatially consistent over time. The central-west area noted previously for having consistently small planimetric canopy area had a low canopy density at post-flowering, a mixed density at veraison, and a high density at harvest. Although such as scenario is possible (Hall et al., 2011), in this case it seems unlikely because it is not occurring in predictable areas within the vineyard. Similarly, in other areas of the vineyard, spatial patterns are inconclusive.

The canopy density correlation results are provided in Table 3.2. The inconsistent NDVI-based canopy density results shown in Figure 3.5(a-d) are confirmed by weak correlation coefficients between NDVI and all harvest variables. The only phenological stage in which a statistically significant correlation coefficient was produced with or from NDVI was for the harvest stage and cluster size (0.273). Due to the weak results of the NDVI, single-band correlations are also provided for the red and NIR bands. High, positive correlations would be expected for NIR (high reflectance, low absorption), while high, negative correlations would be expected for red (low reflectance, high absorption). Red reflectance though, in all cases has little to no relationship with the three harvest variables (no statistically significant correlations). NIR correlations, on the other hand, with the exception of the correlation between veraison and cluster size, are statistically significant and have moderate, positive relationships. Looking at the NIR relationships, harvest NIR consistently exhibited the highest correlations with all harvest variables compared to post-flowering and veraison. Season average NIR correlation coefficients were higher than harvest with number of clusters (0.509) and yield (0.634).

Vine Performance Index and Management Zone Delineation

Based on the correlation analysis, the season average canopy area and season average NIR_{median} reflectance were used to calculate the vine performance index. These two variables had the highest correlation coefficients when compared to eventual crop performance (harvest variables). The vine performance index equation was provided previously with Equation 3.2. This index simply multiplies canopy area values (extent in square meters) by canopy density values (albeit only NIR reflectance) resulting in high values for vines with high vigor and low values for vines with low vigor. Correlation evaluation between the VPI and the harvest variables confirmed statistically significant, higher correlation coefficients (VPI, number of clusters: 0.585; VPI, cluster size: 0.505; VPI, yield: 0.685).

Figure 3.6a displays the spatial distribution of vines with their calculated VPI values (high values are dark; low values are light). The central-west portion of the vineyard was clearly the area of lowest vigor within the study vineyard with a number of missing/removed vines and vines with very low VPI values. High vigor areas are found towards the northern end of the study vineyard as well as along the eastern edge. Medium-to-low vigor areas were present in the southeast and southwest corners of the vineyard.

The automatic grouping analysis results are provided in Figure 3.6b. These groups of vines were placed together based on spatial location and VPI value. The proposed management zones are overlaid (black outline) on the grouping results (Figure 3.6b) as well as provided in a separate figure (3.6c). The proposed management zones were created based on the grouping results (Figure 3.6b), existing vineyard geometry, and

ease of adoption. The proposed management zones (Figure 3.6c) are numbered 1-6 with 1 being the highest vigor zone and 6 being the lowest.

Discussion

Assessment of Methodology and Results

The proposed methodology provided a very low-cost means by which to collect remotely sensed images of vineyards and was successful in identifying spatial variation in vine canopy vigor, especially canopy area. Planimetric canopy area was comprehensively successful in retrieving significant, moderate, positive correlative relationships with harvest variables similar to Hall et al. (2011). As for the spectrally-based canopy density figures, estimation of canopy density by way of NDVI remained difficult due to the use of a simple, off-the-shelf UDC to collect the visible bands. Much of the error observed with the red band reflectance related to the likelihood of the UDC CCD (and the internal Bayer filter) to emphasize color as it was measured. This resulted in inconsistent, under- and, for the most part, overestimations of brightness in the red and other visible wavelengths that while appropriate for recreational image capture, is not desirable for quantitative remote sensing. For further discussion on the error associated with UDC-collected visible bands see Mathews (2014).

Using digital cameras for UAV research relates to the very low payload of UAVs. Fortunately for future studies, sensors created specifically for UAV remote sensing are rapidly being developed and will likely become increasingly affordable. Many studies have utilized the Tetracam multispectral UAV sensor with success (Turner et al. 2011; Kelcey and Lucieer, 2012; Primicerio et al., 2012), but currently this sensor remains cost prohibitive for most practitioners without substantial technology budgets. Without

changing the sensors employed in this study, Mathews (2014) suggested attempting to record specific bands of visible information, like the red band, with a red-only spectral filter forcing the digital camera to collect a smaller range of wavelengths similar to how the NIR image data, which proved more useful, was collected. Whether or not such a method will improve collected visible reflectance is unknown.

Based on the results of this study, which had success using planimetric extent for canopy area and NIR_{median} reflectance for canopy density, the imagery collected at harvest produced the highest correlation coefficients of all phenological stages when related to the harvest variables collected. Therefore, if only one image acquisition were possible in future growing seasons with this system and methodology, harvest would be the best time to capture image data. In cases where multiple acquisitions are possible, collection of data throughout the growing season and calculation of mean values of all image periods resulted in even higher correlation coefficients for canopy area and NIR_{median} reflectance when related to eventual crop performance. Based on these results, collection of multiple image sets is preferred to single stage image capture because it provides a fuller picture of vine canopy vigor over an entire growing season.

Image segmentation provided a relatively quick and standardized method to create per-vine objects for each phenological stage to calculate canopy area and extract spectral information from collected imagery. Implementation of image segmentation algorithms into image processing workflows in this and other very high spatial resolution vineyard studies (Smit et al. 2010; Hall and Wilson 2013) has proven very useful at extracting per-vine canopy information.

The proposed VPI is simple to calculate and successful in displaying spatial variation in vigor across vineyards. The VPI worked well for the datasets collected in this study due to the success of image segmentation and the radiometric accuracy of the ADC collecting the NIR imagery. Incorporation of the season average NIR_{median} in the VPI was based on the high correlation coefficients NIR shared with harvest variables. Although this study was unable to do so, integration of red reflectance would provide a more complete picture of the photosynthetic ability of each vine than would NIR_{median} alone. Using VPI values for all vines, the grouping analysis was advantageous in creating preliminary groupings that provided visual aids for manual delineation of management zones. This type of analysis is quick to process and provides an automated, objective option to generate preliminarily management groups. Using these groups made manual delineation of the final management zones much easier and less time-consuming.

Future Work

Instead of exclusively relying on collected spectral information that in this study proved unsuccessful overall, another UAV and digital camera-based method may exist to estimate vine canopy density, more specifically canopy structure. Mathews and Jensen (2013), for example, estimated LAI for vines with moderate success based on SfM point clouds created from UAV-captured RGB images. High quality, dense SfM point clouds of vineyards might also be used to begin to estimate vertical canopy extent in addition to planimetric extent. Such analysis could yield values of vine canopy volume that may correlate highly with eventual yield and other harvest variables.

Similar future studies may wish to capture imagery over several seasons to explore season-to-season trends in canopy vigor and harvest variables (similar to Hall et

al. 2011). Such research could clarify the best phenological timing for image capture for this or a similar UAV system. Future studies may wish to further pursue other useful metrics in regards to image segmentation results. This may include creating temporal visualizations to view canopy vigor (area and/or density) change over a season and/or calculating per-vine change metrics to relate to vine performance variables. Also, future work may wish to explore the full potential of the very high spatial resolution afforded by this UAV such as adapted/improved segmentation algorithms for vineyard UAV remote sensing and extraction of information from within per-vine canopy objects (i.e. identification of high and low vigor areas within single vine canopies). Future studies may also wish to customize the grouping analysis utilized in this study to automate the entire management zone delineation process by accounting for vineyard geometry and automatically outputting practical, ready-for-adoption zones.

Conclusion

The UAV and digital camera system employed in this study was successful at identifying spatial variability in vine canopy vigor, specifically planimetrically-derived canopy area, at a study vineyard in the Texas Hill Country AVA during the 2012 growing season. The UAV and digital cameras utilized, data collection methods, and data workflow provided a very inexpensive approach to survey vineyards with very high spatial resolution orthophotos (25 mm on average). Spectral performance of the digital cameras was not adequate to calculate useful values of NDVI for canopy density estimation. Only NIR reflectance correlated with harvest variables as expected. A vine performance index was calculated that provided per-vine estimates of vigor for the entire

study vineyard. Management zones for future seasons were successfully delineated based on grouping analysis of vines of similar vigor and spatial location.

Table 3.1. UAV-collected images, conversion results, and output orthophoto attributes.

Acquisition Date	Bands	All Images	Nadir Images	Images Used	Spatial Resolution	Conversion Equation	R^2 (RMSE)
16 May *Post-flowering*	Blue	150	59	25	26 mm	(0.7076 * DN) - 71.149	0.999 (2.753)
	Green					(0.6016 * DN) - 48.385	0.982 (10.158)
	Red					(0.6162 * DN) - 55.824	0.991 (6.631)
	NIR	191	45	13	35 mm	(0.5124 * DN) - 11.675	0.992 (3.420)
6 July *Veraison*	Blue	268	96	57	21 mm	(0.4835 * DN) - 25.615	0.778 (18.519)
	Green					(0.4465 * DN) - 11.218	0.853 (15.418)
	Red					(0.4417 * DN) - 18.794	0.923 (11.018)
	NIR	96	36	26	25 mm	(0.5122 * DN) + 2.8008	0.988 (3.791)
1 August *Harvest*	Blue	241	81	45	20 mm	(0.5239 * DN) - 37.712	0.884 (13.400)
	Green					(0.4394 * DN) - 17.472	0.844 (15.865)
	Red					(0.3481 * DN) - 15.105	0.984 (4.313)
	NIR	248	77	59	22 mm	(0.5193 * DN) - 5.347	0.994 (2.739)

Table 3.2. Canopy area correlations.

			Canopy Area (Planimetrically-based)			
			Post-Flowering	***Veraison***	***Harvest***	***Season Average***
Harvest Variables	***Number of Clusters***^	*RGB*	0.404	**0.438**	0.392	0.515
		NIR	0.425	0.344	0.370	0.479
		Mean	**0.492**	**0.438**	**0.488**	**0.560**
	Cluster Size†	*RGB*	0.357	**0.375**	0.408	0.461
		NIR	0.380	0.284	0.371	0.409
		Mean	**0.432**	0.363	**0.497**	**0.516**
	Yield (kg)^	*RGB*	0.445	0.538	0.374	0.606
		NIR	0.485	0.516	0.457	0.616
		Mean	**0.528**	**0.577**	**0.510**	**0.654**

^Pearson Correlation Coefficient; †Spearman's Rank Correlation Coefficient; All correlations significant to the .01 level; Note: Areas were calculated in square meters.

Table 3.3. Canopy density correlations.

			Canopy Density (Spectrally-based)			
			Post-Flowering	***Veraison***	***Harvest***	***Season Average***
Harvest Variables	***Number of Clusters^***	*Red*	0.080	0.154	0.021	0.132
		NIR	**0.430****	**0.217***	**0.440****	**0.509****
		NDVI	-.028	-0.112	0.068	-0.002
	Cluster Size†	*Red*	-0.060	-0.002	-0.194	-0.083
		NIR	**0.326****	0.136	**0.441****	**0.409****
		ND VI	0.101	-0.029	0.273**	0.202*
	Yield (kg)^	*Red*	0.095	0.137	0.148	0.198
		NIR	**0.366***	**0.432****	**0.613****	**0.634****
		ND VI	-0.014	-0.004	-0.003	-0.071

*^Pearson Correlation Coefficient; †Spearman's Rank Correlation Coefficient; *Correlation significant to .05 level; **Correlation significant to .01 level; Note: All spectral values extracted from vine objects are medians.*

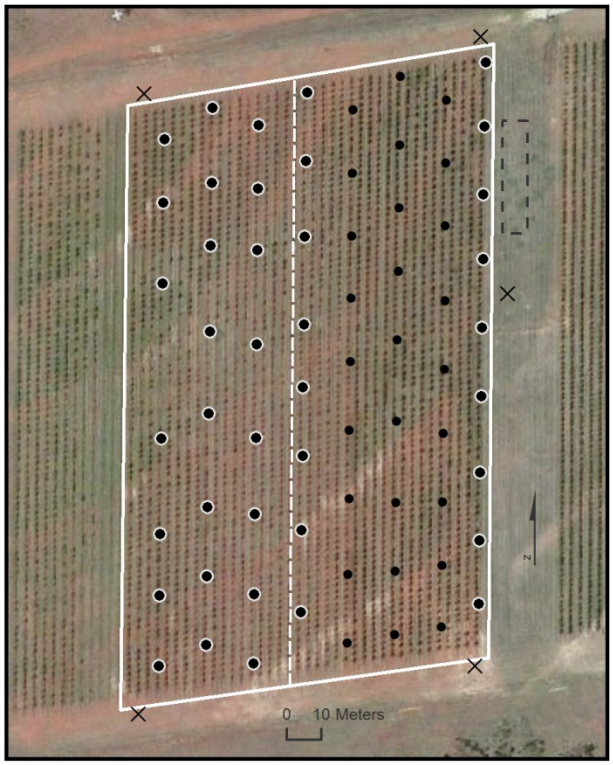

Figure 3.1. The study vineyard in the Texas Hill Country AVA.

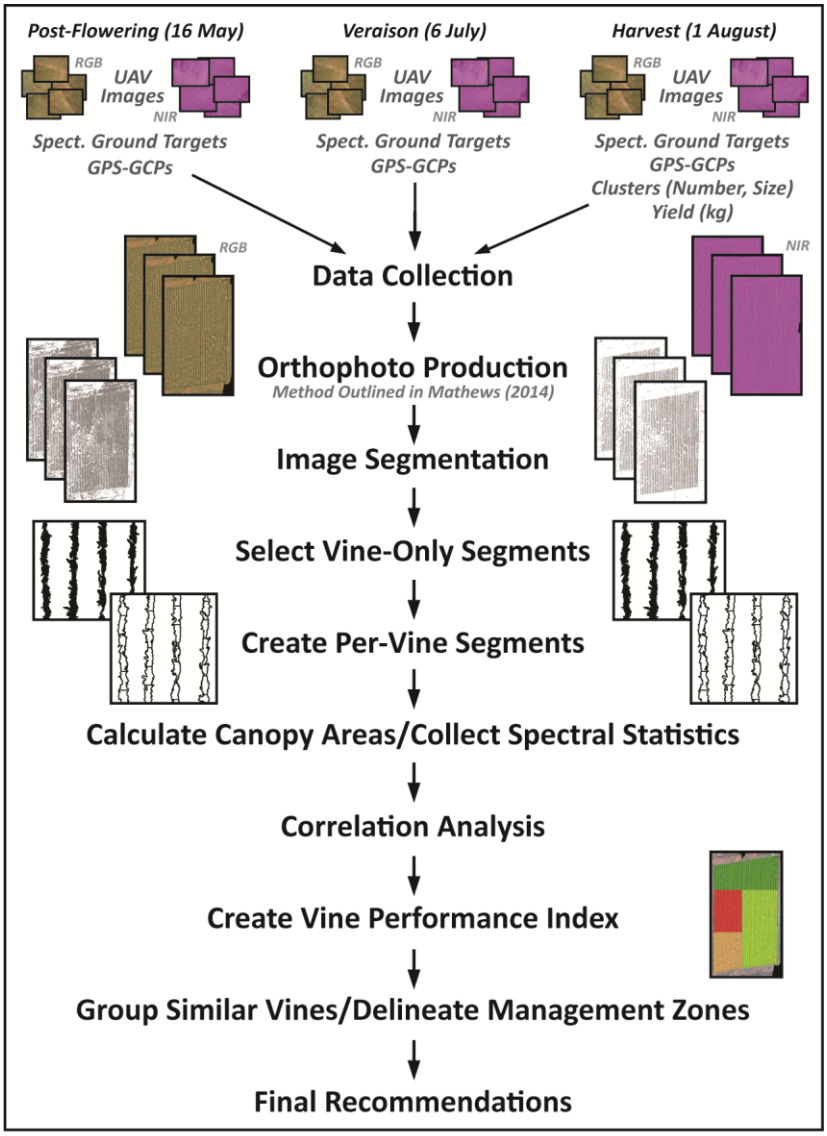

Figure 3.2. Data workflow from collection through processing and final analysis.

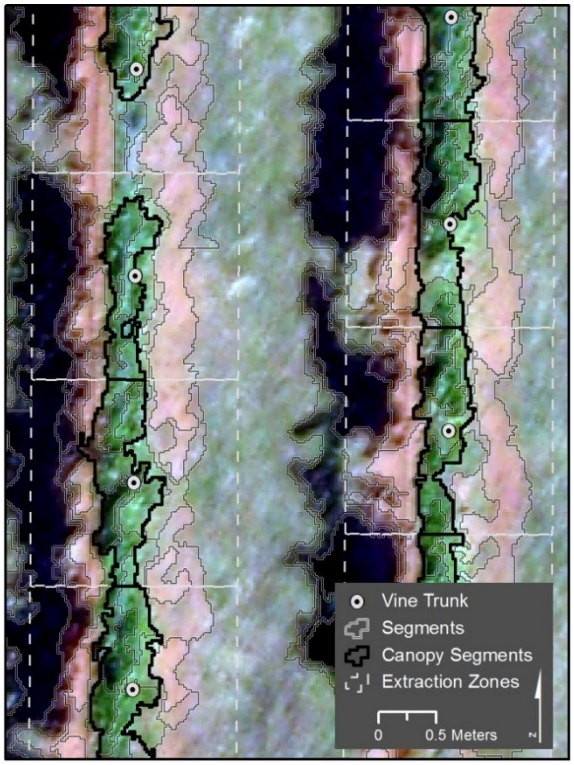

Figure 3.3. Image segmentation results and extraction zones for select vine canopies for the veraison RGB orthophoto.

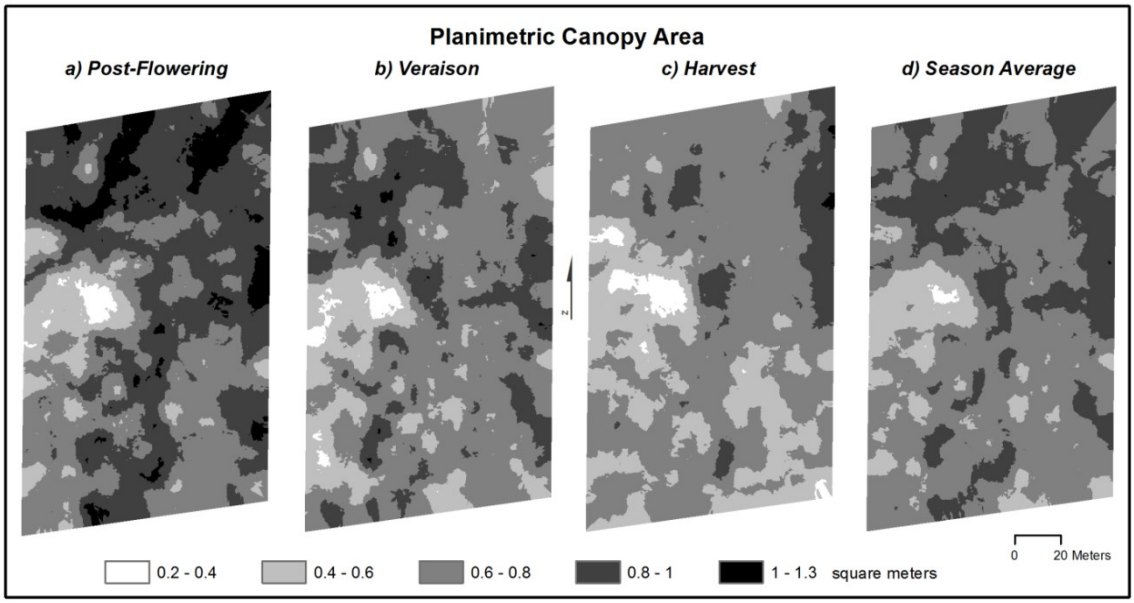

Figure 3.4. Observed canopy area (mean area of RGB and NIR segments) for the study vineyard at (a) post-flowering, (b) veraison, (c) harvest, as well as for (d) the entire growing season (season average).

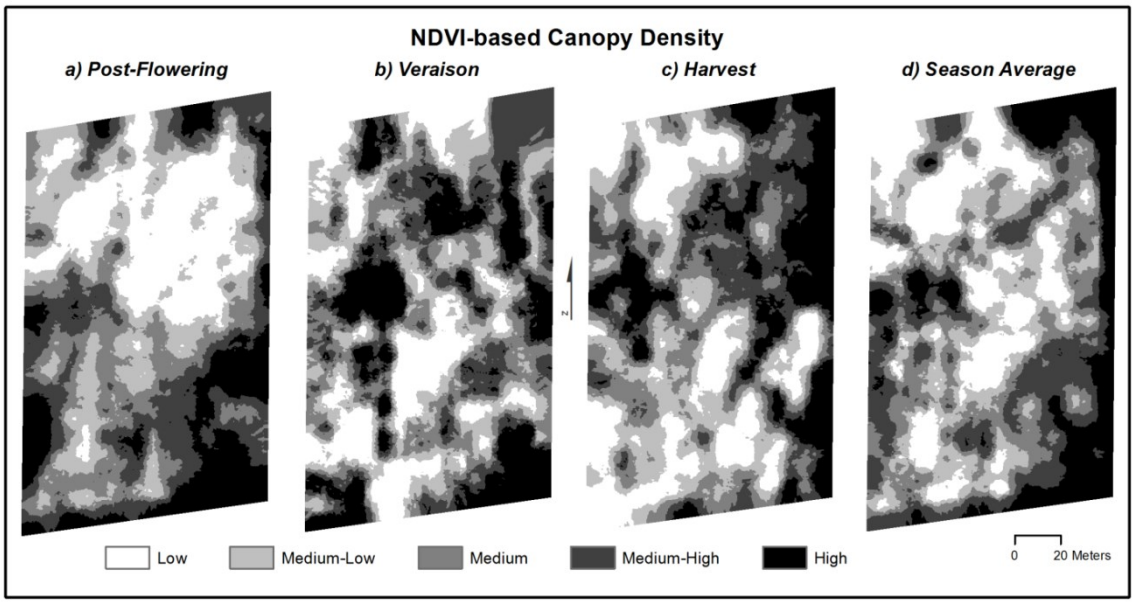

Figure 3.5. Observed canopy density (NDVI-based) for the study vineyard at (a) post-flowering, (b) veraison, (c) harvest, as well as for (d) the entire growing season (season average).

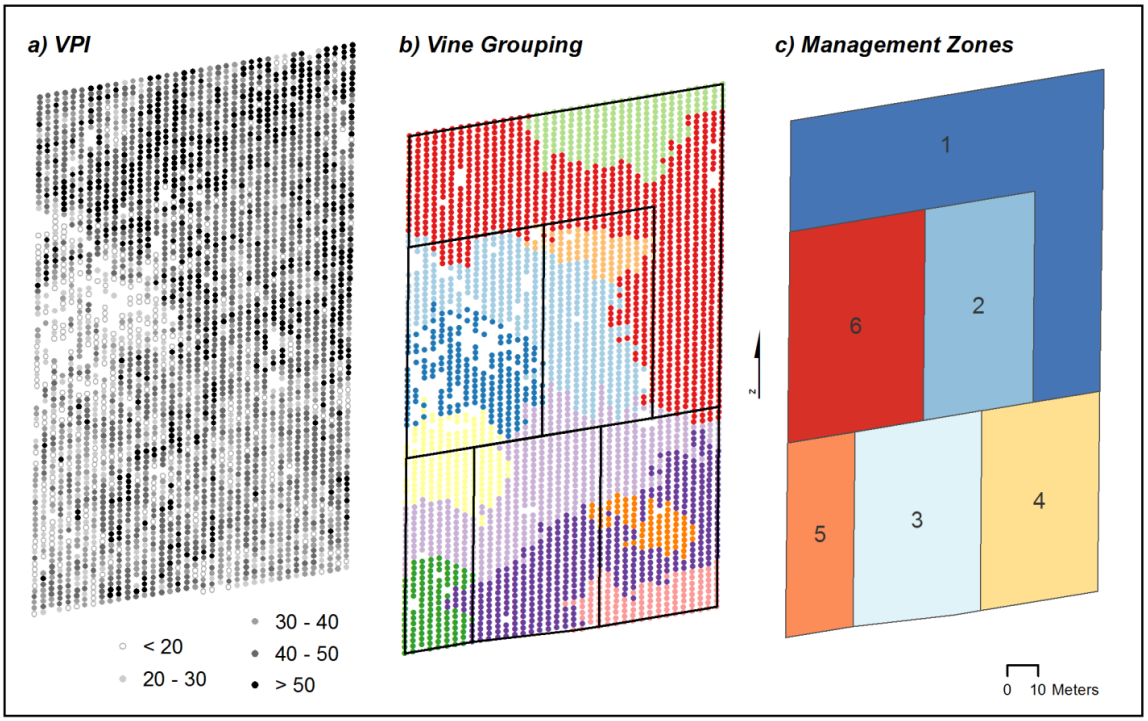

Figure 3.6. Vine performance analyses including (a) the calculated vine performance index or VPI, (b) vine grouping results, and (c) proposed management zones numbered from 1 (high vigor) to 6 (low vigor).

CHAPTER IV

A NEW METHOD FOR VISUALIZING AND QUANTIFYING VINEYARD CANOPY DENSITY[3]

Introduction

Identification of spatial variation in leaf canopy density is important in crop management and for accurate biomass estimation. Within viticulture specifically, being able to recognize such disparities provides vineyard managers the opportunity to examine and address this spatial variability by adjusting the management scheme with the potential of improving the crop (Proffitt et al. 2006). Vine canopy density is vital in protection and production of high quality winegrapes. Moderate canopy density is typically desired, depending on the time of the growing season, specific location, and grapevine varietal (Creasy and Creasy 2009). Passive remote sensing datasets like aerial and satellite-based imagery of vineyard canopy can successfully identify such variability in canopy density and subsequent crop health within vineyard blocks (Hall et al. 2003, 2011; Johnson et al. 2003a, 2003b). Calculated vegetation indices, namely the normalized difference vegetation index (NDVI; Rouse et al. 1973), highly correlate with changes in canopy density measured by leaf area index (LAI; ratio of leaf surface area to ground surface area following Johnson (2003)). More recently, other datasets, like those provided by active remote sensors, are beginning to play a role in such viticultural research.

Unlike imagery, both terrestrial and airborne discrete return light detection and ranging (lidar) systems provide an additional third dimension of information (Z) for

[3] This chapter was published with the title "Visualizing and Quantifying Vineyard Canopy LAI Using an Unmanned Aerial Vehicle (UAV) Collected High Density Structure from Motion Point Cloud" in *Remote Sensing* (2013, Issue: 5(5), Pages: 2164-2183).

height and volumetric analysis. Terrestrial lidar has been successfully implemented to explore biophysical properties of vines (Rosell et al. 2009; Keightley and Bawden 2010; Llorens et al. 2011a, 2011b; Sanz-Cortiella et al. 2011). Keightley and Bawden (2010) measured uprooted grapevine trunk biomass with a stationary terrestrial lidar scanner. Rosell et al. (2009) utilized a tractor-mounted lidar sensor to create three-dimensional (3D) scenes of vineyards and fruit orchards. These lidar data were found to be strongly correlated with field measurements and therefore were highly accurate when used to portray the entire crop structure (trunks, canopy, and trellis systems if present). Similarly, Llorens et al. (2011b) generated whole vineyard 3D canopy structure maps with a lidar sensor mounted on a tractor while moving between vine rows. Llorens et al. (2011a) modeled leaf area and accurately gauged ideal pesticide amounts for vineyards and orchards. Sanz-Cortiella et al. (2011) used a tractor-mounted lidar system to study pear tree leaf density and found that the sensor provided an accurate 3D representation of leaf area but was highly affected by the height and angle of the sensor. Rosell et al. (2009) suggested that lidar data may be used to explore relationships with LAI. Llorens et al. (2011b), in turn, reported a moderate, positive correlation between number of lidar returns and measured LAI of a given portion of canopy. Similarly, high total leaf area of juvenile trees has been shown to directly correlate with point density of the terrestrial lidar point cloud (Seidel et al. 2011). In all of these cases, collected terrestrial-based lidar point clouds exist in a Cartesian coordinate system requiring a highly accurate location tracking global positioning system (GPS) mounted on the lidar sensor platform (tractor or otherwise) for proper georectification (Llorens et al. 2011b).

To a much lesser extent, airborne lidar datasets have proven useful in visualization of vine canopy and vineyard structure leading to accurate delineation of vineyard parcels (Mathews and Jensen 2012a). Although not specifically applied to viticulture, airborne lidar datasets can confidently predict LAI and other biophysical characteristics of tree vegetation by calculating several height-based metrics (Means et al. 2000; Popescu et al. 2004; Jensen et al. 2008; Peduzzi et al. 2012). Yet another method, that of statistically-based modeling, was implemented by Louarn et al. (2008) to look at single vine canopy and explore potential light interception for different grapevine varietals. For sake of practicality and cost though, airborne and terrestrial lidar datasets have proven difficult to acquire (Omasa et al. 2007) and repeat acquisitions are usually cost-prohibitive. Due to this, alternative ways to gather similar datasets have emerged like Structure from Motion (SfM; Leberl et al. 2010). Most recently, successful vineyard canopy modeling has been completed by way of SfM primarily for visualization (Turner et al. 2011; Dey et al. 2012). Across an entire vineyard, Turner et al. (2011) compared a pre-growth and full-growth point cloud of vineyard canopy in natural color by way of SfM. At a more reduced scale, another SfM-based vineyard analysis accurately classified vine structures (grapes, canopy, trellis and other hardware) along portions of a vine row (Dey et al. 2012).

SfM is a computer vision technique based heavily on the principles of photogrammetry wherein a significant number of photographs taken from different, overlapping perspectives are combined to recreate an environment (keypoint matching of features across images). SfM stems from a number of works, namely that of Snavely (2008) and Snavely et al. (2008), which documents the development of the Bundler

algorithm that is now employed by the most well-known SfM platform: Microsoft PhotoSynth. Although SfM was first intended to be used for ground-based applications, it has been used from aerial platforms and for geographic applications (Leberl et al. 2010; Kaminsky et al. 2009; Dandois and Ellis 2010; Harwin and Lucieer 2012; Mathews and Jensen 2012b; Turner et al. 2012; Fonstad et al. 2013). For use in such geographic applications, the SfM output, which is made up of an internally consistent arbitrary coordinate system, must be transformed to real-world coordinates. Accordingly, georeferenced SfM datasets are similar to lidar datasets consisting of a set of data points, the keypoints generated from SfM product creation, with X, Y, and Z information (known as a point cloud in its entirety) with additional color information (red, green and blue [RGB] spectral) from the photographs. The cost to collect SfM point clouds remains very low compared to lidar; hence, there exists great interest in using such methods to model in 3D.

SfM-based 3D models have been used extensively in recreating urban and cultural features (Snavely et al. 2008; Kaminsky et al. 2009; Mathews and Jensen 2012b; Pollefeys et al. 2004), and to a lesser extent topography and other surface features (Rosnell and Honkavaara 2012; Fonstad et al. 2013) such as vegetation (Dandois and Ellis 2010; Turner et al. 2011). The accuracy of the SfM approach, however, is often less trusted than other similar datasets provided by airborne or terrestrial lidar systems. Despite this, a number of research results insist that SfM point clouds are in fact comparable if not more accurate than lidar point clouds (Leberl et al. 2010; Dandois and Ellis 2010; Fonstad et al. 2013). Unfortunately, comparison of such datasets is difficult

unless both datasets are collected for the same research purpose and at similar point densities.

The SfM approach with vegetation has proven more difficult than with urban and other features because of their more complex and discontinuous structures (Omasa et al. 2007; Dandois and Ellis 2010). Keypoint matching is considerably more difficult when working with vegetative features because of leaf gaps, repeating structures of the same color, and inconsistent/random geometries. The resulting SfM point cloud can therefore be more random and less uniform in its spatial coverage (Dandois and Ellis 2010). Despite this, satisfactory results of vegetation modeling (canopy height) with SfM have been reported (Dandois and Ellis 2010). Placement of colored field markers, modification of the SfM algorithms, increasing the number of photographs captured, and taking images at higher altitudes were just a few of the suggestions provided to improve vegetation modeling when implementing the SfM approach (Dandois and Ellis 2010).

Besides Turner et al. (2011) and Dey et al. (2012), no studies have reported specifically modeling vineyard vegetation with SfM. More importantly, no studies have explored the relationship between SfM point clouds and in situ LAI measurements as have been explored with lidar data. Consequently, this study uses SfM to create a 3D vineyard point cloud to visualize vineyard vegetation as well as attempt to predict vine LAI based on information derived from the created SfM point cloud. A number of metrics are calculated with extracted points from the SfM point cloud that are compared to LAI measurements to explore how LAI relates to said metrics (point heights, number of points, etc.).

Materials and Methods

Study Site

The Texas Hill Country American Viticultural Area (THCAVA) was officially recognized in 1991 and is located in central Texas west of Austin and north of San Antonio (Figure 4.1). This viticultural area contains 22 wineries, encompasses parts of 22 counties, and covers an area of over 36,000 square kilometers (14,000 square miles). This study looked at two contiguous vineyard blocks managed by one winery within the THCAVA. These two blocks of trellis-trained Tempranillo (Vitis vinifera) vines are shown outlined in red in Figure 4.2 and total approximately 1.9 hectares (4.8 acres). Within this outlined area, the eastern block (separated by the dashed red line) was planted prior to the western block. Due to this, vines in the western block have smaller, less dense canopies than those in the eastern block. Both blocks are included to provide obvious leaf canopy size and density variation throughout the study site to enhance the robustness of the model results. All of the study vines are between four and six years of age. The vines within the block immediately west of the highlighted study vines are not included because they are less mature and are a different varietal. In total, the study blocks include 38 rows of vines with approximately 65-95 vines per row (around 3,000 vines total). The precise location of the study vineyard within the THCAVA is not disclosed as requested by the property owners.

Data Collection

Point cloud creation and 3D modeling was completed using the SfM approach discussed previously. This method provides a low cost alternative to generate 3D data similar to lidar data and for sake of practicality remains a highly replicable method for

future studies. Data were collected during the veraison phenological phase of the growing season (nearly 100% or full veraison) following Stamatiadis et al. (2010). This phenological phase was chosen for modeling because during phases prior to this the canopy may not be fully developed, while phases after this may be highly affected by canopy management practices like leaf thinning (Creasy and Creasy 2009). Additionally, observations from this part of the growing season have been shown to highly correlate with eventual vine performance in studies using multispectral imagery (Hall et al. 2011; Johnson et al. 2003a).

Over 200 images were taken of the study vineyard with an unaltered, off-the-shelf Canon PowerShot A480 (RGB) digital camera. Images were captured with the use of a remote controlled Hawkeye unmanned aerial vehicle (UAV) system (www.ElectricFlights.com, Kingsland, Texas, USA). The camera was mounted in the UAV facing downward for nadir capture. This kitewing plane UAV platform was flown in vine row direction (north-to-south) for multiple passes to collect the imagery. This flight path was employed because the study UAV flies in a more stable fashion when flown directly into (to the south) or with (to the north) the wind. Flying height ranged from 100 to 200 meters above ground. The Canon Hackers Development Kit (CHDK; chdk.wikia.com) intervalometer script was employed to continuously capture images every second during flight. Images not captured within this altitude threshold (at or near takeoff, landing, and during ascent/descent) were not included in image processing and are not reported in Table 4.1. Images were captured on a cloud free day (16 June 2012) around 11:00AM to minimize the effect of shadowing between the vines rows. The UAV captured images at nadir and varying oblique angles. Oblique images were captured both

unintentionally, during side-to-side UAV movement caused by crosswinds, and intentionally, by way of banking (leaning) the aircraft. Oblique images were included to better gain a sense of and model the canopy in 3D, instead of inputting only nadir images. Increased number of differing angles/perspectives with overlap only serves to further improve the SfM end product (Dandois and Ellis 2010).

The difficulty of SfM keypoint matching with vegetation has been noted (Dandois and Ellis 2010) due to the uniform and repeating nature of the surface area being modeled. Leaves can also be shiny due to their wax-like nature, further deterring proper keypoint matching. To address this and aid efficient SfM product creation, a number of colored targets were placed in the field prior to image capture. Nine, 25-centimeter wide plastic buckets (pails) were placed in random locations upside-down atop trellis support posts throughout the vineyard. These adornments did not touch the vine canopy growing on the trellis below. The buckets were painted several different flat (non-shiny) colors (orange, yellow, white, and gray) to provide added visual distinctness from the surrounding canopy (green), repeating trellis structure (black), and underlying soil (red/brown). The discreteness of these targets within the vineyard landscape provides cursory SfM keypoints from which further keypoints can more easily be generated. This is assumed to create a more accurate SfM model overall as well as potentially reduce processing time. In total, nine buckets were considered enough to aid in cursory keypoint matching, although best practices of employing such aids has yet to be tested in SfM studies.

To properly georeference the SfM point cloud, five ground control points (GCPs) were accurately located using a Trimble GeoXH GPS with an external antenna averaging

a total of 200 separate GPS positions for each location (X,Y: NAD 1983, UTM Zone 14N; and Z: NADV88). GPS acquisition was limited to a maximum position dilution of precision (PDOP) of three. Differential correction of the collected GPS positions was completed using the Trimble GPS Analyst Extension in ArcGIS and resulted in a mean estimated error of 0.1083 m. GCP targets were crafted out of sturdy foamboard, sized 0.6 m by 0.6 m, and painted red with white and black center targets following Aber et al. (2010). This ensures proper identification within the resulting point cloud model. The GCP targets were designed with further distinct colors to additionally aid in SfM keypoint matching much like the previously discussed colored buckets.

LAI data were collected using an AccuPAR LP-80 ceptometer (Decagon Devices, Pullman, Washington, USA) immediately following UAV image capture for improved accuracy with higher sun angles (Lopez-Lozano et al. 2013). Similar to Johnson (2003), offset stratified sampling was implemented consisting of every tenth vine in every fifth row starting with the easternmost row (alternating between the first and fifth vine to begin each sample row starting from the north). A total of 67 vines were sampled for LAI measurements. Ceptometer measurements were taken directly beneath the central portion of the vine canopy beside the vine trunk in a perpendicular fashion to the vine canopy row similar to the accurate measurement protocol M3 reported by (Lopez-Lozano et al. 2013). All sample vines were GPS located based on averaging 30 positions rather than 200 as was employed with the GCPs (mean estimated error of 0.1660 m). Following differential correction of the captured GPS positions, collected LAI information for each vine was attributed to their respective locations.

Data Processing

The 3D vineyard point cloud was created automatically using Agisoft PhotoScan (Agisoft LLC, St. Petersburg, Russia). It should be noted that manual processing by way of open source software is also possible, but remains more time consuming (Dandois and Ellis 2010; Mathews and Jensen 2012b; Fonstad et al. 2013). Of the total 206 images captured, 201 were input into the model. Five images were not included because they were either overly blurry or did not capture the study vineyard within the field of view. The latter was due to the UAV having to turn around at the end of the flight line. Such images can potentially introduce noise into the model as well as slow processing time (more images; blurry images are more difficult to identify matching keypoints across images). PhotoScan, much like Microsoft PhotoSynth (Microsoft Corporation, Seattle, Washington, USA), automatically generated the 3D model based on input images. This model was then manually georeferenced within PhotoScan by way of identifying the GCPs within the model and substituting those data point's arbitrary coordinates with the GPS measured coordinates and applying this locational transformation to the entire point cloud. The georeferenced point cloud was then exported using the high point density setting to LAS file format.

Point cloud processing was completed using LP360 (QCoherent Software LLC, Madison, Alabama, USA). Manual removal of noise within the point cloud was first necessary to remove obvious outliers not representing actual ground features (points 0.5 m or greater beneath the ground surface and points 10 m above the ground surface based on field observation). The spatial extent of the dataset was also reduced to decrease processing time. Points greater than 70 m away from the study block outline were

removed from the dataset. Following this manual effort, the point cloud was processed similar to that of a lidar dataset with automatic point filtering to separate ground points from non-ground points. LP360 uses an adaptive TIN method to first approximate a terrain surface using the lowest elevations in a large grid and then iteratively refines the surface until an accurate representation of bare earth points is achieved (Axelsson 2000). After automatic classification, additional manual classification was necessary to reassign obvious misclassified points to their proper class for improved ground—non-ground separation.

The classified LAS file was imported into ArcGIS (ESRI, Redlands, California, USA) as separate vector files of ground and non-ground points. Ground points were used to create a very high spatial resolution (0.25 m) digital terrain model (DTM) using ordinary kriging. To create relative height of non-ground points, the DTM height was subtracted from the absolute height of each non-ground point. This resulted in meaningful heights for each point in the non-ground point cloud representing measurements from the ground surface rather than from sea-level.

Data Analysis

Non-ground points were extracted based on proximity to the LAI sampled vines. Points were extracted using rectangles sized 1 m by 2 m, centered on sample vine trunk locations, and orientated north-to-south in line with the vine rows. Even though LAI measurements were only taken at the central base of each vine, these extraction zones are most representative of the full canopy of each vine, more so than a circular buffer around the vine location would be. This is due to the trellis system onto which the vines are trained to grow and the inherent geometry. Vine-to-vine spacing within each row is 2 m.

Therefore, a meter to the north and the south of each vine trunk location represents canopy from that particular vine. Likewise, canopy width is no greater than a meter wide (east-to-west), which provides enough space to include the entire canopy.

Following extraction of non-ground points to each sampled LAI vine, several metrics were calculated to explore correlations with the LAI measurements following Popescu et al. (2004) and Jensen et al. (2008). These metrics include the count or number of points within each vine's zone as well as several height-based metrics such as mean height, variance, standard deviation, coefficient of variation, kurtosis, percentiles (10^{th}, 20^{th}, 30^{th}, 40^{th}, 50^{th}, 60^{th}, 70^{th}, 80^{th}, 90^{th}, 100^{th}), percentile differences (100^{th}–10^{th}, 90^{th}–20^{th}, 100^{th}–50^{th}), and percentile point ratios (i.e., number of points above percentile heights relative to the total number of points within the extraction zone). Furthermore, points with heights below 0.3 m and above 2.3 m were not included in metric calculation. These points were excluded based on field observation, which determined that points at these heights could not represent vine canopy. The relationship between these metrics and the measured LAI were modeled using the All Possible Models (i.e. best subsets regression) function in the JMP statistical package (SAS Institute, Cary, North Carolina, USA).

A square root transformation (LAI_{SQRT}) was applied to the field-measured LAI data to meet the assumption of data normality (minimize skewness and kurtosis). LAI_{SQRT} served as the dependent variable (Y) while the height-based metrics served as the independent or explanatory variables (X's). Sample vines with low point counts of less than six were excluded from analysis. This condition was imposed based on prior consultation with an expert statistician to determine the minimum number of points

necessary for reliable metric calculation (i.e., variance, coefficient of variation, etc.). As such, the total number of observations included in the regression analysis was limited to 44 of the original 67 vines.

Correlation analyses between each metric and LAI_{SQRT} were performed but yielded weak results for individual metrics (-0.3372 to 0.3941). However, as is common in lidar-based analyses, 3D-dervied LAI estimates typically require several predictor variables to accurately quantify structural characteristics such as LAI. In that regard, weak individual correlations were not viewed as a limitation for further analysis. The All Possible Models procedure was implemented to provide a range of one-to-six covariate term models. Candidate models were selected based on a several criteria including R^2, adjusted R^2, RMSE, individual covariates, and overall model significance ($\alpha \leq 0.05$). The candidate models were also subjected to a Predicted Residual Sum of Squares (PRESS) analysis, which was used to determine the prediction error of each candidate model. The candidate model with the smallest difference in model root mean square error (RMSE) to PRESS RMSE was selected as the final model.

Results

SfM Results and Point Cloud Visualization

Characteristics of the vineyard SfM model are reported in Table 4.1. Of the 206 total images captured by the digital camera during UAV flight, five were not input into the SfM model. From the 201 input images, PhotoScan exported a point cloud with a total of 462,959 points. After removal of noise within the dataset, a total of 432,184 points remained (93.3% of original), of which 333,835 points were classified as ground (72.1% of original) and the remaining 98,349 points as non-ground (21.2% of original).

Typically, points flagged and removed as noise were located much higher or lower than expected and did not represent any actual feature on the ground or within the vine canopy. The extent of the dataset was also reduced to decrease processing time and the points located outside of the clipped extent were also classified as noise, comprising 6.7% of the original output point cloud.

The filtered point cloud provides a clear 3D visualization of the study site as shown in Figure 4.3 at an oblique angle looking north. Points classified as ground are shown in gray, while points classified as non-ground are shown in orange. The background, and therefore any area not being covered by data points, is displayed in black. The vine canopy with its distinct trellis-trained rows quickly becomes evident, especially at the vineyard edges where features are not found aboveground. Likewise, taller objects like the trees to the north of the study vineyard are properly replicated by the SfM model.

For further depiction of the filtering results, a nadir view of an actual UAV captured image (Figure 4.4a) and the classified point cloud of the same extent (Figure 4.4b) are shown in Figure 4.4. This is the northwesternmost portion of the study vineyard, the extent of which is denoted with a red outline in Figure 4.4b. The repeating linear structure of the vine canopy is again apparent in this case. Other objects on the ground are also well classified such as the vehicle in the upper-right of Figure 4.4a. The points representing the vehicle are correctly classified as non-ground. Likewise, other features like the fence enclosing the vineyard (between the vehicle and the start of the vine rows) and the building northwest of the vehicle are also captured by the point filtering as non-ground. The non-ground points representing vine canopy though, are patchy and less

uniform than found in other areas of the vineyard (refer back to Figure 4.3). This is not due to misclassification but rather less abundance of points in this area.

Due to the overlap of the UAV images input into the SfM model, the point density across the study vineyard is not uniform. Figure 4.5 shows both ground point density (left) and non-ground point density (right). Overall, ground points have a higher density than non-ground points because many more points are classified as ground than non-ground (333,835 vs. 98,349). The spatial pattern of high point density though, remains similar across both sets of points. Both display high densities of points over the central and western sections of the study vineyard. This is where the most overlap in the input images occurred and results in more keypoints within those areas. Additionally, the northern edge of the vineyard shows higher degrees of point density because this was the staging area from which the UAV was launched and landed, resulting in more images being taken at the north end of the vineyard compared to the south. Mean point densities within the study vineyard block (the extent as shown in Figure 4.5) resulted as follows: 9.07 points per square meter for all points (unclassified), 6.33 points per square meter for ground classified points, and 2.74 points per square meter for non-ground classified points.

Despite spatial variation in point density, the SfM point cloud can be used to create powerful visualizations of the study vineyard at a number of scales (see Figure 4.6a-c) including whole vineyard (Figure 4.6a), partial vineyard or vine row (Figure 4.6b), and partial vine row or per vine (Figure 4.6c). The three-dimensional perspective provided in this case increases the ability to perceive the SfM representation of the vine canopy and the density of the non-ground points. This is especially the case with Figure 4.6b in

which the low angle provides a view similar to that of standing at the study site looking down the vine rows. Elements added for visual effect include: colored DTM surface, lines representing trellis wires, red poles with cone bases to represent the sampled vine trunk locations and generalized vine heights, red transparent partitions to highlight the sample vine rows, and extraction rectangles (boxes). The 1 m by 2 m extraction rectangles exist within 0.3 to 2.3 m above the DTM surface and are displayed in a transparent brown hue only in Figure 4.6c. All of the points within these shapes were extracted and attached to that particular LAI sampled vine.

Ceptometer collected LAI data throughout the study vineyard resulted in a large range of values from 0.54 to 5.65. Indeed, a large variation in canopy density across the study site existed, which may be attributed to ceptometer uncertainty (Lopez-Lozano et al. 2013; Hyer and Goetz 2004; Garrigues et al. 2008). The spatial distribution of these collected values are interpolated and shown with Figure 4.7. This figure confirms the previously mentioned east-west block differentiation in canopy density based on age of the vines where the more established vines to the east have larger, denser canopies while the vine canopies to the west are considerably smaller and less dense. The location of the stratified sample of 67 vines is also shown along with the vine row structure. Spacing of the sample points appears to be less uniform in the western block (greater distance between sample points); this is due to removal of vines in the western block, especially noticeable in the last sampled row furthest west.

Relationship between SfM Output and LAI

In total, 44 of the 67 sampled vines had point counts of six or greater. These 44 observations (n) were used to evaluate the relationship between the SfM height metrics

and field-measured LAI (Table 4.2). The final model was selected based on the best subset of covariates and explained 57% of the variation in field-based measures with an RMSE of 0.24. The six covariate terms used to predict LAI_{SQRT} include the variance (Var), coefficient of variation (CV), the 50^{th} and 90^{th} percentile heights (Per5 and Per9), the difference between the 100^{th} percentile height and the 50^{th} percentile height (Per10-5), and the ratio of the number of points above the 60^{th} percentile to the total number of points within the extraction zone (RatioPer6). A summary of the parameter estimates and overall model performance is provided in Table 4.2.

The regression results are shown graphically in Figure 4.8 with observed LAI on the X-axis and predicted LAI on the Y-axis. Estimates were back-transformed to LAI and the observed vs. predicted values are shown around a one-to-one relationship line (gray) and a regression fit trend line (black).

Discussion

General Study Limitations

This study presents preliminary findings using SfM to visualize vine canopy and predict LAI. The scope of this study remains limited to a one-time data acquisition in July 2012 at a single vineyard site in the THCAVA. The potential utility of the presented method, therefore, remains limited to this dataset. Due to the high variation of SfM output (i.e. point density) based on image input, it is highly likely that the captured image data influences the success with which this method is employed. In general, comparative SfM studies exploring the degree to which SfM models vary in recreating the same subject at or near the same time period would be very useful. Specifically, further SfM-based viticultural research would benefit greatly from replicating such analyses over

several data acquisitions within the growing season, over several years, and across several vineyard sites. At that point, the robustness of this method can fully be recognized. Continued success and advancement of this method may also lead to exploration of differences between grapevine varietals and management practices (more or less leaf thinning).

Though LAI measurements over the study area were obtained in a manner to mitigate potential error sources, error may have been introduced in the LAI data acquisition either through the sampling strategy or measurement theory. For example, the ceptometer requires specific parameters that can influence how LAI is calculated by the device including illumination conditions and leaf angle distribution (Garrigues et al. 2008). Slight changes in illumination conditions throughout the measurement period can also influence LAI measurements because the device requires information on the total to direct flux (Garrigues et al. 2008). Lopez-Lozano et al. (2013) reported that the best results from a SunScan ceptometer were obtained under very specific illumination conditions, namely when the sun was neither directly overhead nor parallel to the vine rows. Further, even though the number of PAR sensors was limited to account for the relatively narrow width of the vine rows, the physical footprint of the sensor likely varied despite best efforts to position the sensor exactly the same for all measurement locations. Lastly, LAI measurements are likely influenced by the trellis system itself, as the wooden components and wires influence light interception.

SfM as an Alternative Source of High-Density 3D Data

The low cost and relative ease of creating 3D visualizations by way of SfM will likely see an expansion of use within the coming years. Inputting 201 images to

PhotoScan, with relatively little user input, resulted in a dense (unclassified) point cloud with a mean of 9.07 points per square meter for use in visualization and analysis. A relative disadvantage of the SfM method of creating 3D datasets, however, is the random nature of SfM-obtained points within the output point cloud, since points can only be assigned based on conjugate feature recognition, or the ability of the matching algorithm to identify similar features in two or more images. Spatial variation in point cloud density is likely to occur when creating SfM-based models even with careful planning of image capture. As Figure 4.3 illustrates, higher point densities tended to result from increased overlap between images. As such, a potential solution would be to ensure that the entire study area be redundantly imaged. In short, to minimize spatial variation in point density across a study area, UAVs equipped with autopilot and flight planning functionality could be programmed with automated image capture to ensure more equal study site coverage. This includes obtaining a great deal of overlap of images at the edges of the study site, which can be obtained by buffering the desired coverage area by a generous distance.

SfM-acquired topographic datasets were comparable to airborne lidar data in terms of point densities and horizontal and vertical precision (Fonstad et al. 2013). For vegetation-based studies, such as those presented here, the ability to image the ground surface due to the trellis-row nature of the vineyard provided an opportunity to filter ground from non-ground points and generate SfM-derived terrain and canopy datasets. This may not always be the case, especially in areas of high canopy density, where the ground is not visible to the passive imaging system. However, if lidar data are available for an area, the SfM technique may be used to acquire vegetation canopy information

such as height or percent cover as long as the lidar data are used to model the bare ground (Dandois and Ellis 2010).

As it currently stands, multi-temporal lidar acquisitions are not economically feasible for fine/small scale acquisitions; however, a simple, low cost aerial camera system can be easily configured to provide similar information and more frequently than commissioning a lidar acquisition. Nonetheless, we explicitly state, that unlike lidar, the accuracy of the projected point coordinates are dependent on the geometric transformation between field-measured GPS positions and clearly identifiable features in the imagery and point density is variable and dependent on image overlap and conjugate surface features. Future research in SfM-acquisition for 3D datasets would certainly benefit from guidance regarding image acquisition and spatial redundancy as well as optimal placement of GCPs to distribute transformation uncertainties equally throughout the study area as this may affect location (X,Y) and height (Z) accuracies.

SfM LAI Estimates Compared to Lidar and Spectral-based Approaches

The results of this study are similar to accuracies reported from other vineyard site lidar-based LAI estimation. For example, Llorens et al. (2011b) was able to account for 49% of the variability of field-measured LAI using the number of lidar returns from a tractor-mounted terrestrial lidar. Llorens et al. (2011a) achieved a maximum R^2 value of 0.40 for a regression model that used the number of lidar canopy returns acquired from a tractor-mounted terrestrial lidar. An exception to other lidar-based approaches is Arno et al. (2013), who achieved exceptional R^2 values of up to 0.99 using a tree area index metric derived from very high density terrestrial lidar scanner data.

Passive optical imagery acquired by either aerial or satellite-based platforms has been the traditional data used to estimate LAI and has, with the exception of Arno et al. (2013) produced better results than lidar for vineyard canopy LAI. For example, Johnson (2003) used 4 m multispectral IKONOS imagery to calculate predictor variables based on NDVI and accounted for 91 to 98% variability in field-measured LAI over four different measurement dates. In another study, Johnson et al. (2003b) used NDVI derived from IKONOS imagery and was able to account for 72% of field-measured LAI. Using 0.25 m multispectral aerial imagery and a NDVI threshold of 0.6, Hall et al. (2012) calculated planimetric vine canopy area that accounted for 83% of the variability of LAI over several phenological stages.

Potential of SfM as a Source of 3D Data for LAI Estimation

Although the results of our SfM-derived LAI model only explained a moderate percent of variation in field-measured LAI ($R^2 = 0.567$), these results provide proof-of-concept in that SfM data, due to its similarity with lidar may be used to predict LAI for vineyards. However, several issues provide discussion points in terms of the SfM point densities. As mentioned previously, low point densities in portions of the vineyard were an issue that quickly became apparent during metric calculation of point- and height-based regression covariates. Out of 67 LAI-sampled vines, 23 field-measured LAI observations were excluded from regression modeling because the extraction zones surrounding the vines failed to have more than five points. Higher density of points may have led to an improved R^2 value between LAI and the SfM metrics, although we acknowledge that this relationship is not evident in the current modeled output.

Our regression analysis included a series of point- and height-based metrics. Additional research could address the calculation and implementation of more traditional lidar-derived metrics used to predict LAI such as the laser penetration metric (Zhao and Popescu 2009), laser penetration index, or the laser interception index (Barilotti et al. 2006). Lastly, higher point density may allow for analysis of points within the X, Y axis. Analysis within this plane at designated height profiles could lead to accurate estimates of vine canopy width and overall size. A metric like this could further bolster the regression model that currently is primarily based on height-based metrics. Such analysis was attempted in this study but was unsuccessful presumably due to the lack of points.

Conclusions

This study presented several visualizations of vine canopy from the whole vineyard to single vine scale based on a SfM-derived point cloud. This generated model of vine canopy was created by capturing 201 aerial photographs with a digital camera mounted on a kitewing UAV. The SfM point cloud was then classified as ground and non-ground with non-ground points representing vegetation. This method was successful at quickly, practically, and inexpensively recreating the vineyard environment at the study site including the vine canopy. Using extracted points from this point cloud, this study reported moderate success in relating measured LAI of vine canopy to SfM point cloud derived metrics with an R^2 value of 0.567.

More work utilizing this rapidly developing SfM-methodology is necessary. This is especially the case with vegetation related studies because of the added level of difficulty associated with it. At this stage, modeling vegetation with SfM remains highly experimental and only moderately successful as shown by this and other studies (Dandois

and Ellis 2010). The reasonable success of this method in such an early stage provides hope that this technique can be improved upon. The practical and inexpensive nature of the SfM method of 3D modeling makes it highly attractive to researchers and practitioners within a variety of fields.

Future work using SfM for vegetation should employ colored targets to aid in keypoint matching. Likewise, higher point density is always desirable and can be obtained by acquiring more images, although this will prolong processing time to generate the point cloud. Implementation of this SfM method to predict LAI of other types of vegetation, particularly in forestry, would be worth exploring. SfM point clouds could also be utilized to estimate volumetric variables like biomass. Within the realm of viticulture, using this method at and between each phenological phase (budbreak, flowering, veraison, and harvest) to quickly generate whole vineyard 3D maps of vine growth both for visualization and LAI would be useful for vineyard managers wanting to assess spatial variation in size and density of vine canopy. It would be worth exploring potential variability in the prediction of LAI based on phenological phase, where fuller or lesser dense canopies may improve the accuracy of LAI prediction.

Table 4.1. Inputs and outputs of PhotoScan and LP360 point cloud processing.

Total Images	**Discarded Images**	**Input Images**	**Entire Point Cloud**	**Noise Removed**	**Classified**	
					Ground	***Non-ground***
206	5	201	462,959	30,775	333,835	98,349
100.0%	2.4%	97.6%	100.0%	6.7%	72.1%	21.2%

Table 4.2. Results of stepwise multiple regression predicting LAI based on SfM derived metrics.

R^2: 0.567 | R^2 Adj.: 0.495 | RMSE: 0.236 n: 44 | F Ratio: 7.86 | p < 0.0001				
Term	***Estimate***	***Standard Error***	***t Ratio***	***Prob > |t| α = 0.05***
Intercept	4.61	0.979	4.71	< 0.001
Var	4.77	1.97	2.42	0.020
CV	-5.05	1.58	-3.19	0.003
Per5	-2.91	0.565	-5.16	< 0.001
Per9	1.85	0.422	1.38	< 0.001
Per10-5	-0.716	0.289	-2.48	0.018
RatioPer6	-2.45	0.996	-2.51	0.017
= 4.61 + (4.77 * Var) – (5.05 * CV) – (2.91 * Per5) + (1.85 * Per9) – (0.716 * Per10-5) – (2.45 * RatioPer6)				

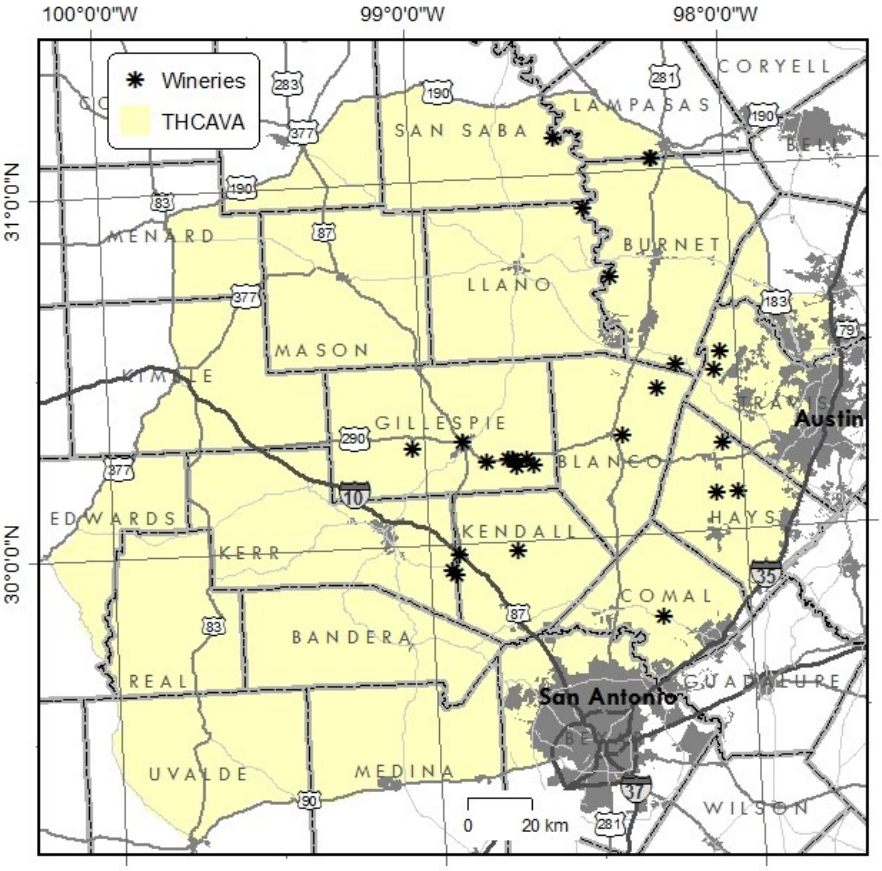

Figure 4.1. Study area in the Texas Hill Country American Viticultural Area with winery locations.

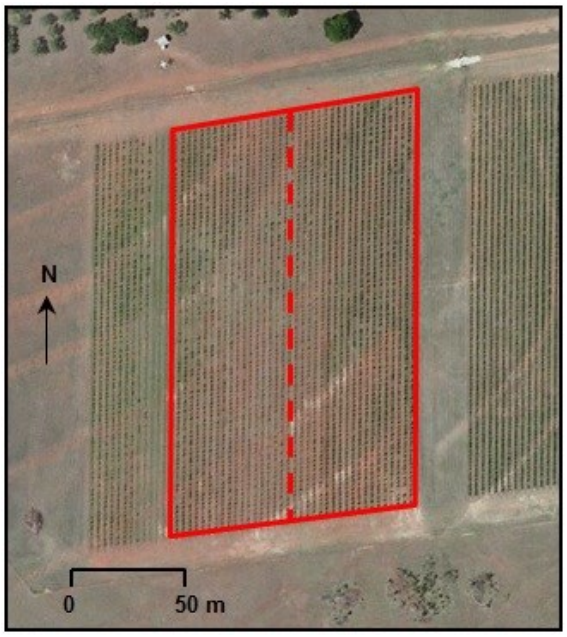

Figure 4.2. The study vineyard blocks.

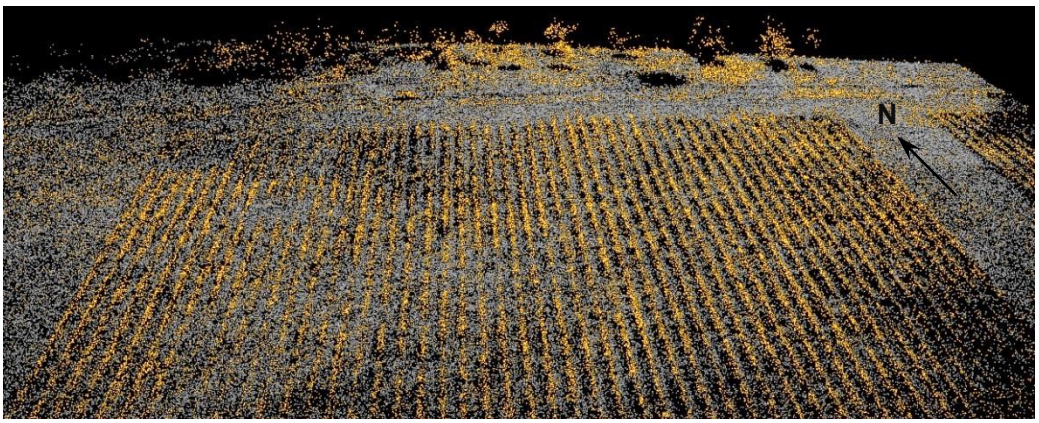

Figure 4.3. The filtered point cloud of ground (gray) and non-ground (orange) points.

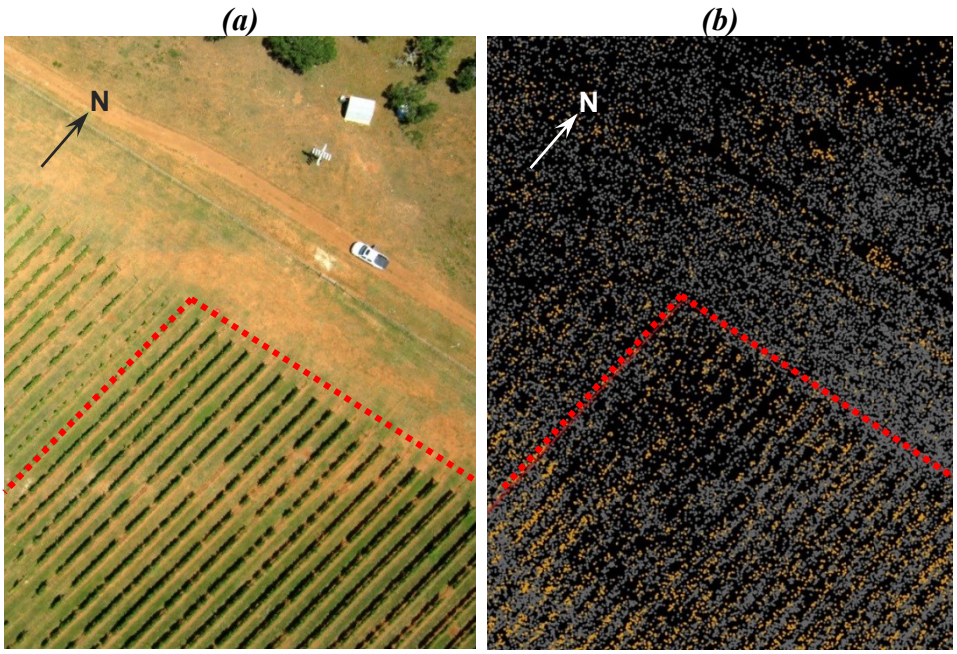

Figure 4.4. A comparison of an actual UAV captured image (a) and the filtered point cloud (b) for the same area.

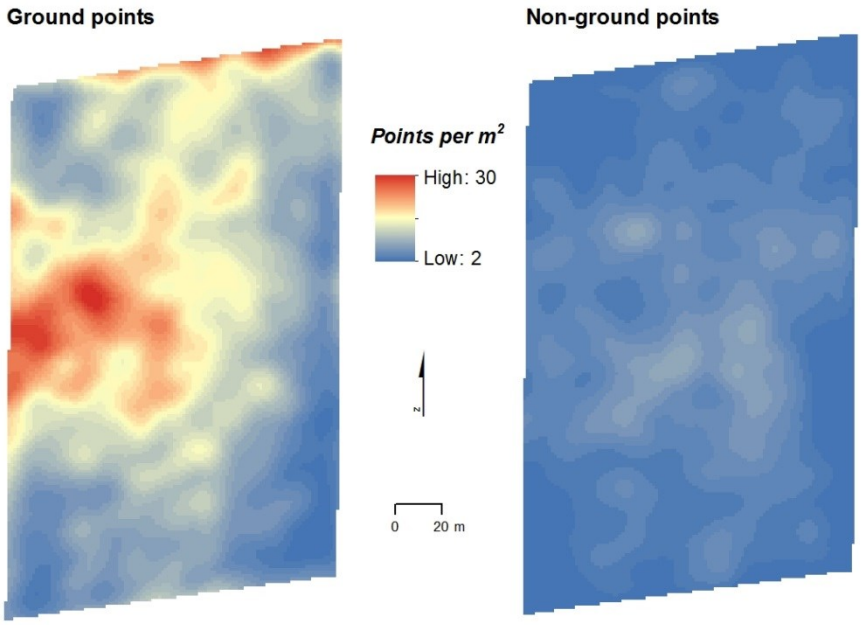

Figure 4.5. The density of points (local average number of points per square meter) for both the ground and non-ground point clouds.

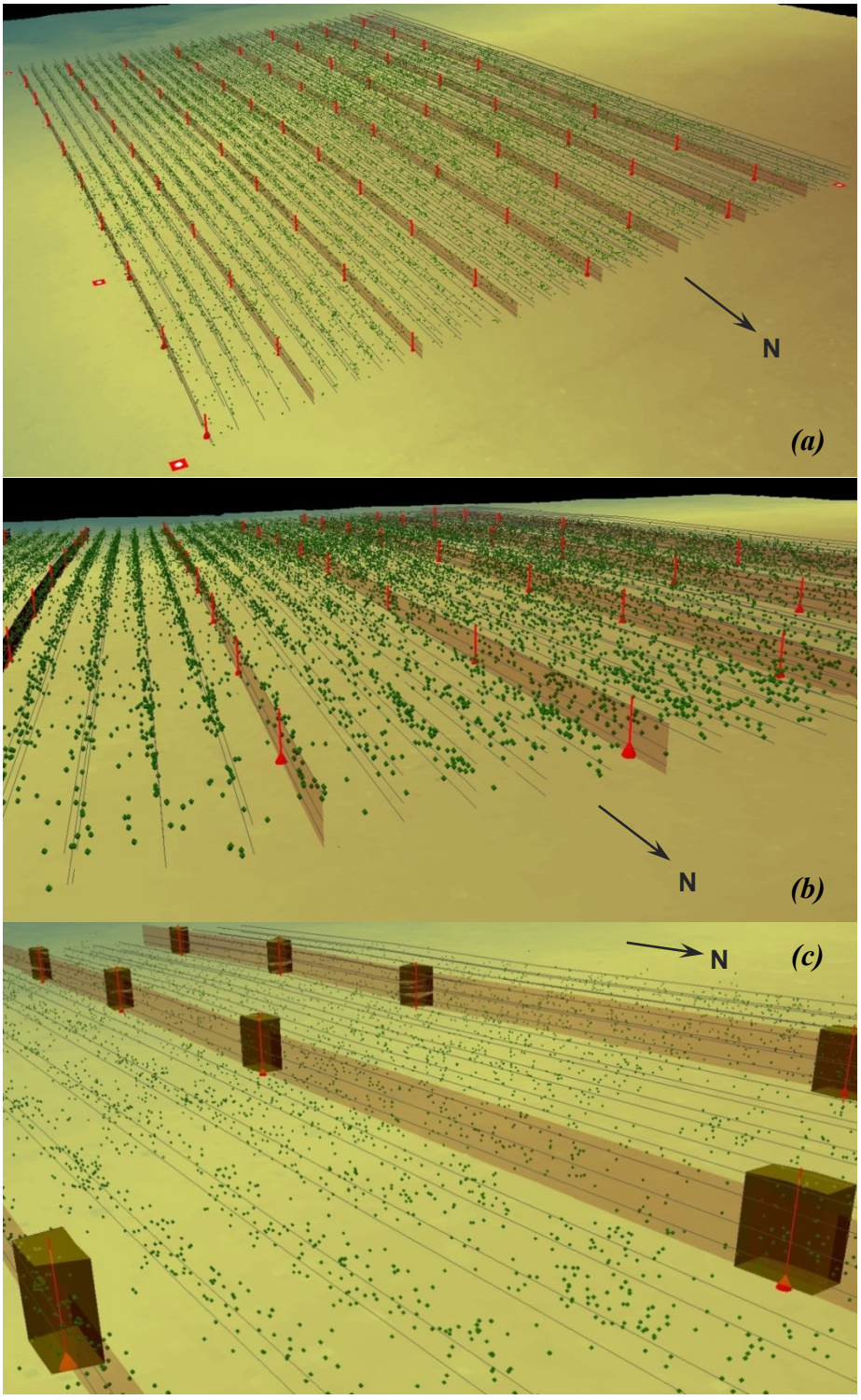

Figure 4.6. Three-dimensional visualization of the study vineyard (a, b, and c) including sample vines (red poles) with highlighted sample rows, non-ground point cloud (green spheres), projected trellis wiring (gray lines), and underlying DTM surface at (a) whole vineyard, (b) partial vineyard, and (c) per-vine scales.

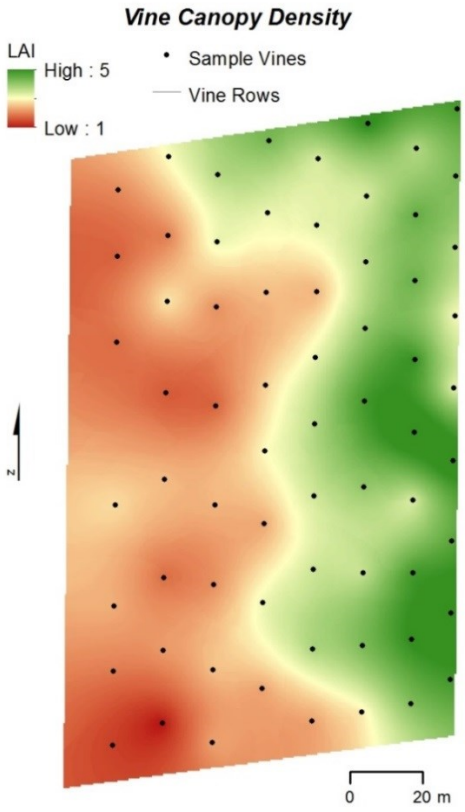

Figure 4.7. Canopy density (measured LAI) across the study vineyard blocks.

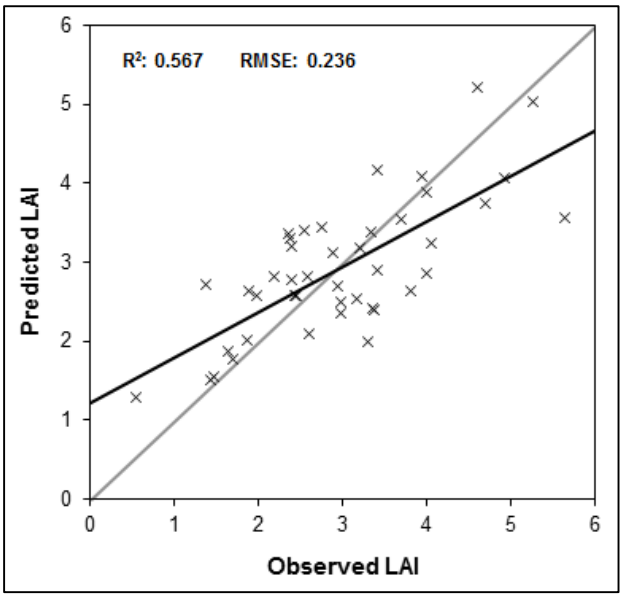

Figure 4.8. Scatterplot of LAI predicted with SfM height metrics (Y-axis) and field-measured LAI (X-axis).

CHAPTER V

CONCLUSIONS

Chapter II Accomplishments

Research objective 1 was addressed in Chapter II and entailed the setup and calibration of digital cameras for use as UAV-mounted remote sensors. This UAV and digital camera combination was very successful in capturing high quality aerial images of a vineyard study site in the Texas Hill Country. By way of SfM-processing, these images were used to produce site-specific DTMs for orthophoto production. On average (six orthophotos total), the created orthophotos exhibited very high spatial resolution of 25 mm. The generated orthophotos (RGB and NIR) were geometrically and radiometrically corrected for use in analysis. Due to the very high spatial resolution, the generated orthophotos are very useful for qualitative (visual) analyses. As for radiometric accuracy and subsequent quantitative analyses, the digital cameras and empirical line method employed was deemed inadequate for the blue and green bands in producing accurate estimates of spectral reflectance. In fact, all of the visible bands (including red) were susceptible to being over- and underestimated by the digital camera. Of the four produced bands, regression analysis showed that the red and NIR bands were the most radiometrically accurate. The red and NIR bands were still associated with an amount of error in the estimates of reflectance. In the end, Chapter II successfully assembled a very low-cost system and proposed a practical, replicable methodology that even with its discussed weaknesses would be a useful, adoptable system and method for other researchers and practitioners.

Chapter III Accomplishments

Research objective 2 was addressed in Chapter III and involved the identification of spatial variation in canopy vigor throughout the 2012 growing season. The UAV and digital camera system discussed in Chapter II was used to collect image sets at post-flowering, veraison, and harvest. Object-based image segmentation provided an automated and relatively easy way to delineate vine canopy pixels from non-vine canopy pixels. Based on this separation, canopy objects and subsequent canopy extent (area) was acquired for all vines. This planimetrically-based canopy area was successfully correlated to the field collected vine performance or harvest variables of numbers of clusters, cluster size, and yield. Spectrally-based estimations of canopy density were extracted per-vine using the canopy objects. Median spectral values were extracted for all vines (red and NIR) to calculate $NDVI_{median}$. These spectrally-based attempts to gauge canopy density were not as successful as for canopy area. NIR_{median} reflectance proved to be the only statistically significant variable in correlation analysis with the previously mentioned harvest variables. Red_{median} and subsequent $NDVI_{median}$ had no relationship with eventual vine performance, which relates back to the radiometric inaccuracy found in Chapter II. A simple vine performance index (VPI) was calculated as the product of season average canopy area and season average NIR_{median} to assess per-vine vigor for the 2012 growing season. Following this, grouping analysis was performed and management zones were manually delineated for use in future growing seasons. In the end, Chapter III provided a straightforward, low-cost UAV-based methodology to identify spatial variation in vine performance for an entire vineyard over a single growing season

Chapter IV Accomplishments

Research objective 3 was addressed in Chapter IV and proposed a cutting-edge SfM-based methodology to estimate vineyard canopy LAI. The methodology was moderately successful at predicting LAI for specific vines using several calculated metrics based on a SfM three-dimensional point cloud. Additionally, this SfM-based modeling of the vineyard environment produced 3D visualizations. This methodology is novel due to its inclusion of 3D canopy data, instead of solely using two-dimensional, image-based approaches with NDVI or other vegetation indices, to estimate canopy LAI across an entire vineyard. The results reported in Chapter IV have room for improvement, which may come from increasing point densities (more images, improved SfM algorithms) and/or better image capturing techniques (improved, more uniform coverage). Overall, Chapter IV provided a novel, low-cost UAV and SfM-based method to visualize and quantify vineyard canopy density and structure (LAI) throughout a vineyard.

Final Recommendations for Viticulturists

One of the overarching aims of this dissertation was to not only successfully identify spatial variation in crop performance, but also be able to do so using very inexpensive tools and practical methodologies that could be replicated by other interested researchers and/or practitioners. In this way, the technology used in this dissertation was very low-cost at around $1000 USD total for the UAV and two digital cameras. The methods presented in the Chapters II-IV likewise are for the most part processed with low-cost or open-source software. Although a substantial amount of manual data manipulation and processing time is needed as well as some expensive equipment (GPS,

spectroradiometer; although this equipment could be rented or borrowed), with some training this methodology could be adopted by tech-savvy practitioners. Further, what will likely make adopting such methods even easier in the near future is improvement in UAV technology as well as software to process UAV-collected images. UAVs are becoming increasingly autonomous from launch to retrieval so much so that, unlike in this study, manual control will soon be needed only in emergency situations. Software for processing UAV-collected images is rapidly advancing as well and will likely soon be almost completely automated including options to radiometrically correct input images.

At the very least, orthophotos produced using the proposed methodology outlined in Chapter II (with or without conversion to reflectance) can be used by viticulturists for qualitative analysis of spatial variation in vigor. Additionally, due to the very high spatial resolution of the orthophotos (25 mm), printed maps may serve as useful field tools for sampling, pruning, harvesting, etc. The workers at the vineyard study site were very excited to use these maps and utilized them extensively for daily planning purposes. More advanced users looking to do quantitative analyses can follow the methods provided in Chapters III and IV to explore canopy vigor by way of planimetric extent, spectral assessment (NIR-based) of canopy density, and even attempt to estimate LAI.

LITERATURE CITED

Aber, J.S., I. Marzoff, and J.B. Ries. 2010. *Small-format aerial photography: principles, techniques and geosciences applications*. Oxford, UK: Elsevier.

Acevedo-Opazo, C., B. Tisseyre, S. Guillaume, and H. Ojeda. 2008. The potential of high spatial resolution information to define within-vineyard zones related to vine water status. *Precision Agriculture* 9: 285-302.

Arno, J., A. Escola, J.M. Valles, J. Llorens, R. Sanz, J. Masip, J. Palacin, and J.R. Rosell-Polo. 2013. Leaf area index estimation in vineyards using a ground-based LiDAR scanner. *Precision Agriculture* 14(3): 290-306.

Axelsson, P. 2000. DEM generation from laser scanner data using adaptive TIN models. *International Archives of Photogrammetry and Remote Sensing* 33*:* 110-117.

Baboo, S.S. and M.R. Devi. 2011. Geometric Correction in Recent High Resolution Satellite Imagery: A Case Study in Coimbatore, Tamil Nadu. *International Journal of Computer Applications* 14(1): 32-37.

Baluja, J., M.P. Diago, P. Balda, R. Zorer, F. Meggio, F. Morales, and J. Tardaguila. 2012. Assessment of vineyard water status variability by thermal and multispectral imagery using an unmanned aerial vehicle (UAV). *Irrigation Science* 30(6): 511-522.

Barilotti, A., S. Turco, and G. Alberti. 2006. LAI determination in forestry ecosystem by lidar data analysis. *Proceedings of the Workshop for 3D Remote Sensing of Forestry*, Vienna, Austria.

Bellvert, J., P.J. Zarco-Tejada, J. Girona, and E. Fereres. 2013. Mapping crop water stress index in a 'Pinot-noir' vineyard: comparing ground measurements with thermal remote sensing imagery from an unmanned aerial vehicle. *Precision Agriculture* doi:10.1007/s11119-013-9334-5.

Best, S., L. Leon, and M. Claret. 2005. Use of Precision Viticulture Tools to Optimize the Harvest of High Quality Grapes. *Information and Technology for Sustainable Fruit and Vegetable Production: FRUTIC 05*. Montpellier, France. 12-16 September. 249-258.

Bramley, R.G.V. 2001. Progress in the Development of Precision Viticulture - Variation in Yield, Quality and Soil Properties in Contrasting Australian Vineyards. *Precision Tools for Improving Land Management: 14th Annual FLRC Workshop*. Massey University, New Zealand. 25-43.

Bramley, R.G.V. and R.P. Hamilton. 2004. Understanding variability in winegrape production systems: 1 Within vineyard variation in yield over several vintages. *Australian Journal of Grape and Wine Research* 10: 32-45.

Bramley, R.G.V., B. Pearse, and P. Chamberlain. 2003. Being Profitable Precisely – A Case Study of Precision Viticulture from Margaret River. *The Australian & New Zealand Grapegrower & Winemaker*: Annual Technical Issue.

Bramley, R.G.V. and T. Proffitt. 1999. Managing Variability in Viticultural Production.*The Australian & New Zealand Grapegrower & Winemaker* 427: 11-16.

Bramley, R.G.V., T. Proffitt, C.J. Hinze, B. Pearse, and R.P. Hamilton. 2005. Generating benefits from Precision Viticulture through selective harvesting. *5th European Conference on Precision Agriculture* Uppsala, Sweden. 891-898.

Cheng, C. and A. Rahimzadeh. 2005. *Hacking Digital Cameras*. Indianapolis, IN, USA: Wiley Publishing, Inc.

Coombe, B.G. and P.R. Dry. 1988. *Viticulture: Volume 2, Practices (2nd Edition).* Ashford, SA, Australia: Winetitles.

Creasy, G.L. and L.L. Creasy. 2009. *Crop Production Science in Horticulture 16: Grapes*. Cambridge, UK: CABI.

Cunha, M., A.R.S Marcal, and L. Silva. 2010. Very Early Prediction of Wine Yield Based on Satellite Data from Vegetation. *International Journal of Remote Sensing* 31: 3125-3142.

Dandois, J.P. and E.C. Ellis. 2010. Remote sensing of vegetation structure using computer vision. *Remote Sensing* 2: 1157-1176.

Dandois, J.P. and E.C. Ellis. 2013. High spatial resolution three-dimensional mapping of vegetation spectral dynamics using computer vision. *Remote Sensing of Environment* 136: 259-276.

Dare, P.M. 2008. Small Format Digital Sensors for Aerial Imaging Applications. *The International Archives of the Photogrammetry, Remote Sensing, and Spatial Information Sciences XXXVII*(B1): 533-538.

Dean, C., T.A. Warner, and J.B. McGraw. 2000. Suitability of the DSC460c colour digital camera for quantitative remote sensing analysis of vegetation. *ISPRS Journal of Photogrammetry & Remote Sensing* 55: 105-118.

De Biasio, M., T. Arnold, R. Leitner, G. McGuinnigle, and R. Meester. 2010. UAV-based environmental monitoring using multi-spectral imaging. *Proceedings of SPIE – The International Society for Optical Engineering* 7668: 1-7.

de Blij, H. 1983. *Wine: A Geographic Appreciation.* Totowa, NJ, USA: Rowman & Allanheld Publishers.

Delenne, C., S. Durrieu, G. Rabatel, and M. Deshayes. 2010. From pixel to vine parcel: A complete methodology for vineyard delineation and characterization using remote-sensing data. *Computers and Electronics in Agriculture* 70: 78-83.

Dey, A., L. Mummet, and R. Sukthankar. 2012. Classification of Plant Structures from Uncalibrated Image Sequences. *Proceedings of IEEE Workshop on Applications of Computer Vision* Breckenridge, CO. January 9-11.

Dobrowski, S.Z., S.L. Ustin, and J.A. Wolpert. 2002. Remote estimation of vine canopy density in vertically shoot-positioned vineyards: Determining optimal vegetation indices. *Australian Journal of Grape and Wine Research* 8: 117-125.

Dobrowski, S.Z., S.L. Ustin, and J.A. Wolpert. 2003. Grapevine dormant pruning weight prediction using remotely sensed data. *Australian Journal of Grape and Wine Research* 9: 177-182.

Dry, P.R. and B.G. Coombe. 2004. *Viticulture: Volume 1, Resources (2nd Edition)*. Ashford, SA, Australia: Winetitles.

Everaerts, J. 2008. The use of unmanned aerial vehicles (UAVs) for remote sensing and mapping. *The International Archives of the Photogrammetry, Remote Sensing, and Spatial Information Sciences* XXXVII(B1): 1187-1191.

Fonstad, M.A., J.T. Dietrich, B.C. Courville, J.L. Jensen, and P.E. Carbonneau. 2013. Topographic structure from motion: a new development in photogrammetric measurement. *Earth Surface Processes and Landforms* 38(4): 421-430.

Garrigues, S., N.V. Shabanov, K. Swanson, J.T. Morisette, and F. Baret. 2008. Intercomparison and sensitivity analysis of leaf area index retrievals from LAI-2000, AccuPar, and digital hemispherical photography over croplands. *Agricultural and Forest Meteorology* 148: 1193-1209.

Hall, A. 2003. *Defining Grapevine and Vineyard Characteristics from High Spatial Resolution Remotely Sensed Optical Imagery.* Doctoral thesis, Charles Sturt University (Australia).

Hall, A. and J. Hardie. 2008. Using precision technologies to improve grape yield forecasting. *Australian & New Zealand Grapegrower & Winemaker* 538: 20-24.

Hall, A., D.W. Lamb, B. Holzapfel, and J. Louis. 2002. Optical Remote Sensing Applications in Viticulture - A Review. *Australian Journal of Grape and Wine Research* 8: 36-47.

Hall, A., D.W. Lamb, B. Holzapfel, and J. Louis. 2011. Within-season temporal variation in correlations between vineyard canopy and winegrape composition and yield. *Precision Agriculture* 12: 103-117.

Hall, A. and J. Louis. 2009. Vineclipper: A Proximal Search Algorithm to Tie GPS Field Locations to High Resolution Grapevine Imagery. *Innovations in Remote Sensing and Photogrammetry* 3: 361-372.

Hall, A., J. Louis, and D.W. Lamb. 2003. Characterising and mapping vineyard canopy using high-spatial-resolution aerial multispectral images. *Computers & Geosciences* 23: 813-822.

Hall, A., J. Louis, and D.W. Lamb. 2008. Low resolution remotely sensed images of winegrape vineyards map spatial variability in planimetric canopy area instead of LAI. *Australian Journal of Grape and Wine Research* 14: 9-17.

Hall, A., L. Quirk, M.A. Wilson, and J. Hardie. 2009. Increasing the Efficiency of Forecasting Winegrape Yield by Using Information on Spatial Variability to Select Sample Sites. *The Grapevine Management Guide 2009-2010, National Wine and Grape Industry Centre*, Wagga Wagga, Australia. 11-12.

Hall, A. and M.A. Wilson. 2013. Object-based analysis of grapevine canopy relationships with winegrape composition and yield in two contrasting vineyards using multitemporal high spatial resolution optical remote sensing. *International Journal of Remote Sensing* 34(5): 1772-1797.

Harwin, S. and A. Lucieer. 2012. Assessing the accuracy of georeferenced point clouds produced via multi-view stereopsis from unmanned aerial vehicle (UAV) imagery. *Remote Sensing* 4: 1573-1599.

Hellman, E.W., E.A. Takow, M.D. Tchakerian, and R.N. Coulson. 2011. Geology and Wine 13: Geographic Information System Characterization of Four Appellations in West Texas, USA. *Geoscience Canada* 38(1): 6-20.

Hunt, E.R., M. Cavigelli, C.S.T. Daughtry, J. McMurtrey, and C.L. Walthall. 2005. Evaluation of Digital Photography from Model Aircraft for Remote Sensing of Crop Biomass and Nitrogen Status. *Precision Agriculture* 6: 359-378.

Hunt, E.R., W.D. Hively, C.S.T. Daughtry, and G.W. McCarty. 2008. Remote Sensing of Crop Leaf Area Index Using Unmanned Airborne Vehicles. In *ASPRS Pecora 17*, *Denver, CO,* November 18-20: 1-9.

Hyer, E.J., and S.J. Goetz. 2004. Comparison and sensitivity analysis of instruments and radiometric methods for LAI estimation: assessments from a boreal forest site. *Agricultural and Forest Meteorology* 122: 157-174.

Jackson, R.S. 2008. *Wine Science: Principles and Applications (3rd Edition).* Burlington, MA, USA: Elsevier.

Jensen, J.L.R., K.S. Humes, L.A. Vierling, and A.T. Hudak. 2008. Discrete-return lidar-based prediction of leaf area index in two conifer forests. *Remote Sensing of Environment* 112: 3947–3957.

Jensen, J.R. 2005. *Introductory Digital Image Processing: A Remote Sensing Perspective*. Upper Saddle River, NJ, USA: Pearson Prentice Hall.

Jensen, T., A. Apan, F. Young, and L. Zeller. 2007. Detecting the attributes of a wheat crop using digital imagery acquired from a low-altitude platform. *Computers and Electronics in Agriculture* 59: 66-77.

Johnson, L.F. 2003. Temporal Stability of an NDVI-LAI Relationship in a Napa Valley Vineyard. *Australian Journal of Grape and Wine Research* 9: 96-101.

Johnson, L.F., D.F. Bosch, D. Williams, and B. Lobitz. 2001. Remote sensing of vineyard management zones: implications for wine quality. *Applied Engineering in Agriculture* 17: 557-560.

Johnson, L.F., S. Herwitz, S. Dunagan, B. Lobitz, D. Sullivan, and R. Slye. 2003a. Collection of Ultra High Spatial Resolution Image Data over California Vineyards with a Small UAV. *Proceedings, International Symposium on Remote Sensing of Environment,* Honolulu, HI. 10-14 November.

Johnson, L.F., D.E Roczen, S.K. Youkhana, R.R. Nemani, and D.F. Bosch. 2003b. Mapping vineyard leaf area with multispectral satellite imagery. *Computers and Electronics in Agriculture* 38: 33-44.

Johnson, L.F., and T. Scholasch. 2005. Remote Sensing of Shaded Area of Vineyards. *HortTechnology* 15: 859-863.

Kaminsky, R.S., N. Snavely, S.T. Seitz, and R. Szeliski. 2009. Alignment of 3D point clouds to overhead images. *Second IEEE Workshop on Internet Vision*, Miami, FL.

Karpouzli, E. and T. Malthus. 2003. The empirical line method for the atmospheric correction of IKONOS imagery. *International Journal of Remote Sensing* 24(5): 1143-1150.

Kelcey, J., and A. Lucieer. 2012. Sensor Correction of a 6-Band Multispectral Imaging Sensor for UAV Remote Sensing. *Remote Sensing* 4: 1462-1493.

King, D.J. 1995. Airborne Multispectral Digital Camera and Video Sensors: A Critical Review of System Designs and Applications. *Canadian Journal of Remote Sensing* 21(3): 245-273.

Keightley, K.E. and G.W. Bawden. 2010. 3D Volumetric Modeling of Grapevine Biomass Using Tripod LiDAR. *Computers and Electronics in Agriculture* 74: 305-312.

Kurtural, S.K., I.E. Dami, and B.H. Taylor. 2006. Utilizing GIS Technologies in Selection of Suitable Vineyard Sites. *International Journal of Fruit Science* 6: 87-107.

Laliberte, A., Goforth, M.A., Steele, C.M., & Rango, A. 2011. Multispectral Remote Sensing from Unmanned Aircraft: Image Processing Workflows and Applications for Rangeland Environments. *Remote Sensing* 3(11): 2529-2551.

Lamb, D.W. 2001. Remote Sensing – A Tool for Vineyard Managers? *11th Australian Wine Industry Technical Conference: Workshop W14 Precision Viticulture – Principles, Opportunities and Applications*. Adelaide, Australia. 15-20.

Lamb, D.W., A. Hall, and J. Louis. 2001. Airborne remote sensing of vines for canopy variability and productivity. *Australian & New Zealand Grapegrower & Winemaker* 449: 89-92.

Lamb, D.W., M.M. Weedon, and R.G.V. Bramley. 2004. Using remote sensing to predict grape phelonics and colour at harvest in a Cabernet Sauvignon vineyard: Timing observations against vine phenology and optimising image resolution. *Australian Journal of Grape and Wine Research* 10: 46-54.

Leberl, F., A. Irschara, T. Pock, P. Meixner, M. Gruber, S. Scholz, and A. Weichert. 2010. Point clouds: Lidar *versus* 3D vision. *Photogrammetric Engineering & Remote Sensing* 76: 1123–1134.

Lebourgeois, V., A. Begue, S. Labbe, B. Mallavan, L. Prevot, and B. Roux. 2008. Can Commercial Digital Cameras Be Used as Multispectral Sensors? A Crop Monitoring Test. *Sensors* 8: 7300-7322.

Lelong, C.C.D., P. Burger, G. Jubelin, B. Roux, S. Labbe, and F. Baret. 2008. Assessment of Unmanned Aerial Vehicles for Quantitative Monitoring of Wheat Crop in Small Plots. *Sensors* 8: 3557-3585.

Levin, N., E. Ben-Dor, and A. Singer. 2005. A digital camera as a tool to measure colour indices and related properties of sandy soils in semi-arid environments. *International Journal of Remote Sensing* 26(24): 5475-5492.

Llorens, J.; E. Gil, J. Llop, and A. Escola. 2011a. Ultrasonic and LiDAR sensors for electronic canopy characterization in vineyards: advances to improve pesticide application methods. *Sensors* 11: 2177–2194.

Llorens, J., E. Gil, J. Llop, and M. Queralto. 2011b. Georeferenced LiDAR 3D Vine Plantation Map Generation. *Sensors* 11: 6237-6256.

Louarn, G., J. Lecoeur, and E. Lebon. 2008. A three-dimensional statistical reconstruction model of grapevine (vitis vinifera) simulating canopy structure variability within and between cultivar/training system pairs. *Annals of Botany* 101: 1167–1184.

Mathews, A.J. 2014. A practical UAV remote sensing methodology to generate multispectral orthophotos for vineyards: Estimation of spectral reflectance using compact digital cameras. *International Journal of Applied Geospatial Research* (accepted: February 1).

Mathews A.J. and J.L.R. Jensen. 2012a. An airborne LiDAR-based methodology for vineyard parcel detection and delineation. *International Journal of Remote Sensing* 33: 5251-5267.

Mathews A.J. and J.L.R. Jensen. 2012b. Three-dimensional building modeling using structure from motion: improving model results with telescopic pole aerial photography. *Papers of the Applied Geography Conferences* 35: 98-107.

Mathews, A.J. and J.LR. Jensen. 2013. Visualizing and Quantifying Vineyard Canopy LAI Using an Unmanned Aerial Vehicle (UAV) Collected High Density Structure from Motion Point Cloud. *Remote Sensing* 5(5): 2164-2183.

McCoy, R.M. 2005. *Field Methods in Remote Sensing.* New York, NY, USA: The Guilford Press.

Means, J.E., S.A. Acker, B.J. Fitt, M. Renslow, L. Emerson, and C.J. Hendrix. 2000. Predicting forest stand characteristics with airborne scanning Lidar. *Photogrammetric Engineering & Remote Sensing* 66: 1367–1371.

Morrison, P.C. 1936. Viticulture in Ohio. *Economic Geography* 12: 71-85.

Mullins, M.G., A. Bouquet, and L.E. Williams. 1992. *Biology of the Grapevine*. Cambridge, MA, USA: University Press.

Newman, J.L. 1986. Vines, Wines, and Regional Identity in the Finger Lakes Region. *Geographical Review* 76: 301-316.

Niethammer, U., S. Rothmund, U. Schwaderer, J. Zeman, and M. Joswig. 2011. Open source image-processing tolls for low-cost UAV-based landslide investigations. *International Archives of the Photogrammetry, Remote Sensing and Spatial Information Sciences* XXXVIII-1/C22.

Omasa, K., F. Hosoi, and A. Konishi. 2007. 3D Lidar imaging for detecting and understanding plant responses and canopy structure. *Journal of Experimental Botany* 58: 881-898.

Peduzzi, A, R.H. Wynne, V.A. Thomas, R.F. Nelson, J.J. Reis, and M. Sanford. 2012. Combined use of airborne Lidar and DBInSAR data to estimate LAI in temperate mixed forests. *Remote Sensing* 4: 1758–1780.

Peters, G.L. 1984. Trends in California Viticulture. *Geographical Review* 74: 455-467.

Petrie, R.P., M.C.T. Trought, and G.S. Howell. 2000. Fruit composition and ripening of Pinot Noir (*Vitis vinifera* L.) in relation to leaf area. *Australian Journal of Grape and Wine Research* 6: 45-45.

Popescu, S.C., R.H. Wynne, and J.A. Scrivani. 2004. Fusion of small-footprint and multispectral data toestimate plot-level volume and biomass in deciduous and pine forests in Virginia, USA. *Forest Science* 50: 551–565.

Pollefeys, M., L.V. Gool, M. Vergauwen, F. Verbiest, K. Cornelis, and J. Tops. 2004. Visual modeling with a hand-held camera. *International Journal of Computer Vision* 59: 207-232.

Primicerio, J., S.F. Di Gennaro, E. Fiorillo, L. Genesio, E. Lugato, A. Matese, and F.P. Vaccari. 2012. A flexible unmanned aerial vehicle for precision agriculture. *Precision Agriculture* 13(4): 517-523.

Proffitt, T., R.G.V. Bramley, D.W. Lamb, and E. Winter. 2006. *Precision Viticulture: A New Era in Vineyard Management and Wine Production*. Ashford, SA, Australia: Winetitles.

Rango, A., A. Laliberte, J.E. Herrick, C. Winters, K. Havstad, C. Steele, and D. Browning. 2009. Unmanned aerial vehicle-based remote sensing for rangeland assessment, monitoring, and management. *Journal of Applied Remote Sensing* 3(1): 033542.

Ritchie, G.L., D.G. Sullivan, C.D. Perry, J.E. Hook, and C.W. Bednarz. 2008. Preparation of a Low-Cost Digital Camera System for Remote Sensing. *Applied Engineering in Agriculture* 24: 885-896.

Rodríguez-Pérez, J.R., D. Riaño, E. Carlisle, S. Ustin, and D.R. Smart. 2007. Evaluation of Hyperspectral Reflectance Indexes to Detect Grapevine Water Status in Vineyards. *American Journal of Enology and Viticulture* 58(3): 302-317.

Rosell, J.R., J. Llorens, R. Sanz, J. Arno, M. Ribes-Dasi, J. Masip, A. Escola, F. Camp, F. Solanelles, F. Gracia, E. Gil, L. Val, S. Planas, and J. Palacin. 2009. Obtaining the three-dimensional structure of tree orchards from remote 2D terrestrial LiDAR scanning. *Agricultural and Forest Meteorology* 149: 1505–1515.

Rosnell, T., and E. Honkavaara. 2012. Point cloud generation from aerial image data acquired by a quadrocopter type micro unmanned aerial vehicle and a digital still camera. *Sensors* 12: 453-480.

Rouse, J.W., R.H. Haas, J.A. Schell, and D.W. Deering. 1973. Monitoring Vegetation Systems in the Great Plains with ERTS. *Proceedings of the Third Earth Resources Technology Satellite-1 Symposium NASA SP-351*: 309-317.

Sanz-Cortiella, R., J. Llorens-Calveras, A. Escola, J. Arno-Satorra, M. Ribes-Dasi, J. Masip-Vilalta, F. Camp, F. Gracia-Aguila, F. Solanelles-Batlle, S. Planas-DeMarti, T. Palleja-Cabre, J. Palacin-Roca, E. Gregario-Lopez, I. Del-Moral-Martinez, and J.R. Rosell-Polo. 2011. Innovative LiDAR 3D dynamic measurement system to estimate fruit-tree leaf area. *Sensors* 11: 5769-5791.

Seidel, D., F. Beyer, D. Hertel, S. Fleck, and C. Leuschner. 2011. 3D-laser scanning: a non-destructive method for studying above-ground biomass and growth of juvenile trees. *Agricultural and Forest Meteorology* 151: 1305-1311.

Smit, J.L., G. Sithole, and A.E. Strever. 2010. Vine Signal Extraction – an Application of Remote Sensing in Precision Viticulture. *South African Journal of Enology & Viticulture* 31(2): 65-74.

Smith, G.M. and E.J. Milton. 1999. The use of the empirical line method to calibrate remotely sensed data to reflectance. *International Journal of Remote Sensing* 20(13): 2653-2662.

Snavely, N. 2008. *Scene reconstruction and visualization from internet photo collections*. Doctoral dissertation, University of Washington (USA).

Snavely, N., S.M. Seitz, and R. Szeliski. 2008. Modeling the world from internet photo collections. *International Journal of Computer Vision* 80: 189-210.

Stamatiadis, S., D. Taskos, E. Tsadila, C. Christofides, C. Tsadilas, and J.S. Schepers. 2010. Comparison of passive and active canopy sensors for the estimation of vine biomass production. *Precision Agriculture* 11: 306-315.

Trolier, L.J., W.R. Philipson, and W.D. Philpot. 1989. Landsat TM analysis of vineyards in New York. *International Journal of Remote Sensing* 10: 1277-1281.

Turner, D., A. Lucieer, and C. Watson. 2011. Development of an Unmanned Aerial Vehicle (UAV) for Hyper Resolution Mapping Based Visible, Multispectral, and Thermal Imagery. *Proceedings of 34th International Symposium of Remote Sensing Environment*. Sydney, Australia.

Turner, D., A. Lucieer, and C. Watson. 2012. An automated technique for generating georectified mosaics from ultra-high resolution unmanned aerial vehicle (UAV) imagery, based on structure from motion (SfM) point clouds. *Remote Sensing* 4: 1392-1410.

Wassenaar, T., J.M. Robbez-Masson, and P. Andrieux. 2002. Vineyard identification and description of spatial crop structure by per-field frequency analysis. *International Journal of Remote Sensing* 23: 3331-3325.

Watkins, R.L. 1997. Vineyard site suitability in Eastern California. *GeoJournal* 43: 229-239.

Watts, A.C., V.G. Ambrosia, and E.A. Hinkley. 2012. Unmanned Aerial Systems in Remote Sensing and Scientific Research: Classification and Considerations of Use. *Remote Sensing* 4(6): 1671-1692.

Weigend, G.G. 1954. The Basis and Significance of Viticulture in Southwest France. *Annals of the Association of American Geographers* 44: 75-101.

Zarco-Tejada, P.J., A. Berjon, R. Lopez-Lozano, J.R. Miller,P. Martin, V. Cachorro, M.R. Gonzalez, and A. de Frutos. 2005. Assessing Vineyard Condition with Hyperspectral Indices: Leaf and Canopy Reflectance Simulation in a Row-Structured Discontinuous Canopy. *Remote Sensing of Environment* 99: 271-287.

Zhao, K. and S.C. Popescu. 2009. Lidar-based mapping of leaf area index and its use for validating GLOBCARBON satellite LAI product in a temperate forest of the southern USA. *Remote Sensing of Environment* 113: 1628-1645.